Distribution Agreement

In presenting this thesis or dissertation as a partial fulfillment of the requirements for an advanced degree from Emory University, I hereby grant to Emory University and its agents the non-exclusive license to archive, make accessible, and display my thesis or dissertation in whole or in part in all forms of media, now or hereafter known, including display on the world wide web. I understand that I may select some access restrictions as part of the online submission of this thesis or dissertation. I retain all ownership rights to the copyright of the thesis or dissertation. I also retain the right to use in future works (such as articles or books) all or part of this thesis or dissertation.

Signature:

_____ _____

Ye Yang Date

Photo-induced Charge Carrier Dynamics in Artificial Atoms, Molecules, and Solids Studied by Transient Absorption Spectroscopy

By

Ye Yang
Doctor of Philosophy

Chemistry

_____
Dr. Tianquan Lian, Advisor

_____
Dr. Michael C. Heaven, Committee Member

_____
Dr. R. Brian Dyer, Committee Member

Accepted:

_____
Dean of the Graduate School
Lisa A. Tedesco. Ph.D.

_____
Date

Photo-induced Charge Carrier Dynamics in Artificial Atoms, Molecules, and Solids Studied by Transient Absorption Spectroscopy

By

Ye Yang

B.S. University of Science and Technology of China, Hefei, China, 2008

Advisor: Tianquan Lian, Ph.D.

An abstract of
A dissertation submitted to the Faculty of the
James T. Laney School of Graduate Studies of Emory University
in partial fulfillment of the requirements for the degree of
Doctor of Philosophy
in Chemistry
2013

Abstract

Photo-induced Charge Carrier Dynamics in Artificial Atoms, Molecules, and Solids Studied by Transient Absorption Spectroscopy

By Ye Yang

Quantum confined semiconductor nanoparticles are referred to as artificial atoms due to atomic like energy levels. In analogy to molecules or solids, artificial molecules or solids can be constructed by covalent bonding or by close packing artificial atoms. Recently, these artificial atoms, molecules, and solids have attracted intensive interest in solar-to-electricity and solar-to-fuel applications. To further improve the solar energy conversion efficiency, the fundamental understanding of the dynamics of the photo-induced charge carriers in these artificial systems is required.

In this dissertation, we first investigated the multiple exciton generation (MEG) and dissociation in a model system consisted of PbS quantum dots and electron acceptors. We demonstrated that the presence of electron acceptors did not affect the MEG efficiency of QDs and all generated excitons could be dissociated by electron transfer to the acceptor, achieving MEG and multiple exciton dissociation efficiencies of 112%. We also demonstrated that these efficiencies were not affected by the charging of QDs.

We also studied the strong electronic coupling and hot electron transfer between PbS QDs and TiO_2 nanocrystalline films. In this study, we reported that, due to the strong electronic coupling between 1S electron state and TiO_2 conduction band, the 1S electron transfer time from PbS QDs to TiO_2 films was estimated as 6.4 ± 0.4 fs. We further demonstrated that the 1P electron of the PbS QDs could inject to the TiO_2 films coated by aluminum oxide layers prior to its relaxation to 1S level. The 1P electron injection yield is determined to be 18±4 %.

Finally, we studied the carrier transport and interfacial electron transfer in CdSe heterostructured tetrapod and CdSe QD solids. We find that the electrons in the tetrapod can quickly migrate from the branch to the core and the rate of this electron localization process is not affected by the presence of another electron in the core, suggesting an electron and hole coupled transport in one dimensional confinement. We also showed that photogenerated electrons in quantum dot solid electrodes could be transported to the surface to reduce methyl viologen with 100% quantum efficiency.

Photo-induced Charge Carrier Dynamics in Artificial Atoms, Molecules, and Solids Studied by Transient Absorption Spectroscopy

By

Ye Yang

B.S. University of Science and Technology of China, Hefei, China, 2008

Advisor: Tianquan Lian, Ph.D.

A dissertation submitted to the Faculty of the
James T. Laney School of Graduate Studies of Emory University
in partial fulfillment of the requirements for the degree of
Doctor of Philosophy
in Chemistry
2013

ACKNOWLEDGEMENT

First, I would like to express my gratitude to my advisor, Dr. Tianquan Lian, for his guidance and support during my graduate study at Emory University. Through the discussion with him, I learnt the skills of data analysis, scientific reasoning, and critical thinking. He has taught me not only how to be a self-motivated scientist but also how to work with others. I also wish to extend sincere thanks to my graduate committee members, Dr. Michael C. Heaven and Dr. Brian Dyer, for their insightful comments, challenging questions and valuable support.

I would also like to express my great appreciation to my lab fellows for their support and friendship. Dr. Jier Huang provided me guidance during my first year in the lab. Dr. Chantelle Anfuso has offered me many helps in my writings. Dr. William Rodríguez has been a source of guidance regarding the laser, and working with him was a great experience. I am grateful to my friends and colleagues: Dr. Nianhui Song, Dr. Zheng Liu, Dr. Xu Xiang, Dr. Zheyuan Chen, Haimin Zhu, Kaifeng Wu, Nannan Han, Elisabeth McClure, Hongjin Lv and Chunfu Xu. They have been invaluable to me for challenging me in my research ideas and their support and friendship has been a blessing to me during the past five years. I am also grateful for the help from my other group members, Dr. Shengye Jin, Dr. Zhuangquan Huang, Dr. David Stockwell, Dr. Allen Ricks, Dr. Jinquan Chen, Dr. Yongling Du, Dr. Chris Keating, David Wu, Tony Xu, Kelly Falls.

Finally, I would like to acknowledge my parents and my two sisters for their support, encourage and understanding. Talking to them has always been a comfort and support to me. Special thanks and appreciation are deserved by my wife, Wenting, who has encouraged me at every step of the way.

Table of content

List of Figures

List of Tables

Chapter 1. Introduction

Semiconductor quantum dots (QDs) are often referred to as artificial atoms because the discrete electronic states arising from quantum confinement resemble those of natural atoms.[1, 2] Artificial atoms, however, possess many unique properties including tunable absorption spectra, large absorption coefficient, fast charge transfer rate, potential of charge carrier multiplication, and hot carrier extraction that make them as promising light harvesters for the next generation solar energy conversion.[3-10] Although these properties can be adjusted by changing the size and material of particles, further opportunities for tailoring these properties are expected by coupling two or more quantum confined materials to fabricate a hetero-structures. Because quantum dots are regarded as artificial atoms, the ensemble of the covalently coupled quantum confined components can be considered as "artificial molecules". The new electronic states in the artificial molecules are more controllable than the original states in artificial atoms.[11-20] For example, compared with QDs, the photo-induced electron transfer and back electron transfer rates for core/shell QDs can be more selectively controlled by tuning the electronic states in the core and shell.[21-23] Indeed, many types of artificial molecules, like core-shell, tetrapod, and dot-in-rod nanostructures, have been designed to more efficiently harvest sunlight and deliver the photo-induced charges for solar energy conversion.[24-29] In analogy to solids, an artificial solid can also be constructed by closely packing the artificial atoms or molecules by short chain molecular liners.[30, 31] In addition to the tunable spectral response and inexpensive manufacturing,[32] the strong interaction between adjacent individual particles can lead to high carrier mobility,

including band-like transport in the solid.[33-35] Due to these merits, QD solids have been incorporated in many devices, including photovoltaics,[4, 36, 37] photodectors,[38] and light emitting diodes.[39, 40] To improve the energy conversion efficiency of these devices, the fundamental understanding of the photon induced charge carriers dynamic behaviors in the artificial atoms, molecules as well as the solid are required.

Transient absorption spectroscopy in the visible-NIR and mid-IR regions has been shown to be a powerful tool for studying the carrier dynamics in QDs and interfacial charge transfer from QDs to the charge acceptors.[21, 41-47] Based on this technique, we have studied the ultrafast photo-induced carrier dynamics in model artificial molecules and solids for solar energy conversion, including multiple exciton dissociation and hot electron extraction in the artificial atoms (PbS QDs) and charge transport and interfacial charge transfer in artificial molecules (CdSe tetrapod heterostructures) and solid (CdSe QD films).

1.1. Ultrafast multiple exciton dissociation and hot electron extraction from PbS QDs.

More recently, the use of QDs for low cost and high efficiency solar cells is attracting a great level of interest.[4-9, 25, 27, 28, 37, 38, 48-58] These materials are low cost because they are prepared by colloidal syntheses and amenable to solution processing. The potential energy conversion efficiency of QD-based solar cells may exceed the Shockley-Queisser limit for single junction solar cells due to two novel phenomena in these materials that are results of their strong quantum confinement.[59] The Shockley-Queisser limit in bulk materials is caused by the thermalization loss of the excess energy of the hot carriers that are generated by photons with energy larger than the bandgap.[59] For QD based solar cells, two approaches have been proposed to surpass the Shockley-Queisser limit by reducing the hot carrier thermalization energy loss.[3, 60-63] The first

approach is to utilize the multiple exciton generation (MEG) in QDs, a process in which multiple low energy excitons are generated by one high energy photon. As shown in Figure 1.1, the excess energy of the hot exciton is used to create additional low energy excitons *via* MEG, and the photocurrent of the device can be enhanced by dissociating these multiple excitons. The second approach is to extract the hot electrons and holes before they relax to conduction band (CB) and valence band (VB) edges, respectively, which is also depicted in Figure 1.1. In this case, the energy conversion efficiency is increased by the enhancement of photovoltage.[64, 65]

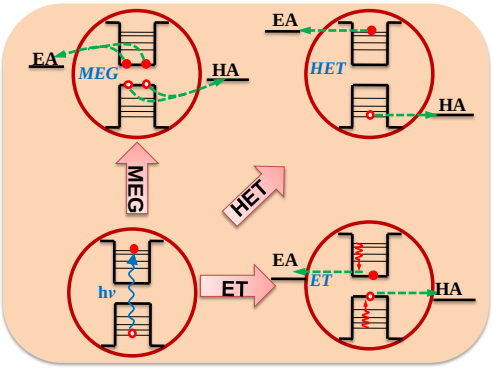

Figure 1.1. Schematic illustration of three hot carrier decay and extraction pathways: hot carrier relaxation (ET), hot carrier extraction (HET), multiple exciton generation (MEG). EA and HA represent electron and hole acceptors.

MEG in bulk materials has been shown to occur with a large threshold energy (>4 and 6 times of band gap in PbS and PbSe, respectively) and low energy efficiency.[66-68] The strong Coulomb interaction of confined carrier and the relaxation of momentum conservation has led to the expectation of more efficient MEG at lower threshold energy in strongly confined QDs.[69, 70] Since the first reports of MEG in PbSe QDs,[69, 71] the efficiency as well as the mechanism of MEG in QDs have been subjects of intense debates.[67, 72-80] The current status and experimental

challenges that were faced by earlier studies have been summarized in recent papers[81, 82] and are not introduced here. It is now generally accepted that the MEG efficiency is modest in PbSe and PbS QDs in the visible and near UV region. The reported MEG efficiencies for PbS and PbSe QDs are less than 120% and 160%, respectively, at excitation energy $\leq 5\ E_g$.[83-85] Internal quantum efficiency of absorbed photon to current conversion (APCE) has been reported to exceed 100% in PbS[86] and PbSe[4] QD based solar cells at near UV wavelength. For practical implementation of MEG based solar cells, the improvement of MEG efficiency at the visible region would be beneficial, and it remains a scientific challenge to understand the MEG mechanism and design materials with improved MEG efficiency and threshold. Extensive studies of bulk SC materials have shown that hot carriers relax on the sub-picosecond and faster time scales through electron-electron and electron phonon coupling. It has been expected that compared to bulk semiconductors, the increased energy level spacing arising from quantum confinement of QDs should lead to much slower hot electron relaxation due to the so called "phonon bottleneck" effect.[87-89] For example, the energy spacing between the 1P and 1S electron level in QDs is about 0.2-0.5 eV[46, 90-95], which would require the excitation of several-to-tens longitudinal optical (LO) phonons if the electron-lattice phonon scattering is the only relaxation pathway. Therefore, the unfavorable Frank-Condon overlap of such process, i.e. the phonon bottleneck effect, should slow down the hot electron relaxation. Unfortunately, extensive research on carrier relaxation in QDs has shown that in addition to the direct electron-to-lattice phonon coupling, hot carriers can also relax by interaction with the vibration of surface ligands as well as Auger-assisted relaxation by the excitation of holes in the quasi-continuous VB.[96-101] The latter process was found to be efficient and typically on the sub-picosecond time scale in most QDs due to the strong Coulomb interaction in these materials. [95, 98-102] These insights have led to the development of a sophisticated core-multi-shell QD in which the 1P to 1S electron relaxation on the nanosecond time scale was achieved by spatially separating the electron and hole and reducing interaction with surface ligands.[19, 103]

A common challenge to both the MEG and hot-carrier based solar cell concepts is the ultrafast dissociation of excitons by interfacial electron transfer (ET) from QDs.[44, 104-110] For MEG based solar cells, multiple excitons need to be dissociated before they annihilate by Auger recombination, which has been shown to occur on the few to hundreds of picoseconds time scale.[111] For hot carrier extraction, interfacial ET has to compete with ultrafast carrier relaxation on the sub-picosecond time scale. Motivated by these challenges, we carried out studies of exciton dissociation from PbS QDs. We started with an investigation of charge separation and recombination in PbS/MB^+ complexes to demonstrate that the electron and hole dynamics could be independently detected by TA spectroscopy.[112] This finding allowed us to directly probe the interfacial electron and hole transfer processes. We then examined the MEG yield in PbS QDs and whether multiexciton dissociation (MED) could compete with Auger recombination in PbS/MB^+ complexes. Our result suggested that the MEG yield in PbS QDs was not affected by binding with MB^+, and 100% of the multiple excitons were dissociated by electron transfer to MB^+.[85] Unfortunately, the rate of ET from PbS to MB^+ was not competitive to hot electron relaxation. To seek systems with faster ET rates, we studied interfacial ET dynamics in the PbS/TiO_2 system, which also served as a good model system for QD based photovoltaic devices. We observed strong electronic coupling between electron levels of PbS QD and TiO_2 CB, which resulted in a <150 fs band edge electron (cool electron) injection rate. These observations suggested the feasibility of hot electron transfer in PbS/TiO_2 system,[113] which is further studied by examining the 1P electron transfer from PbS QDs to the aluminum oxide coated TiO_2 film. In this experiment, the 1S electron transfer was greatly retarded by the aluminum oxide layers and the 1P electron injection yield was determined as 18±4 %.

1.2. Charge transport and interfacial transfer in CdSe tetrapods.

In addition to solar-to-electricity conversion, solar energy can also be converted as chemical fuels. In this approach, the photon generated electron hole pairs in the light absorbers are separated by delivering the electrons to reduce water or CO_2 to hydrogen or carbon-rich fuels and the holes to oxidize the water into oxygen. Compared with conventional dye molecules, the artificial atoms and molecules possess superior advantages in light harvesting and charge delivery steps in this photon conversion process due to the large absorption coefficient over broad spectral range and high charge separation yield. Indeed, the artificial atoms and molecules have been successfully coupled with various catalysts for solar-to-fuel conversions, like water splitting[6, 7, 24, 25, 28, 48, 49, 114-123] and CO_2 reduction.[124, 125] The previously published report also pointed out that the efficiency of the light harvesting and charge separation can be further improved in the branched artificial molecules due to the giant absorption coefficient of one dimensional branch and high degree of asymmetry in electron and hole wavefunctions.[24, 126] Although the interfacial charge separation and recombination processes between various artificial molecules and electron acceptors or donors have been thoroughly examined and also correlated with the quantum yield of photon conversion,[21-24, 127, 128] due to complexity arising from the band alignment, trapping, highly overlapped transitions, and electron-hole interaction the carrier transport mechanism in the heterostructured nanocrystals still remains open questions.[129-133] Compared with the intensively studied dot-in-rod structures, tetrapod structures can have the similar band alignment but with ~10 time larger absorption coefficient resulting from the four perfectly arranged branches that can harvest photons without depending on the direction and polarization.[134]

In this study, we chose the CdSe tetrapod as a model system to study the carrier transport in the heterostructured light harvesters. As consequence of the different crystal structures and quantum confinements in the branches and core, a quai-type II band alignment was formed in the CdSe tetrapods. The transient absorption measurement showed that the lifetime of the electron transport from the branch to the core was ~1.5 ps. By comparing the electron transport rate in

unexcited and excited tetrapods, we found that the electron transport from branch to the core was not affected by the charge carriers localized in the core, suggesting that electron moves with hole as a neutral particle due to the strong exciton binding energy in the one dimensional branches.

1.3. Charge transport and interfacial transfer in CdSe solids.

To date, most reported studies of solar-to-fuel conversion based on artificial atoms and molecules were conducted in homogeneous systems in which sacrificial electron donors were required to remove the hole from the light absorbers to reduce the charging of light absorbers and to prevent charge recombination. However, a practical solar-to-fuel conversion device requires an anode for oxidizing water and cathode for reducing the water or CO_2. Since the reaction is driven by sunlight, photoelectrodes that can capture light and transport photon induced charge carriers are necessary. The artificial solid could serve as the photoelectrode for the solar-to-fuel conversion. The artificial solid can exhibit high photoconductivity due to the electron and hole wave functions overlapping between the adjacent artificial atoms or molecules. [33, 35] At the meanwhile, the solids also possess the tunable absorption response arising from the preserved quantum confinement in the individual artificial atoms.

In this work, we investigated the bulk transport and interfacial transfer dynamics of the photon generated charge carriers in the CdSe QD solid immersed in the methyl viologen solution. We found that the 100% of the photon generated electrons underwent the reduction reaction with the methyl viologen in the solution. The electron transport dynamics in the bulk of the solid can be described by a diffusion model. Our results suggested the feasibility of exploiting the artificial solid as a photoelectrodes in photoelectrochemical cells.

1.4. Summary.

In summary, the photo-induced charge carrier dynamics in artificial atoms, molecules, and solids, were studied by using transient absorption spectroscopy. The rest of this work is organized as follows: Chapter 2 summaries the experimental methods, including the preparations of the samples and the setup of the transient absorption measurement. Chapter 3 introduces the independent detection of electron and hole dynamics in PbS QD. Chapter 4 describes the studies of the multiple exciton generation and dissociation in PbS QD-electron acceptor. Chapter 5 examines the electronic coupling between TiO_2 films and PbS QDs. Chapter 6 demonstrates hot electron injection from the PbS QDs to the TiO_2 films. Chapter 7 and Chapter 8 present the investigation of the photon generated charge carrier transport and interfacial transfer in the heterostructured CdSe tetrapods and CdSe QD solids, respectively.

Reference

1. Kastner, M. A. *Physics Today* **1993,** 46, (1), 24-31.

2. Ashoori, R. C. *Nature* **1996,** 379, (6564), 413-419.

3. Nozik, A. J.; Beard, M. C.; Luther, J. M.; Law, M.; Ellingson, R. J.; Johnson, J. C. *Chem. Rev. (Washington, DC, U. S.)* **2010,** 110, (11), 6873-6890.

4. Semonin, O. E.; Luther, J. M.; Choi, S.; Chen, H.-Y.; Gao, J.; Nozik, A. J.; Beard, M. C. *Science* **2011,** 334, (6062), 1530-1533.

5. Kamat, P. V.; Tvrdy, K.; Baker, D. R.; Radich, J. G. *Chem. Rev. (Washington, DC, U. S.)* **2010,** 110, (11), 6664-6688.

6. Han, Z.; Qiu, F.; Eisenberg, R.; Holland, P. L.; Krauss, T. D. *Science* **2012,** 338, (6112), 1321-1324.

7. Brown, K. A.; Dayal, S.; Ai, X.; Rumbles, G.; King, P. W. *J. Am. Chem. Soc.* **2010,** 132, (28), 9672-9680.

8. Lee, H. J.; Yum, J.-H.; Leventis, H. C.; Zakeeruddin, S. M.; Haque, S. A.; Chen, P.; Seok, S. I.; Grätzel, M.; Nazeeruddin, M. K. *J. Phys. Chem. C* **2008,** 112, (30), 11600-11608.

9. Pattantyus-Abraham, A. G.; Kramer, I. J.; Barkhouse, A. R.; Wang, X. H.; Konstantatos, G.; Debnath, R.; Levina, L.; Raabe, I.; Nazeeruddin, M. K.; Gratzel, M.; Sargent, E. H. *ACS Nano* **2010,** 4, (6), 3374-3380.

10. Salant, A.; Shalom, M.; Hod, I.; Faust, A.; Zaban, A.; Banin, U. *ACS Nano* **2010,** 4, (10), 5962-5968.

11. Kim, S.; Fisher, B.; Eisler, H.-J.; Bawendi, M. *J. Am. Chem. Soc.* **2003,** 125, (38), 11466-11467.

12. Hines, M. A.; Guyot-Sionnest, P. *J. Phys. Chem.* **1996,** 100, (2), 468-471.

13. Peng, X.; Schlamp, M. C.; Kadavanich, A. V.; Alivisatos, A. P. *J. Am. Chem. Soc.* **1997,** 119, (30), 7019-7029.

14. Milliron, D. J.; Hughes, S. M.; Cui, Y.; Manna, L.; Li, J.; Wang, L.-W.; Paul Alivisatos, A. *Nature* **2004,** 430, (6996), 190-195.

15. Peng, P.; Milliron, D. J.; Hughes, S. M.; Johnson, J. C.; Alivisatos, A. P.; Saykally, R. J. *Nano Lett.* **2005,** 5, (9), 1809-1813.

16. Lee, D. C.; Robel, I.; Pietryga, J. M.; Klimov, V. I. *J. Am. Chem. Soc.* **2010,** 132, (29), 9960-9962.

17. Carbone, L.; Nobile, C.; De Giorgi, M.; Sala, F. D.; Morello, G.; Pompa, P.; Hytch, M.; Snoeck, E.; Fiore, A.; Franchini, I. R.; Nadasan, M.; Silvestre, A. F.; Chiodo, L.; Kudera, S.; Cingolani, R.; Krahne, R.; Manna, L. *Nano Lett.* **2007,** 7, (10), 2942-2950.

18. Pietryga, J. M.; Werder, D. J.; Williams, D. J.; Casson, J. L.; Schaller, R. D.; Klimov, V. I.; Hollingsworth, J. A. *J. Am. Chem. Soc.* **2008,** 130, (14), 4879-4885.

19. Pandey, A.; Guyot-Sionnest, P. *Science* **2008,** 322, (5903), 929-932.

20. Costi, R.; Saunders, A. E.; Elmalem, E.; Salant, A.; Banin, U. *Nano Lett.* **2008,** 8, (2), 637-641.

21. Zhu, H.; Song, N.; Lian, T. *J. Am. Chem. Soc.* **2010,** 132, (42), 15038-15045.

22. Zhu, H.; Song, N.; Lian, T. *J. Am. Chem. Soc.* **2011,** 133, (22), 8762-8771.

23. Zhu, H.; Song, N.; Rodríguez-Córdoba, W.; Lian, T. *J. Am. Chem. Soc.* **2012,** 134, (9), 4250-4257.

24. Zhu, H.; Song, N.; Lv, H.; Hill, C. L.; Lian, T. *J. Am. Chem. Soc.* **2012,** 134, (28), 11701-11708.

25. Huang, J.; Mulfort, K. L.; Du, P.; Chen, L. X. *J. Am. Chem. Soc.* **2012,** 134, (40), 16472-16475.

26. Acharya, K. P.; Khnayzer, R. S.; O'Connor, T.; Diederich, G.; Kirsanova, M.; Klinkova, A.; Roth, D.; Kinder, E.; Imboden, M.; Zamkov, M. *Nano Lett.* **2011,** 11, (7), 2919-2926.

27. Khon, E.; Lambright, K.; Khnayzer, R. S.; Moroz, P.; Perera, D.; Butaeva, E.; Lambright, S.; Castellano, F. N.; Zamkov, M. *Nano Lett.* **2013,** 13, (5), 2016-23.

28. Amirav, L.; Alivisatos, A. P. *J. Phys. Chem. Lett.* **2010,** 1, (7), 1051-1054.

29. Huynh, W. U.; Dittmer, J. J.; Alivisatos, A. P. *Science* **2002,** 295, (5564), 2425-2427.

30. Talapin, D. V.; Lee, J.-S.; Kovalenko, M. V.; Shevchenko, E. V. *Chem. Rev. (Washington, DC, U. S.)* **2009,** 110, (1), 389-458.

31. Hanrath, T. *Journal of Vacuum Science & Technology A: Vacuum, Surfaces, and Films* **2012,** 30, (3), 030802-28.

32. Graetzel, M.; Janssen, R. A. J.; Mitzi, D. B.; Sargent, E. H. *Nature* **2012,** 488, (7411), 304-312.

33. Choi, J.-H.; Fafarman, A. T.; Oh, S. J.; Ko, D.-K.; Kim, D. K.; Diroll, B. T.; Muramoto, S.; Gillen, J. G.; Murray, C. B.; Kagan, C. R. *Nano Lett.* **2012,** 12, (5), 2631-2638.

34. Talgorn, E.; Gao, Y.; Aerts, M.; Kunneman, L. T.; Schins, J. M.; Savenije, T. J.; van HuisMarijn, A.; van der ZantHerre, S. J.; Houtepen, A. J.; SiebbelesLaurens, D. A. *Nat Nano* **2011,** 6, (11), 733-739.

35. Lee, J.-S.; Kovalenko, M. V.; Huang, J.; Chung, D. S.; Talapin, D. V. *Nat Nano* **2011,** 6, (6), 348-352.

36. Tang, J.; Kemp, K. W.; Hoogland, S.; Jeong, K. S.; Liu, H.; Levina, L.; Furukawa, M.; Wang, X.; Debnath, R.; Cha, D.; Chou, K. W.; Fischer, A.; Amassian, A.; Asbury, J. B.; Sargent, E. H. *Nat. Mater.* **2011,** 10, (10), 765-771.

37. Luther, J. M.; Law, M.; Beard, M. C.; Song, Q.; Reese, M. O.; Ellingson, R. J.; Nozik, A. J. *Nano Lett.* **2008,** 8, (10), 3488-3492.

38. Sukhovatkin, V.; Hinds, S.; Brzozowski, L.; Sargent, E. H. *Science* **2009,** 324, (5934), 1542-1544.

39. Sun, L.; Choi, J. J.; Stachnik, D.; Bartnik, A. C.; Hyun, B.-R.; Malliaras, G. G.; Hanrath, T.; Wise, F. W. *Nat Nano* **2012,** 7, (6), 369-373.

40. Caruge, J. M.; Halpert, J. E.; Wood, V.; Bulovic, V.; Bawendi, M. G. *Nat Photon* **2008,** 2, (4), 247-250.

41. Burda, C.; Link, S.; Mohamed, M.; El-Sayed, M. *J. Phys. Chem. B* **2001,** 105, (49), 12286-12292.

42. Klimov, V. I. *Annu. Rev. Phys. Chem.* **2007,** 58, 635-673.

43. Robel, I.; Kuno, M.; Kamat, P. V. *J. Am. Chem. Soc.* **2007,** 129, (14), 4136-+.

44. Huang, J.; Stockwell, D.; Huang, Z.; Mohler, D. L.; Lian, T. *J. Am. Chem. Soc.* **2008,** 130, (17), 5632-5633.

45. Huang, J.; Huang, Z. Q.; Yang, Y.; Zhu, H. M.; Lian, T. Q. *J. Am. Chem. Soc.* **2010,** 132, (13), 4858-4864.

46. Wehrenberg, B. L.; Wang, C. J.; Guyot-Sionnest, P. *J. Phys. Chem. B* **2002,** 106, (41), 10634-10640.

47. Huang, J.; Huang, Z.; Jin, S.; Lian, T. *J. Phys. Chem. C* **2008,** 112, (49), 19734-19738.

48. Brown, K. A.; Wilker, M. B.; Boehm, M.; Dukovic, G.; King, P. W. *J. Am. Chem. Soc.* **2012,** 134, (12), 5627-5636.

49. Wang, F.; Wang, W.-G.; Wang, X.-J.; Wang, H.-Y.; Tung, C.-H.; Wu, L.-Z. *Angew. Chem., Int. Ed.* **2011,** 50, (14), 3193-3197.

50. Shemesh, Y.; Macdonald, J. E.; Menagen, G.; Banin, U. *Angew. Chem., Int. Ed.* **2011,** 50, (5), 1185-1189.

51. Robel, I.; Subramanian, V.; Kuno, M.; Kamat, P. V. *J. Am. Chem. Soc.* **2006,** 128, (7), 2385-2393.

52. Wang, X.; Koleilat, G. I.; Tang, J.; Liu, H.; Kramer, I. J.; Debnath, R.; Brzozowski, L.; Barkhouse, D. A. R.; Levina, L.; Hoogland, S.; Sargent, E. H. *Nat Photon* **2011,** 5, (8), 480-484.

53. Johnston, K. W.; Pattantyus-Abraham, A. G.; Clifford, J. P.; Myrskog, S. H.; Hoogland, S.; Shukla, H.; Klem, E. J. D.; Levina, L.; Sargent, E. H. *Appl. Phys. Lett.* **2008,** 92, (12), 122111-3.

54. Shalom, M.; Dor, S.; Rühle, S.; Grinis, L.; Zaban, A. *J. Phys. Chem. C* **2009,** 113, (9), 3895-3898.

55. Salant, A.; Shalom, M.; Tachan, Z.; Buhbut, S.; Zaban, A.; Banin, U. *Nano Lett.* **2012,** 12, (4), 2095-2100.

56. Shalom, M.; Buhbut, S.; Tirosh, S.; Zaban, A. *J. Phys. Chem. Lett.* **2012,** 3, (17), 2436-2441.

57. Selinsky, R. S.; Ding, Q.; Faber, M. S.; Wright, J. C.; Jin, S. *Chem. Soc. Rev.* **2013,** 42, (7), 2963-2985.

58. MacDonald, B. I.; Martucci, A.; Rubanov, S.; Watkins, S. E.; Mulvaney, P.; Jasieniak, J. J. *ACS Nano* **2012,** 6, (7), 5995-6004.

59. Shockley, W.; Queisser, H. J. *J. Appl. Phys.* **1961,** 32, (3), 510-&.

60. Nozik, A. J. *Phys. E* **2002,** 14, (1-2), 115-120.

61. Arthur J, N. *Chem. Phys. Lett.* **2008,** 457, (1-3), 3-11.

62. Hanna, M. C.; Nozik, A. J. *J. Appl. Phys.* **2006,** 100, (7), 074510-8.

63. Nozik, A. J. *Annu. Rev. Phys. Chem.* **2001,** 52, (1), 193-231.

64. Würfel, P. *Sol. Energy Mater. Sol. Cells* **1997,** 46, (1), 43-52.

65. Ross, R. T.; Nozik, A. J. *J. Appl. Phys.* **1982,** 53, (5), 3813-3818.

66. Beard, M. C.; Midgett, A. G.; Hanna, M. C.; Luther, J. M.; Hughes, B. K.; Nozik, A. J. *Nano Lett.* **2010,** 10, (8), 3019-3027.

67. Pijpers, J. J. H.; Ulbricht, R.; Tielrooij, K. J.; Osherov, A.; Golan, Y.; Delerue, C.; Allan, G.; Bonn, M. *Nat. Phys.* **2009,** 5, (11), 811-814.

68. Delerue, C.; Allan, G.; Pijpers, J. J. H.; Bonn, M. *Phys. Rev. B* **2010,** 81, (12), 125306.

69. Schaller, R. D.; Klimov, V. I. *Phys. Rev. Lett.* **2004,** 92, (18), 186601.

70. McGuire, J. A.; Joo, J.; Pietryga, J. M.; Schaller, R. D.; Klimov, V. I. *Acc. Chem. Res.* **2008,** 41, (12), 1810-1819.

71. Ellingson, R. J.; Beard, M. C.; Johnson, J. C.; Yu, P. R.; Micic, O. I.; Nozik, A. J.; Shabaev, A.; Efros, A. L. *Nano Lett.* **2005,** 5, (5), 865-871.

72. Ben-Lulu, M.; Mocatta, D.; Bonn, M.; Banin, U.; Ruhman, S. *Nano Lett.* **2008,** 8, (4), 1207-1211.

73. Nair, G.; Bawendi, M. G. *Phys. Rev. B* **2007,** 76, (8), 081304.

74. Trinh, M. T.; Houtepen, A. J.; Schins, J. M.; Hanrath, T.; Piris, J.; Knulst, W.; Goossens, A. P. L. M.; Siebbeles, L. D. A. *Nano Lett.* **2008,** 8, (6), 1713-1718.

75. McGuire, J. A.; Sykora, M.; Joo, J.; Pietryga, J. M.; Klimov, V. I. *Nano Lett.* **2010,** 10, (6), 2049-2057.

76. Gdor, I.; Sachs, H.; Roitblat, A.; Strasfeld, D. B.; Bawendi, M. G.; Ruhman, S. *ACS Nano* **2012,** 6, (4), 3269-3277.

77. Tyagi, P.; Kambhampati, P. *J. Chem. Phys.* **2011,** 134, (9), 094706-10.

78. Allan, G.; Delerue, C. *Phys. Rev. B* **2006,** 73, (20), 205423.

79. Miaja-Avila, L.; Tritsch, J. R.; Wolcott, A.; Chan, W. L.; Nelson, C. A.; Zhu, X. Y. *Nano Lett.* **2012,** 12, (3), 1588-1591.

80. Ji, M. B.; Park, S.; Connor, S. T.; Mokari, T.; Cui, Y.; Gaffney, K. J. *Nano Lett.* **2009,** 9, (3), 1217-1222.

81. Nair, G.; Chang, L.-Y.; Geyer, S. M.; Bawendi, M. G. *Nano Lett.* **2011,** 11, (5), 2145-2151.

82. Beard, M. C. *J. Phys. Chem. Lett.* **2011**, 1282-1288.

83. Nootz, G.; Padilha, L. A.; Levina, L.; Sukhovatkin, V.; Webster, S.; Brzozowski, L.; Sargent, E. H.; Hagan, D. J.; Van Stryland, E. W. *Phys. Rev. B* **2011,** 83, (15), 155302.

84. Stewart, J. T.; Padilha, L. A.; Qazilbash, M. M.; Pietryga, J. M.; Midgett, A. G.; Luther, J. M.; Beard, M. C.; Nozik, A. J.; Klimov, V. I. *Nano Lett.* **2011,** 12, (2), 622-628.

85. Yang, Y.; Rodríguez-Córdoba, W.; Lian, T. *Nano Lett.* **2012,** 12, (8), 4235-4241.

86. Sambur, J. B.; Novet, T.; Parkinson, B. A. *Science* **2010,** 330, (6000), 63-66.

87. Benisty, H.; Sotomayor-Torrès, C. M.; Weisbuch, C. *Phys. Rev. B* **1991,** 44, (19), 10945-10948.

88. Bockelmann, U.; Bastard, G. *Phys. Rev. B* **1990,** 42, (14), 8947-8951.

89. Inoshita, T.; Sakaki, H. *Phys. Rev. B* **1992,** 46, (11), 7260-7263.

90. Klimov, V. I.; McBranch, D. W. *Phys. Rev. Lett.* **1998,** 80, (18), 4028-4031.

91. Yu, D.; Wang, C.; Guyot-Sionnest, P. *Science* **2003,** 300, (5623), 1277-1280.

92. Wehrenberg, B. L.; Guyot-Sionnest, P. *J. Am. Chem. Soc.* **2003,** 125, (26), 7806-7807.

93. Kang, I.; Wise, F. W. *J. Opt. Soc. Am. B* **1997,** 14, (7), 1632-1646.

94. Schaller, R. D.; Pietryga, J. M.; Goupalov, S. V.; Petruska, M. A.; Ivanov, S. A.; Klimov, V. I. *Phys. Rev. Lett.* **2005,** 95, (19), 196401.

95. Guyot-Sionnest, P.; Shim, M.; Matranga, C.; Hines, M. *Phys. Rev. B* **1999,** 60, (4), R2181-R2184.

96. An, J. M.; Califano, M.; Franceschetti, A.; Zunger, A. *J. Chem. Phys.* **2008,** 128, (16), 164720-7.

97. Guyot-Sionnest, P.; Wehrenberg, B.; Yu, D. *J. Chem. Phys.* **2005,** 123, (7), 074709-7.

98. Hendry, E.; Koeberg, M.; Wang, F.; Zhang, H.; de Mello Donegá, C.; Vanmaekelbergh, D.; Bonn, M. *Phys. Rev. Lett.* **2006,** 96, (5), 057408.

99. Wang, L.-W.; Califano, M.; Zunger, A.; Franceschetti, A. *Phys. Rev. Lett.* **2003,** 91, (5), 056404.

100. Efros, A. L.; Kharchenko, V. A.; Rosen, M. *Solid State Commun.* **1995,** 93, (4), 281-284.

101. Bonati, C.; Cannizzo, A.; Tonti, D.; Tortschanoff, A.; van Mourik, F.; Chergui, M. *Phys. Rev. B* **2007,** 76, (3), 033304.

102. Klimov, V. I.; Mikhailovsky, A. A.; McBranch, D. W.; Leatherdale, C. A.; Bawendi, M. G. *Phys. Rev. B* **2000,** 61, (20), R13349.

103. Pandey, A.; Guyot-Sionnest, P. *J. Phys. Chem. Lett.* **2009,** 1, (1), 45-47.

104. Knowles, K. E.; Malicki, M.; Weiss, E. A. *J. Am. Chem. Soc.* **2012,** 134, (30), 12470-12473.

105. Tagliazucchi, M.; Tice, D. B.; Sweeney, C. M.; Morris-Cohen, A. J.; Weiss, E. A. *ACS Nano* **2011,** 5, (12), 9907-9917.

106. Boulesbaa, A.; Issac, A.; Stockwell, D.; Huang, Z.; Huang, J.; Guo, J.; Lian, T. *J. Am. Chem. Soc.* **2007,** 129, (49), 15132-15133.

107. Wu, K.; Zhu, H.; Liu, Z.; Rodríguez-Córdoba, W.; Lian, T. *J. Am. Chem. Soc.* **2012,** 134, (25), 10337-10340.

108. Burda, C.; Green, T. C.; Link, S.; El-Sayed, M. A. *J. Phys. Chem. B* **1999,** 103, (11), 1783-1788.

109. Tvrdy, K.; Frantsuzov, P. A.; Kamat, P. V. *Proc. Natl. Acad. Sci. U. S. A.* **2011,** 108, (1), 29-34.

110. Matylitsky, V. V.; Dworak, L.; Breus, V. V.; Basche, T.; Wachtveitl, J. *J. Am. Chem. Soc.* **2009,** 131, (7), 2424.

111. Klimov, V. I.; Mikhailovsky, A. A.; McBranch, D. W.; Leatherdale, C. A.; Bawendi, M. G. *Science* **2000,** 287, (5455), 1011-1013.

112. Yang, Y.; Rodríguez-Córdoba, W.; Lian, T. *J. Am. Chem. Soc.* **2011,** 133, (24), 9246-9249.

113. Yang, Y.; Rodríguez-Córdoba, W.; Xiang, X.; Lian, T. *Nano Lett.* **2011,** 12, (1), 303-309.

114. Greene, B. L.; Joseph, C. A.; Maroney, M. J.; Dyer, R. B. *J. Am. Chem. Soc.* **2012,** 134, (27), 11108-11111.

115. Berr, M.; Vaneski, A.; Susha, A. S.; Rodríguez-Fernández, J.; Döblinger, M.; Jäckel, F.; Rogach, A. L.; Feldmann, J. *Appl. Phys. Lett.* **2010,** 97, (9), -.

116. Nann, T.; Ibrahim, S. K.; Woi, P.-M.; Xu, S.; Ziegler, J.; Pickett, C. J. *Angew. Chem., Int. Ed.* **2010,** 49, (9), 1574-1577.

117. Bhoware, S. S.; Kim, K. Y.; Kim, J. A.; Wu, Q.; Kim, J. *J. Phys. Chem. C* **2011,** 115, (5), 2553-2557.

118. Jia, L.; Wang, D.-H.; Huang, Y.-X.; Xu, A.-W.; Yu, H.-Q. *J. Phys. Chem. C* **2011,** 115, (23), 11466-11473.

119. Kim, H. N.; Kim, T. W.; Kim, I. Y.; Hwang, S.-J. *Adv. Funct. Mater.* **2011,** 21, (16), 3111-3118.

120. Li, Q.; Guo, B.; Yu, J.; Ran, J.; Zhang, B.; Yan, H.; Gong, J. R. *J. Am. Chem. Soc.* **2011,** 133, (28), 10878-10884.

121. Tang, M. L.; Grauer, D. C.; Lassalle-Kaiser, B.; Yachandra, V. K.; Amirav, L.; Long, J. R.; Yano, J.; Alivisatos, A. P. *Angew. Chem., Int. Ed.* **2011,** 50, (43), 10203-10207.

122. Wen, F.; Yang, J.; Zong, X.; Ma, B.; Wang, D.; Li, C. *J. Catal.* **2011,** 281, (2), 318-324.

123. Berr, M. J.; Schweinberger, F. F.; Döblinger, M.; Sanwald, K. E.; Wolff, C.; Breimeier, J.; Crampton, A. S.; Ridge, C. J.; Tschurl, M.; Heiz, U.; Jäckel, F.; Feldmann, J. *Nano Lett.* **2012,** 12, (11), 5903-5906.

124. Sato, S.; Arai, T.; Morikawa, T.; Uemura, K.; Suzuki, T. M.; Tanaka, H.; Kajino, T. *J. Am. Chem. Soc.* **2011,** 133, (39), 15240-15243.

125. Wang, C.; Thompson, R. L.; Baltrus, J.; Matranga, C. *J. Phys. Chem. Lett.* **2009,** 1, (1), 48-53.

126. Giblin, J.; Kuno, M. *J. Phys. Chem. Lett.* **2010,** 1, (23), 3340-3348.

127. Zhu, H.; Lian, T. *J. Am. Chem. Soc.* **2012,** 134, (27), 11289-11297.

128. Zhu, H.; Lian, T. *Energy Environ. Sci.* **2012,** 5, (11), 9406-9418.

129. Wu, K.; Rodríguez-Córdoba, W. E.; Liu, Z.; Zhu, H.; Lian, T. *ACS Nano* **2013**.

130. She, C.; Bryant, G. W.; Demortière, A.; Shevchenko, E. V.; Pelton, M. *Phys. Rev. B* **2013,** 87, (15), 155427.

131. Shafran, E.; Borys, N. J.; Huang, J.; Talapin, D. V.; Lupton, J. M. *J. Phys. Chem. Lett.* **2013**, 691-697.

132. Kunneman, L. T.; Zanella, M.; Manna, L.; Siebbeles, L. D. A.; Schins, J. M. *J. Phys. Chem. C* **2013,** 117, (6), 3146-3151.

133. Mauser, C.; Da Como, E.; Baldauf, J.; Rogach, A. L.; Huang, J.; Talapin, D. V.; Feldmann, J. *Phys. Rev. B* **2010,** 82, (8), 081306.

134. Talapin, D. V.; Nelson, J. H.; Shevchenko, E. V.; Aloni, S.; Sadtler, B.; Alivisatos, A. P. *Nano Lett.* **2007,** 7, (10), 2951-2959.

Chapter 2. Experimental Methods

2.1. Sample synthesis.

2.1.1. Synthesis of PbS quantum dots and preparation of PbS/methylene blue complex.

PbS QDs were prepared following a previously reported procedure.[1] Briefly, 0.45 g of lead (II) oxide (Sigma Aldrich), 2.5 ml of oleic acid and 12.5 ml of 1-octadecene (ODE) were injected in a three-neck flask and heated to 120 ºC under a continuous argon flow for two hours. Then, 0.18 ml of hexamethyldisilathiane (Sigma Aldrich) in 5 ml of ODE was injected into this mixture. The resulting solution was kept at 120 ºC for several minutes to allow the formation of the QDs and then quenched by cooling to room temperature. The longer reaction time will lead to the larger particle size. The QDs were precipitated from the growth solution by adding into acetone solvent. The isolated QDs can be dissolved in non-polar solvent such as heptane, hexane and chloroform. The QDs can be further purified by repeating the precipitation and dispersion steps. To prepare the PbS-MB^+ complexes, methylene blue chloride powder was added into PbS heptane solution. The mixture was sonicated and filtered to remove undissolved MB^+.

2.1.2. Synthesis CdSe tetrapod nanocrystals.

Colloid CdSe tetrapods (TPs) were synthesized as described below. Typically, a mixture of 51.2 mg of CdO, 0.5 mL of oleic acid and 5 mL of 1-octadecene in a three-neck flask was heated to 280 ˚C under vigorous stirring to obtain a clear solution. Then 2 mL of selenium source solution was injected into the hot solution. The selenium source stock solution was prepared by dissolving 0.984 g of selenium powder and 5 mL tributylphosphine into 30 mL of 1-octadecene. The temperature was maintained at 280˚C for 3-5 minutes. The growth was then stopped by cooling the reaction solution down to room temperature. At last, the quantum dots were precipitated by adding 30 mL of ethanol to the reaction solution. After centrifuging, the isolated quantum dots were dispersed into heptane or chloroform. A further purification can be done by repeating the precipitation and dispersion steps.

2.1.3. Synthesis of CdSe Quantum dots and preparation of CdSe QD solids.

Colloid CdSe quantum dots (QDs) were synthesized following a published procedure with minor modification.[2] Typically, a mixture of 50 mg of CdO, 1 mL of oleic acid and 8 mL of 1-octadecene in a three-neck flask was heated to 270 ˚C under vigorous stirring to obtain a clear solution. Then a selenium source solution containing 320 mg selenium and 1 mL tributylphosphine was injected into the hot solution. The temperature was maintained at 250˚C for 1-2 minutes to allow the crystal growth to reach a desired size. The growth was then stopped by cooling the reaction solution down to room temperature. The QD was purified in the same way described above as for CdSe TPs.

QD solids were prepared by layer-by-layer spin coating. Clean FTO glass was placed in a spin coater that was set at 2000 rpm. Ethanedithiol or 3-mercaptopropionic acid in acetonitrile (1% by volume) was dropped on the FTO glass and then washed by acetonitrile. This step was followed by the adding few drops of QD solution and rinsing with heptane. These two steps were repeated for 5-20 times to reach a desired thickness. At the end, the prepared samples were annealed at 120 ºC in air for 30 minutes.

2.1.4. Synthesis of TiO_2 nanoparticles and preparation of TiO_2 nanoporous films.

TiO_2 nanocrystalline thin films were prepared by a sol-gel method followed by growth under hydrothermal condition.[3] Specifically, a mixture of 2-propanol (10 mL) and titanium (IV) isopropoxide (37 mL, Aldrich, 97%) was dropped slowly to the acetic acid (80 mL) aqueous solution (water 250 mL) at 0 ºC under vigorous stirring. After overnight aging, the transparent colloidal solution was heated at 80 ºC for 3-4 h under vigorous stirring. The resulting gel was autoclaved at 230 ºC for 12 h and cooled down to room temperature. The gel was separated into the transparent liquid above the white solid paste. About 1mL TritonX-100 was added into 10 mL solid paste. The mixture was stirred for a week to achieve the well dispersed TiO_2 nanoparticle colloidal solution. The TiO_2 film was prepared doctor blading the TiO2 colloidal solution on a tape masked substrate. The films were dried in air and then baked at 450 ºC for 1 hour.

2.2. Pump-probe transient absorption setup.

2.2.1. Femtosecond visible-NIR transient absorption setup.

The femtosecond transient absorption setup is based on a regeneratively amplified Ti:sapphire laser system (coherent Legend, 800 nm, 150 fs, 3 mJ/pulse, and 1 kHz repetition rate). Briefly, the 800 nm output pulse from the regenerative amplifier was split in two parts with a 50:50 beam splitter. One part was used to pump an optical parametric amplifier (Opera, Coherent) which generates two tunable near-IR pulses from 1.1 to 2.5 μm. This signal and idler beams were separated with a dichroic mirror, and used separately to generate visible pumps by sum frequency mixing with the 800 nm fundamental beam in a type I β-BBO crystal. The transmitted 800 nm beam, was split again into two parts. One part, with ~ 1 mJ/pulse, was used to pump a home build optical parametric amplifier for mid-IR probe (see below). The other part was further split into two beams. One with the most power (~ 0.35mJ/pulse) was used as the 800 nm pump or to generate the 400 nm pump by doubling the frequency in a BBO crystal. The pump beam was directed to the main optical delay line. The power of the pump pulses at the sample was controlled by a variable neutral-density filter wheel. The pump beam was chopped by a synchronized chopper (New Focus Model 3501) at 500 Hz. The typical instrument response was well represented by a Gaussian function with a full-width-at-half-maximum (FWHM) of 150 fs.

The remaining 800 nm beam (~ 25 μJ/pulse) was attenuated with a neutral density filter (~3 μJ) and focused into a 2 mm thick sapphire window to generate a white light continuum (WLC) probe. After collimation with an off-axis parabolic mirror, the while light was divided into a signal and a reference beam. While the signal beam measures the absorption of the sample, the reference beam is used to normalize the laser intensity fluctuation. The signal was focused into the sample with a second aluminum parabolic mirror. After the sample, the probe beam was collimated and then focused into a fiber-coupled visible or NIR spectrometer. The visible light (400 nm – 800 nm) of the probe was detected using a CMOS sensor (1024 pixels) while the NIR part (800 nm – 1200 nm) was detected with a InGaAs linear diode array (256 pixels). The diameter of the pump and probe beams at the sample were 250 and 150 μm, respectively. All

experiments were performed at room temperature. During data collection, samples were constantly stirred or translated at a speed of 5 mm/min to avoid photodegradation.

2.2.2. Femtosecond mid-IR transient absorption setup.

The tunable femtosecond mid infrared (mid-IR) measurement is based on a home build optical parametric amplifier pumped with 1 mJ/pulse of the 800 nm fundamental beam (see above), which generate two tunable near-IR pulses from 1.1 to 2.5 μm (signal and idler, respectively). These two beams are combined in a 1-mm-thick $AgGaS_2$ crystal, cut for type II phase matching at 40°, to generate the mid-infrared probe pulses from 3 to 6 μm by difference frequency generation (DFG). The DFG signal was collimated with a 50 cm CaF_2 lens before it was focused into a 200 μm path length cell containing the sample, and at the focal point, it was crossed with the temporally delayed excitation pulse. The diameter of the pump and probe beams at the sample were 300 and 200 μm, respectively. The mid-IR probe was then dispersed in a monochromator and the intensity change of the IR light induced by photoexcitation was monitored as a function of time with a 32-element HgCdTe array detector. The pump beam was chopped by a New Focus Model 3501 Chopper at 500 Hz and its polarization was adjusted at magic angle condition (54.7°) relative to the probe beam. The instrument response function (IRF) of the Vis-pump/Mid-IR-probe spectrometer was determined to have a 230 ± 10 fs full width at half-maximum (FWHM) using a thin silicon wafer. To avoid spectral and temporal reshaping of the Mid-IR probe by absorption of water vapor and CO_2 in air, the entire pump-probe setup was purged by dried air generated by a FTIR purging gas generator (75–62 Parker-Balston).

2.2.3. Nanosecond visible transient absorption setup.

Nanosecond (0.5 ns - 1 μs) transient absorption was measured by the EOS spectrometer (Ultrafast Systems LLC). The pump pulses were generated from the regenerative amplified Ti:sapphire laser system as described above. The probe pulses (400 -1600 nm, 0.5 ns pulse width, 20 KHz repetition rate) was generated by focusing a Nd:YAG laser into a photonic crystal fiber. The probe beam from the light source was split into two before passing through the sample. While one arm traveled through the sample, the other one was sent directly to the reference spectrometer that monitored the fluctuations in the probe beam intensity. The delay between pump and probe was controlled by CNT90 timing unit (Spectracom). The spectrometers for probe detecting were the same as used in the femtosecond setup. The temporal resolution of this system was 0.5 ns, and the spectral resolution was 1.5 nm in visible region and 3.5 nm in NIR region.

2.3. Three-pulse visible transient absorption setup.

The three pulse visible transient absorption setup was similar to the two pulse visible transient absorption. The only change came from the configuration of the pump beams. After the translational delay line, the pump beam split into two parts by a 10:90 beam splitter. The reflected part with 10% of the total power was going to be the pump beam that went through the synchronized chopper. The transmitted beam with 90% of the total power was used as the pre-pump. The pump and pre-pump were collinearly combined and then focused the sample. The intensity of the pre-pump and pump was independently tuned by two neutral density filters.

2.4. Time resolved fluorescence setup.

Time–resolved fluorescence measurements were performed in the time-correlated single photon counting (TCSPC) mode under right-angle sample geometry. The 800nm pulse with a repetition rate of 80 MHz was generated by a mode-locked Ti:Sapphire laser (Tsunami oscillator pumped by a 10 W Millennia Pro, Spectra-Physics) and doubled the frequency to excite the sample. The emission light was focused into a monochromater (Acton SP2150i, Princeton Instrument) and the output with a selected narrow band of wavelength was detected by a micro-channel-PMT (Hamamatsu R3809U-51), the output of which was amplified and analyzed by a TCSPC board (Becker & Hickel SPC 600). To reach a good signal to noise, the spectral width of the output of the monochromator was chosen as ~10 nm.

Reference.

1. Hines, M. A.; Scholes, G. D. *Adv. Mater*. **2003,** 15, (21), 1844-1849.

2. Qu, L.; Peng, X. *J. Am. Chem. Soc.* **2002,** 124, (9), 2049-2055.

3. Zaban, A.; Ferrere, S.; Sprague, J.; Gregg, B. A. *J. Phys. Chem. B* **1997,** 101, (1), 55-57.

Chapter 3. Electron and Hole Dynamics in PbS Quantum Dot-Methylene Blue Complexes

3.1. Introduction

Lead chalgogenide (PbS, PbSe, and PbTe) quantum dot (QD) based solar cells have been intensively investigated in recent years because of the many unique photophysical properties of these materials.[1-4] These properties include tunable and broad spectral responses extending from the visible to near IR regions,[2, 5, 6] long exciton lifetimes,[7, 8] multiple exciton generation (MEG),[9-12] and hot carrier extraction.[13] MEG and hot-carrier extraction provide potential new ways to improve the conversion efficiencies of QD based solar cells by reducing the loss of high energy carriers.[14] Parkinson and co-workers reported MEG induced two-fold photocurrent enhancement in solar cells based on PbS QD sensitized TiO_2 single crystals.[1] Zhu and coworkers reported hot electron injection from PbSe QDs to TiO_2 single crystals.[13] These reports imply ultrafast interfacial electron transfer rates from PbSe and PbS QDs to TiO_2 that are competitive with the fast exciton-exciton annihilation (10 – 100 ps[15, 16]) and the even faster hot electron relaxation (~0.2 – 6 ps[17, 18]) processes. However, recent time-resolved spectroscopy studies have reported interfacial electron transfer rates on a much slower time scale (~100 ns) in PbS-TiO_2 complexes[7] and a lack of hot electron transfer from PbSe to TiO_2 nanoparticles.[19] These discrepancies may be

caused in part by different QDs and QD–TiO_2 linkages used in these studies. Systematical studies of the factors that control the rate of charge transfer from lead salt QDs are needed.

In this chapter, we report a transient absorption (TA) study of the charge carrier separation and recombination dynamics between PbS QDs and an adsorbed electron acceptor, methylene blue (MB^+). We found that both 1S electrons and holes in excited PbS QDs contribute to transient absorption features (1S exciton bleach and induced absorption) in the visible and near IR regions that cannot be easily separated. However, the 1S electrons and holes have distinct intraband absorption features in the mid-IR, which can be used to directly follow their interfacial charge transfer dynamics. We show that the charge separation (electron transfer) and recombination (hole transfer) rates are 2.7±0.2 ps^{-1} and 11.0±2.0 ps^{-1}, respectively.

3.2. Results.

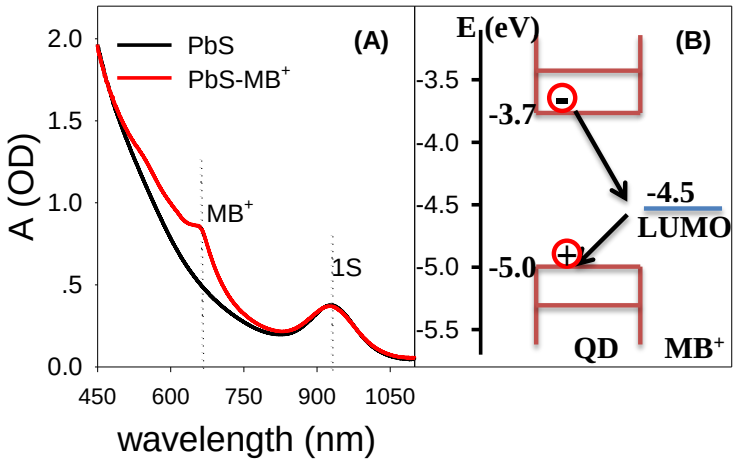

Figure 3.1. (A) UV-vis absorption spectra of free PbS QDs (black dashed line) and PbS-MB^+ complexes (red solid line). (B) Schematic diagram of relevant energy levels (relative to vacuum) involved in the interfacial charge separation (k_{CS}) and recombination (k_{CR}) processes in PbS-MB^+ complexes.

3.2.1. Energy levels and absorption spectra of PbS QD and PbS-MB complex.

The sample preparation procedures and the TA measurement setup are described in Chapter 2. The steady-state absorption spectra of PbS QDs and PbS-MB^+ complexes in heptane solutions are shown in Figure 3.1.A. The absorption spectrum of PbS QDs shows the first ($1S_h \rightarrow 1S_e$) exciton absorption band at 930 nm, corresponding to an estimated particle diameter of 3.6 nm.[20] Compared to free QDs, the absorption spectrum of QD-MB^+ complexes shows the same QD first exciton band at 930 nm and an additional absorption feature centered at 660 nm that corresponds to the ground state absorption of MB^+ molecules. Following the recent reports of Wise and coworkers,[7, 20] the $1S_e$ and $1S_h$ energy levels were estimated to be -3.7 and -5.0 eV (vs vacuum), respectively, as shown in Figure 3.1.B. Compared with the reduction potential of MB^+ (-4.5 eV vs vacuum),[21] estimated Gibbs free energy change (or driving forces) for electron transfer from the excited PbS to MB^+ and the subsequent charge recombination processes are -0.8, and -0.5 eV, respectively. [22, 23]

According to the energy level configuration in PbS-MB complex, the expected interfacial charge transfer processes in this system can be summarized by eq. 3.1.

$$\begin{aligned} PbS^{**} - MB^+ &\xrightarrow{k_R} PbS^{*}(1S_e, 1S_h) - MB^+ \\ &\xrightarrow{k_{CS}} PbS^{+}(1S_h) - MB^{\cdot} \xrightarrow{k_{CR}} PbS - MB^+ \end{aligned} \qquad (3.1)$$

where PbS**-MB^+ represents an excited complex with the QD in the initial excited state generated by the excitation pulse. It relaxes with a rate constant k_R to form PbS*-MB^+ in which the QD is in the 1S exciton state. Charge separation in the excited complex (with a rate constant k_{CS}) generates the charge separated state (PbS^+-$MB^{\cdot}$), which recombines (with a rate constant k_{CR}) to regenerate the complex in the ground state (PbS-MB^+).

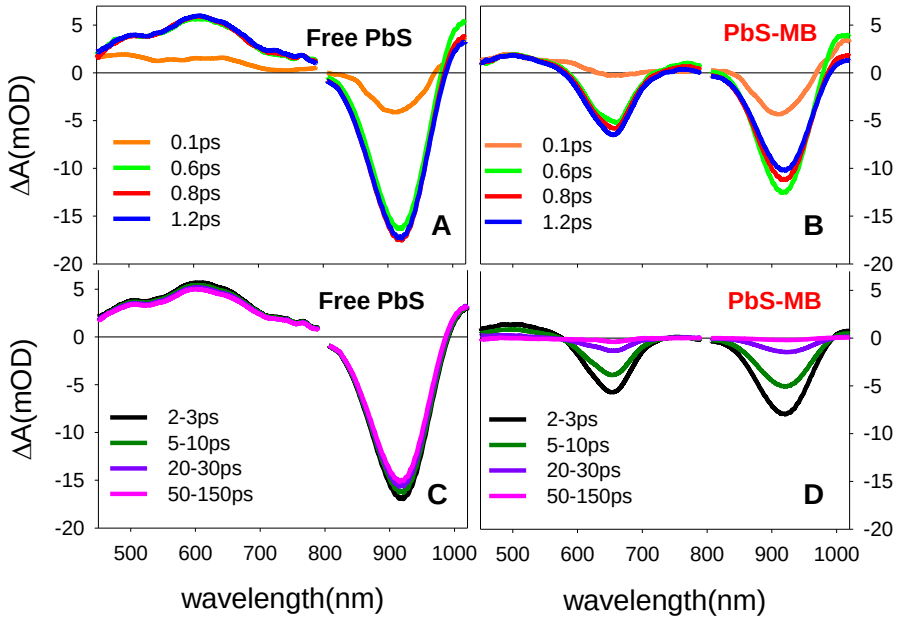

Figure 3.2. Visible and near-IR transient absorption spectra of (A) PbS QDs and (B) PbS-MB$^+$ complexes in heptane at indicated delay time windows after 800 nm excitation. Upper panels: 0.1 – 1.2 ps; lower panels: 2 – 150 ps.

3.2.2. Charge separation and recombination measured by visible-NIR TA.

The visible and near-IR TA spectra of PbS and PbS-MB$^+$ measured under the same conditions are compared in Figure 3.2. The TA spectra of free QDs show a bleach of the 1S exciton band (~930 nm) and a broad positive band from 450 to 800 nm. The 1S exciton bleach is caused by the state-filling of the 1S electron and hole levels.[24] The broad positive absorption has been attributed to the Stark effect-induced red-shift of the higher energy bands in the presence of the 1S exciton.[25-27] These exciton-induced absorption and bleach features show only a small decay (< 15%) within 150 ps, indicating that most excited QDs are in long-lived (> 1 ns) single exciton states under these experimental conditions.

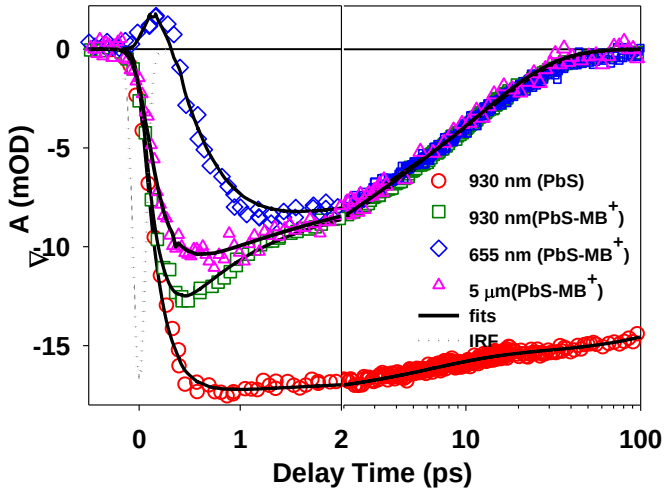

Figure 3.3. Comparison of 1S exciton bleach recovery kinetics (at 930 nm) of free PbS QDs (red circles) and PbS-MB^+ complexes (green squares). Also shown are the normalized kinetics of the MB^+ ground state bleach (GSB at 655 nm, blue diamonds) and the $1S_h$-$1P_h$ intraband transition (at 5 μm, purple triangles) in PbS-MB^+ complexes. These kinetics were normalized to match those of the 1S exciton bleach at the later delay times. Solid lines are fits to a kinetics model described in the supporting information. The dotted curve is the instrument response function. The x axis is in linear scale in the left panel (-0.5 – 2 ps) and in logarithmic scale in the right panel (2 – 100 ps).

The TA spectra of the PbS-MB^+ complexes (Figure 3.2.B) show an ultrafast (< 0.6 ps) formation of the MB^+ ground state bleach (GSB) at 660 nm in addition to the PbS 1S exciton induced TA features. The amplitude of the 1S exciton bleach at 0.6 ps is considerably (~30%) smaller than that in free PbS QDs under the same conditions. This can be more readily seen in Figure 3.3, in which the kinetic traces of the 1S exciton bleach (at 930 nm) in PbS-MB^+ complexes and free PbS QDs are compared. The observed ultrafast exciton bleach recovery and MB^+ bleach formation indicates ultrafast quenching of the PbS excitons by MB^+. From the

energetics shown in Figure 3.1.B, exciton quenching by hole transfer and energy transfer is not possible in this system. Therefore it can be attributed to ultrafast electron transfer from the PbS to MB^+. The ET process should generate reduced MB^+ molecules (MB· radicals) with an absorption band at around 420 nm,[28] a spectral region that is unfortunately not accessible in this study due to the strong (OD > 2) QD absorption (see Figure 3.1.A). Further support for this assignment will be provided below by directly probing the electron and hole intraband transitions.

The TA spectra after 2 ps show the simultaneous recovery of the MB^+ ground state bleach and the decay of the QD TA features (1S exciton bleach and induced absorption). As shown in Figure 3.3, the recovery of the MB^+ ground state bleach and 1S exciton bleach follow the same kinetics, suggesting that the spectral evolution after 2 ps can be attributed to recombination of the electron in the MB· radical with the 1S hole in the PbS QD (to regenerate both MB^+ and QD ground state). These kinetics differ at $t < 2$ ps due to the overlapping contributions of the 1S electron induced TA features (bleach at 930 nm and induced absorption at 655 nm) and MB^+ ground state bleach. The electron transfer process leads to the recovery of the 1S electron induced bleach at 930 nm and the formation of the MB^+ ground state bleach at 655 nm. As will be discussed later, the 1S electron dynamics can be extracted by global fitting of these kinetic traces.

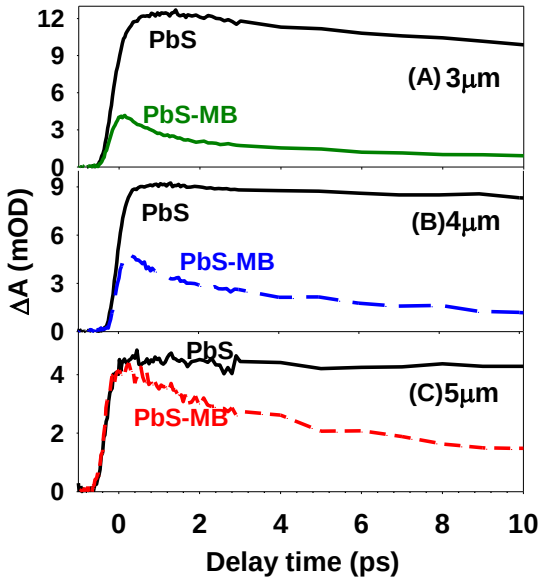

Figure 3.4. Comparison of mid-IR kinetics of free PbS QDs (black line) and PbS-MB$^+$ complexes at (A) 3.0 (green solid line), (B) 4.0 (blue long dashed line) and (C) 5.0 μm (red short dashed line).

3.2.3. Charge separation and recombination measured by mid-IR TA.

Clearly, the 1S exciton induced bleach and absorption in the visible and near IR contain contributions from both 1S electrons and holes, consistent with a previous electrochemical study of charged PbS QDs.[24] The same study also showed that the electron ($1S_e \rightarrow 1P_e$) intraband transition in the mid-IR has a slightly higher energy than the hole ($1S_h \rightarrow 1P_h$) transitions. In this work, we utilize this energy separation to independently probe the electron and hole dynamics in the PbS-MB$^+$ complexes, enabling us to follow directly the charge separation and recombination processes, respectively. The kinetics of mid-IR absorption of free PbS QDs and PbS-MB$^+$ complexes are compared in Figure 3.4.A-C. The free QD mid-IR absorptions are long lived (only the first 10 ps are shown), consistent with the presence of long-lived single excitons. Similar absorptions were previously observed in PbSe QDs.[29, 30] The kinetics of PbS-MB$^+$ complexes

show much faster decays. The initial mid-IR absorptions in PbS-MB^+ are about 30% and 50% of those in free PbS QDs at 3.0 and 4.0 μm, respectively, suggesting an ultrafast decay (< 0.5 ps) due to the ultrafast electron transfer process. This ultrafast decay component is absent at 5.0 μm, where the initial signal amplitude is the same as that in free PbS QDs. Therefore the absorption at 5.0 μm can be attributed to the hole $1S_h \rightarrow 1P_h$ intraband transition and is a direct probe of the 1S hole dynamics. This assignment is supported by the comparison in Figure 3.3, which shows that the kinetics at this wavelength are identical to those of the 1S exciton bleach and MB^+ bleach recovery after 2 ps.

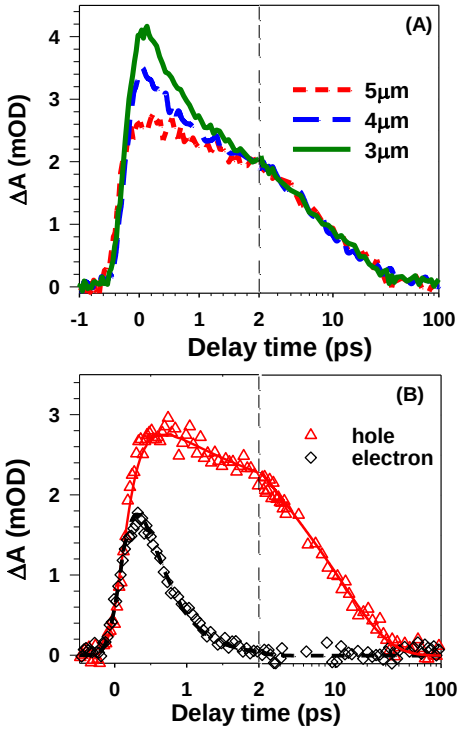

Figure 3.5. (A) Normalized comparison of kinetics at 3.0, 4.0 and 5.0 μm in PbS-MB^+. The kinetics at 4.0 and 5.0 μm were normalized to match those at 3.0 μm at long delay time. (B) Kinetics of 1S electrons (black square) and 1S holes (red triangles) in PbS-MB^+ complexes. The 1S hole kinetics is monitored at 5.0 μm, where the IR absorption is dominated by the $1S_h$-$1P_h$

transition. The 1S electron kinetics is obtained by subtracting the hole contribution to the total signal at 3.0 μm. Solid and dashed lines are fits. In both panels, the x axes are in linear scale in the left panel (-0.5 – 2 ps) and in logarithmic scale in the right panel (2 – 100 ps).

As shown in Figure 3.5.A, a normalized comparison of the mid-IR absorptions at 3.0, 4.0 and 5.0 μm in PbS-MB^+ complexes indicates that after 2 ps these kinetics are identical and probe the population of the 1S hole (i.e. the charge recombination process). They differ in the amplitudes of the ultrafast decay component, which increases at higher energy due to an increased contribution from the electron $1S_e \rightarrow 1P_e$ transition. The electron kinetics can be obtained by subtracting the hole contribution (represented by the normalized kinetics at 5 μm) from the total signal at 3.0 μm, as shown in Figure 3.5.B. The electron kinetics show an ultrafast decay within 2 ps, consistent with the observed ultrafast 1S exciton recovery and MB^+ bleach formation shown in Figure 3.2 and 3.3. Our data also suggest that it should be possible to identify a spectral window (<3 μm) that monitors only the 1S electron dynamics.

3.3. Discussions.

To quantify the charge separation and recombination rates in the PbS-MB^+ complexes, we fit the kinetics shown in Figure 3.3 and 3.5 according to equation 1. A detailed kinetics model that describes the time-dependent concentration of various species and the fitting procedure are given in the supporting information. The kinetics of free QDs at 930 nm were first fit to obtain the hot excited state relaxation rate k_R (5.9 ps^{-1}), which is assumed to be the same for the PbS-MB^+ complexes. The normalized kinetics at 5.0 μm were then fit to obtain the charge recombination rate (k_{CR}). Finally, the kinetics at 930 nm (1S exciton bleach), at 655 nm (MB^+ ground state), and at 3.0 μm (1S electron and hole) were fit simultaneously with the charge separation rate (k_{CS}) as

the only fitting parameter. As shown in Figure 3.3, 3.4 and 3.5, these kinetics are well fit by this model. Biexponential functions were needed to satisfactorily describe both the charge separation and recombination kinetics, reflecting the heterogeneities of these interfacial processes. From the biexponential fits, amplitude-weighted average time constants were calculated, yielding average charge separation and recombination rates of 2.7 ± 0.2 ps^{-1} and 11 ± 2 ps^{-1}, respectively, in the PbS-MB^+ complexes. The error bars reflect standard deviations of rates determined from three sets of data

It is interesting to note that the charge separation rate is approximately a factor of 2 slower than the electron relaxation rate, suggesting that in some of the complexes charge separation may have occurred prior to electron relaxation to the 1S level. This finding is consistent with a recent study of PbSe QDs on TiO_2 single crystals, in which hot electron transfer from PbSe to TiO_2 and an ultrafast (~10 ps) charge recombination were observed.[13] The observed ultrafast charge separation rate also suggests the possibility of dissociating multiple excitons prior to the exciton-exciton annihilation process.[9-12] The multiple exciton generation and dissociation study is going to be discussed in next chapter. Our results are also consistent with the efficient multi-exciton collection reported for solar cells based on PbS QD sensitized TiO_2 single crystals, assuming the charge recombination process can be suppressed under device operation conditions.[1] A recent report of the formation of a depleted heterojunction between PbS and TiO_2 offers a possible mechanism for preventing the charge recombination process in these devices.[3] Our study also suggests the possibility of directly measuring the charge separation and recombination rates by monitoring the intraband transitions at the PbS and PbSe/TiO_2 interfaces, which would offer a better comparison with the reported hot electron injection and multi-exciton collection in these materials.[1, 13] Such studies are going to be discussed in Chapter 4 and 5.

3.4. Conclusion.

In summary, charge separation and recombination in PbS-MB^+ complexes have been studied by transient absorption spectroscopy. While the 1S electron and hole contribute to overlapping transient absorption features in the visible and near IR regions, they have distinct intraband transitions in the mid-IR that can be used to follow their dynamics independently. We show that the charge separation and recombination rates are 2.7 ± 0.2 and 11 ± 2 ps^{-1}, respectively. The ultrafast charge separation rate suggests the possibility of hot electron extraction and multi-exciton dissociation from these strongly quantum confined QDs that are going to be further discussed in the following three chapters.

Reference.

1. Sambur, J. B.; Novet, T.; Parkinson, B. A. *Science (Washington, DC, United States)* **2010,** 330, (6000), 63-66.

2. Sargent, E. H. *Nature Photonics* **2009,** 3, (6), 325-331.

3. Pattantyus-Abraham, A. G.; Kramer, I. J.; Barkhouse, A. R.; Wang, X.; Konstantatos, G.; Debnath, R.; Levina, L.; Raabe, I.; Nazeeruddin, M. K.; Gratzel, M.; Sargent, E. H. *ACS Nano* **2010,** 4, (6), 3374-3380.

4. Luther, J., M.; Law, M.; Beard, M., C.; Song, Q.; Reese, M., O.; Ellingson, R., J.; Nozik, A., J. *Nano letters* **2008,** 8, (10), 3488-92.

5. Hines, M. A.; Scholes, G. D. *Adv. Mater.* **2003,** 15, (21), 1844-1849.

6. Murray, C. B.; Sun, S.; Gaschler, W.; Doyle, H.; Betley, T. A.; Kagan, C. R. *IBM J. Res. & Dev.* **2001,** 45, 47.

7. Hyun, B.-R.; Zhong, Y.-W.; Bartnik, A. C.; Sun, L.; AbrunÌƒa, H. D.; Wise, F. W.; Goodreau, J. D.; Matthews, J. R.; Leslie, T. M.; Borrelli, N. F. *ACS Nano* **2008,** 2, (11), 2206-2212.

8. Leventis, H. C.; O'Mahony, F.; Akhtar, J.; Afzaal, M.; O'Brien, P.; Haque, S. A. *J. Am. Chem. Soc.* **2010,** 132, (8), 2743-2750.

9. Pijpers, J. J. H.; Ulbricht, R.; Tielrooij, K. J.; Osherov, A.; Golan, Y.; Delerue, C.; Allan, G.; Bonn, M. *Nat. Phys.* **2009,** 5, (11), 811-814.

10. McGuire, J. A.; Sykora, M.; Joo, J.; Pietryga, J. M.; Klimov, V. I. *Nano letters* **2010,** 10, (6), 2049-2057.

11. Beard, M. C.; Midgett, A. G.; Hanna, M. C.; Luther, J. M.; Hughes, B. K.; Nozik, A. J. *Nano letters* **2010,** 10, (8), 3019-3027.

12. Nair, G.; Geyer, S. M.; Chang, L.-Y.; Bawendi, M. G. *Phys. Rev. B* **2008,** 78, (12), 125325.

13. Tisdale, W. A.; Williams, K. J.; Timp, B. A.; Norris, D. J.; Aydil, E. S.; Zhu, X.-Y. *Science (Washington, DC, United States)* **2010,** 328, 1543-1547.

14. Nozik, A. J. *Physica E: Low-Dimensional Systems & Nanostructures (Amsterdam, Netherlands)* **2002,** 14, (1-2), 115-120.

15. Schaller, R. D.; Sykora, M.; Pietryga, J. M.; Klimov, V. I. *Nano Letters* **2006,** 6, (3), 424-429.

16. Klimov, V. I.; McGuire, J. A.; Schaller, R. D.; Rupasov, V. I. *Physical Review B* **2008,** 77, (19), -.

17. Schaller, R. D.; Pietryga, J. M.; Goupalov, S. V.; Petruska, M. A.; Ivanov, S. A.; Klimov, V. I. *Phys. Rev. Lett.* **2005,** 95, (19), 196401.

18. Harbold, J. M.; Du, H.; Krauss, T. D.; Cho, K. S.; Murray, C. B.; Wise, F. W. *Physical Review B* **2005,** 72, (19), -.

19. Pijpers, J. J. H.; Koole, R.; Evers, W. H.; Houtepen, A. J.; Boehme, S.; Donega, C. D.; Vanmaekelbergh, D.; Bonn, M. *J. Phys. Chem. C* **2010,** 114, (44), 18866-18873.

20. Kang, I.; Wise, F. W. *J. Opt. Soc. Am. B* **1997,** 14, (7), 1632-1646.

21. Kamat, P. V.; Dimitrijevic, N. M.; Fessenden, R. W. *Journal of Physical Chemistry* **1987,** 91, 396.

22. Brus, L. *J. Chem. Phys.* **1983,** 79, (11), 5566-5571.

23. Brus, L. E. *J. Chem. Phys.* **1984,** 80, 4403-4409.

24. Wehrenberg, B. L.; Guyot-Sionnest, P. *J. Am. Chem. Soc.* **2003,** 125, (26), 7806-7807.

25. Kohn, S. E.; Yu, P. Y.; Petroff, Y.; Shen, Y. R.; Tsang, Y.; Cohen, M. L. *Phys. Rev. B* **1973,** 8, (4), 1477-1488.

26. Kanazawa, H.; Adachi, S. *J. Appl. Phys.* **1998,** 83, (11), 5997-6001.

27. Cho, B.; Peters, W. K.; Hill, R. J.; Courtney, T. L.; Jonas, D. M. *Nano Lett.* **2010,** 10, (7), 2498-2505.

28. Huang, J.; Huang, Z. Q.; Yang, Y.; Zhu, H. M.; Lian, T. Q. *J. Am. Chem. Soc.* **2010,** 132, (13), 4858-4864.

29. Ji, M.; Park, S.; Connor, S. T.; Mokari, T.; Cui, Y.; Gaffney, K. J. *Nano Letters* **2009,** 9, (3), 1217-1222.

30. Ellingson, R. J.; Beard, M. C.; Johnson, J. C.; Yu, P.; Micic, O. I.; Nozik, A. J.; Shabaev, A.; Efros, A. L. *Nano Letters* **2005,** 5, (5), 865-871.

Chapter 4. Multiple Exciton Generation and Dissociation in PbS Quantum Dot-Electron Acceptor Complexes

http://pubs.acs.org/doi/pdf/10.1021/nl301847r

4.1. Introduction.

Multiexciton generation (MEG), a process by which one absorbed photon generates multiple electron hole pairs (or excitons), has been reported in lead chalcogenide quantum dots (QDs).[1-6] Since the initial report in 2004, the MEG efficiency of QDs has been a subject of intense debate.[7-11] Despite these debates and recent reports of modest efficiency (~110~125% at 3.1 eV for PbSe and PbS QDs),[10, 12-14] MEG continues to attract intense research interest because of its potential applications in photovoltaic and photocatalytic devices. In the absence of MEG, hot electron-hole pairs in semiconductors, generated by high energy photons, relax rapidly to the conduction and valence band edges, losing their excess energy by thermalization. With MEG, the excess energy of high energy photons is converted to additional low energy excitons, enhancing the energy conversion efficiency. Theoretical studies suggest that the maximum power conversion efficiency of a single junction photovoltaic device can be increased from 33.7% to 44.4% under ideal MEG conditions.[15, 16] Although the expected large improvement has yet to be realized in devices, there have been reports of MEG enhanced photocurrents in photodetectors,[17] photoelectrochemical cell,[18] and solar cells.[19] For example, an external photo-to-current conversion efficiency of larger than 100% (at 3.44 eV) was reported for a PbSe based solar cell with a power conversion efficiency of ~2%[19] and an absorbed photon-to-current conversion efficiency of as high as 180%

(at 3.1 eV) have been observed in a photoelectrochemical cell with a single crystalline TiO_2 electrode sensitized by a monolayer of PbS QDs.[18]

Practical application of MEG requires the development of materials with lower MEG threshold and higher efficiency and schemes for efficient extraction of multiple excitons before their ultrafast annihilation. One potential scheme is efficient multiple exciton dissociation (MED) by ultrafast interfacial charge transfer to electron or hole acceptors. Ultrafast electron transfer from QDs to molecular and semiconductor electron acceptors have been reported.[20-26] Some of these ultrafast electron transfer systems have been used in recent proof-of-principle experiments to demonstrate that multiple excitons in QDs, generated by multiple-photon absorptions, can be efficiently dissociated.[27-29] So far, most MEG studies have been carried out for PbS and PbSe QDs in the absence of electron acceptors and some studies have reported strong influence of QD surface treatment and charging on the MEG efficiency.[30-32] Ultrafast electron transfer requires electronic interaction between QDs and electron acceptors, which perturbs the electronic structure of the QDs. In some cases, such as PbS on TiO_2, their strong coupling leads to significant broadening of exciton peaks in QDs,[33] which may affect the dynamics of multiple exciton generation. It remains unclear whether the MEG efficiency in QD-acceptor complexes is affected by the presence of the electron acceptors and whether high MEG and MED efficiencies can be simultaneously achieved.

In this chapter, we examine MEG and MED in PbS QD/Methylene blue (PbS-MB^+) complexes. MB^+ is chosen as a model electron acceptor due to reported ultrafast electron transfer (ET) rate in related PbS/MB^+ complexes as well as its strong absorption band in the visible region that enables the probe of the ET process.[28, 34] We first determine that the MEG efficiency of the PbS QDs used in this study is 112±2 % at 400 nm (~2.9 times the band gap) excitation. In PbS/MB^+ complexes, the quantum efficiency of MB^+ reduction is also 112±4%, which suggests that the MEG efficiencies of the PbS QD is not affected by the presence of MB^+ and all generated

excitons can be dissociated by electron transfer to MB^+. Furthermore, photocharging of PbS-MB^+ complexes does not affect MEG and MED efficiencies.

4.2. Results and discussions.

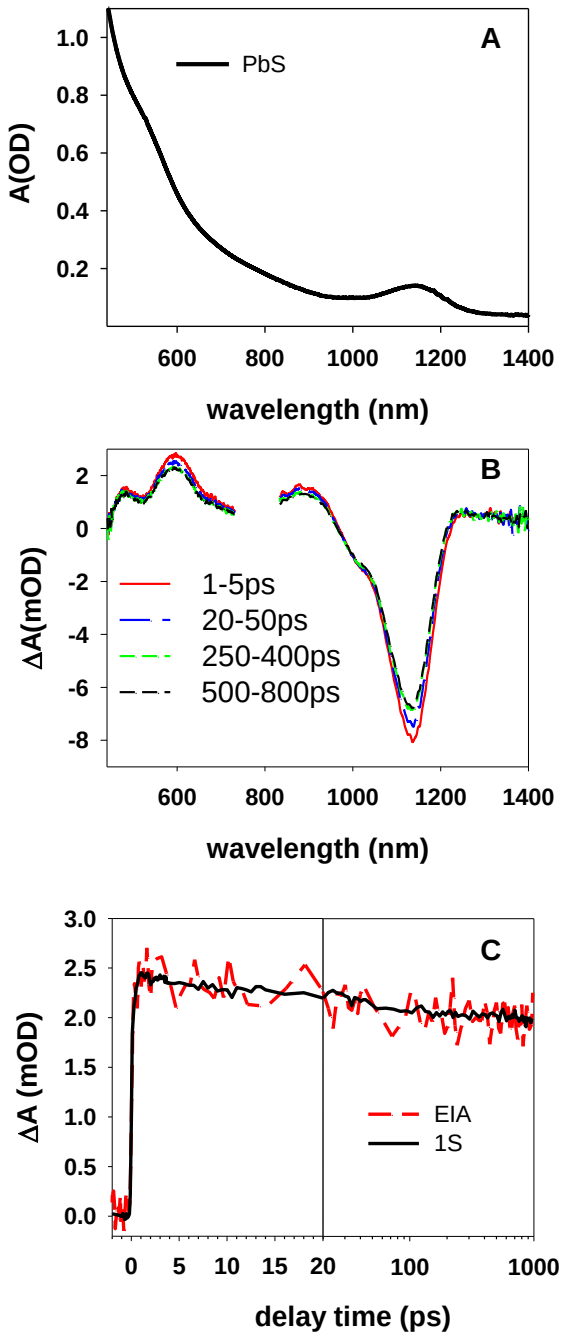

Figure 4.1. (A) Steady state absorption spectrum and (B) Transient absorption spectra of the PbS QDs at indicated delay time windows after 400 nm excitation. (C) Comparison of kinetic traces of exciton induced absorption (EIA) (600 to 620 nm) and 1S exciton bleach (1S) (1135 to 1140 nm). The latter kinetics was inversed and scaled for better comparison. The x-axes in panel C are in linear scale from 0-20 ps and logarithmic scale from 20-1000ps.

4.2.1. Steady-state and Transient Absorption Spectra of PbS QDs.

As shown in Figure 4.1.A, visible-NIR absorption spectrum of PbS QDs in heptane solution shows a 1S exciton absorption band ($1S_h \rightarrow 1S_e$) centered at 1140 nm, corresponding to a band gap (E_g) of 1.08 eV. In the TA measurement, the QD sample was excited at 400 or 800 nm and probed in visible and near-infrared (NIR) region. Unless specified, all TA measurements were conducted with QD solutions that were rigorously stirred with a magnetic stirrer to prevent the build-up of photoproducts. The typical TA spectra of PbS QDs are shown in Figure 4.1.B at indicated delay time windows after 400 nm excitation. In the NIR region, 1S exciton bleach centered at 1140 nm can be attributed to the state filling of both 1S electron and hole levels.[34, 35] Within 250 ps, the bleach amplitude recovers to approximately 80% of the initial value, caused by the Auger recombination of multiple exciton states with time constants of 10s of ps.[14] In the visible region (450-800 nm), a broad positive feature has been attributed to the red shift of the higher absorption band caused by the presence of 1S excitons (EIA).[34, 36-38] As indicated in Figure 4.1.C, the EIA and the 1S exciton bleach feature have identical kinetic traces, consistent with this assignment.

4.2.2. Multiple Exciton Dynamics in PbS QDs.

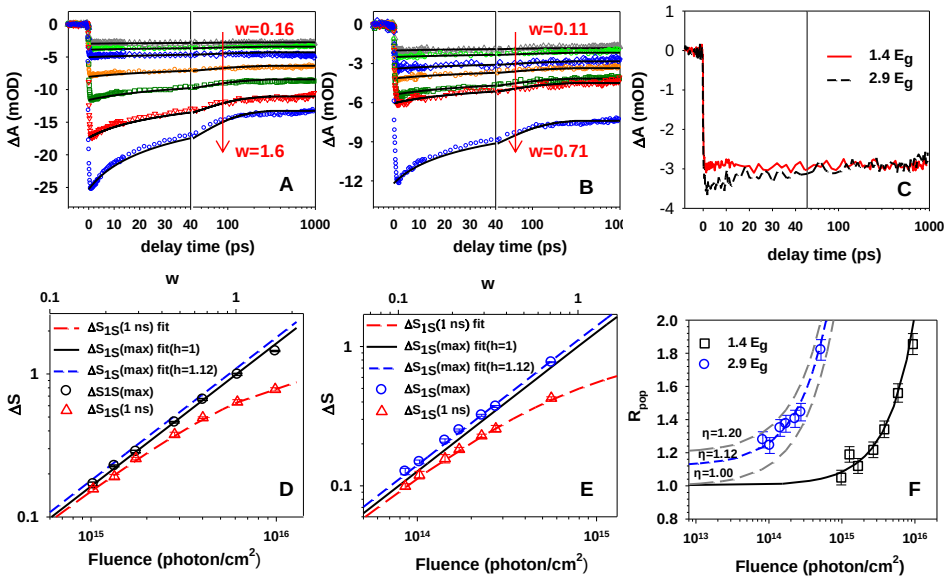

Figure 4.2. Excitation intensity dependence of 1S exciton bleach in PbS QDs. Pump intensity dependent 1S exciton bleach kinetics of PbS QDs after (A) 800 nm and (B) 400 nm excitation. The solid lines are fits according to a stochastic multiexciton annihilation model described in the main text. The intensity is indicated by the average number of absorbed photons per dot (*w*). The x-axes in A and B are in linear scale from 0-40 ps and logarithmic scale from 40-1000ps. (C) Comparison of the 1S exciton bleach kinetics at the lowest intensity of 800 nm (*w*=0.16) and 400 nm (*w*=0.11) excitation, showing significant fast decay component in the latter. Normalized 1S exciton bleach signals at early (ΔS_{1S}(max)) and long (ΔS_{1S}(1 ns)) delay times as (D) 800 and (E) 400 nm excitation. The best fit to ΔS_{1S}(1 ns) according to eq 4.2 is given by the red dashed line, from which *w* for any excitation intensities can be obtained. Fits to ΔS_{1S}(max) according to eq 4.3 with MEG efficiency of η=1 (black solid line) and 1.12 (blue dashed line) are also shown, with the latter being the best fit to the signal at 400 nm excitation. (F) The ratio (R_{pop}) of ΔS_{1S}(max)/ΔS_{1S}(1 ns) as a function of the fluence of 800 nm (black squares) and 400 nm (red circles) excitation. Best fits to these data according to eqs 4.2 and 4.3 yield η=1.00 (black solid line) for 800 nm excitation and η=1.12 (blue dashed line).for 400 nm excitation. Fits with η=1.00

and 1.20 (grey dashed lines) for the data at 400 nm excitations are also shown for comparison. Error bars in D, E, and F indicate the standard deviation of three measurements.

We investigate two approaches for quantifying the MEG efficiency. In both approaches we compare the number of excitons generated with excitations above (400 nm, 2.9 Eg) and below (800 nm, 1.45 Eg) the MEG threshold.[6, 14, 39] In the first approach for determining the MEG efficiency, we compare the excitation intensity dependent TA signals of PbS QDs at 800 nm (Figure 4.2 A) and 400 nm (Figure 4.2 B) excitation. The intensity of the pump pulse is indicated as the average number of absorbed photons per QD, *w*, which is determined by a fitting procedure to be discussed below. The complete sets of TA spectra of the sample at all the excitation intensities are shown in Appendix 1. Under the lowest intensity 800 nm excitation, the kinetic trace of 1S bleach shows negligible decay within 1 ns (Figure 4.2 A and 4.2 C), suggesting that it is dominated by long-lived single exciton states. At higher excitation intensity, the bleach kinetics show larger fast decay component due to Auger recombination of multiple excitons. Similar intensity dependence is observed with 400 nm excitation (Figure 4.2 B). A comparison of the 1S exciton bleach kinetics at the lowest intensities of 800 nm (w=0.16) and 400 nm (w=0.11) excitation is shown in Figure 4.2 C. The former shows negligible fast decay components, whereas the latter shows significant contribution of QDs with multiple exactions.

Multiple excitons can be generated by the MEG process and by the absorption of multiple photons by one quantum dot. The latter can be determined by assuming that the number of absorbed photons per QD obeys the Poisson statistics.[41, 42] However, as pointed out previously,[3, 43, 44] the large optical density at 400 nm leads to significant attenuation of the light intensity along the sample path. To simulate this scenario, we follow a previous procedure[43] and divide the cuvette into 10 slabs. Within each slab the Poisson distribution of absorbed photons is assumed:

$P_i(n) = \frac{w_i^{\,n}}{n!} e^{-w_i}$, where $P_i(n)$ is the probability of QDs with n absorbed photons and w_i is the average number of absorbed photons in slab i. w_i scales linearly with the excitation density (I_i), i.e., w_i=C·I_i. I_i varies between slabs following the Beer's law. The scaling factor, C, depending on the absorption cross-section of the sample and the overlap of the pump and probe beams, is determined from fitting the excitation intensity dependence of the 1S exciton bleach signal amplitude. The average number of absorbed photons (w) throughout the sample is given by $w = \sum_{i=1}^{10} \frac{1}{10} \sum_{n=0}^{\infty} n P_{w_i}(n)$.

At long delay time (~1 ns after excitation), when all multiple exciton states have decayed by exciton-exciton annihilation and only single exciton states remain, the probability of QDs with single exciton is the same as the probability of all excited QDs. Therefore, the transient absorption signal at 1S bleach at 1 ns is given by[42]

$$\Delta A_{1S}(1ns) = \sum_{i=1}^{10} \frac{1}{8} C_0 \frac{L}{10} \varepsilon_{1S} \sum_{n=1}^{\infty} P_{w_i}(n) = A_{1S} \frac{1}{10} \sum_{i=1}^{10} [1 - P_{w_i}(0)] \qquad (4.1)$$

where C_0 is the QD concentration, L the sample path length, and ε_{1S} (A_{1S}) the extinction coefficient (absorbance) at the 1S exciton band. The 1/8 factor accounts for the state filling contribution of one exciton to the bleach of the 8-fold degenerate 1S exciton band. We define a normalized transient bleach signal at long delay time

$$\Delta S_{1S}(1ns) = \Delta A_{1S}(1ns) / (\frac{1}{8} A_{1S}) = \frac{1}{10} \sum_{i=1}^{10} [1 - P_{w_i}(0)] \qquad (4.2)$$

which represents the average number of excited QDs. At early delay time (~1-2 ps after excitation), the annihilation of the multiple exciton is negligible due to the long Auger lifetime (10s-100s ps). The normalized transient bleach signal at this time is given by

$$\Delta S_{1S}(\max) = \Delta A_{1S}(\max) / (\frac{1}{8} A_{1S}) = \frac{1}{10} \sum_{i=1}^{10} \eta \cdot [n \times \sum_{n=1}^{7} P_w(n) + 8 \times \sum_{n=8}^{\infty} P_w(n)] \qquad (4.3)$$

Inside the square bracket of this expression, the first term represents the contribution of QDs with less than 8 excitons and the second term the contribution from QDs with 8 or more excitons. The MEG efficiency, η, accounts for the increase of the total number of excitons due to the MEG process. At 800 nm pulse excitation, MEG is excluded due to energy conservation (η = 1). For 400 nm pulse excitation, η is set as a free fitting parameter. The normalized transient signals at early and long decay times as a function of photon fluence (bottom x-axis) are shown in Figure 4.2 D and 4.2 E for 800 nm and 400 nm excitations, respectively. Figure 4.2 F shows the ratio of the initial and final bleach amplitudes ($R_{pop}= \Delta S_{1S}(\max) / \Delta S_{1S}(1ns)$) as a function of pump fluence, which is often used to determine the MEG efficiency in the literature.[5, 14, 32] These signals can be well fit according to eqs 4.2 and 4.3 with scaling factor C (C, and η) as the fitting parameters for 800 nm (400 nm) excitation. From the best fit, *w*, the average number of absorbed photons is determined and plotted as the top x-axis of Figures 4.2 D and 4.2 E. The MEG efficiency η is determined to be 112±2 % at 400 nm excitation, consistent with the recently reported values for PbS NCs.[13]

The decay kinetics of the 1S exciton bleach in Figures 4.2 A and 4.2 B reflects the exciton-exciton annihilation in the QDs. We fit these kinetics following a stochastic model, in which the multi-exiton states are assumed to decay sequentially from n+1 to n exciton states. The rate equation governing the population kinetics of the n-exciton state N(n,t) is given by

$$\frac{dN(n,t)}{dt} = \frac{N(n+1,t)}{\tau_{n+1}} - \frac{N(n,t)}{\tau_n} \qquad (4.4)$$

In this equation, the decay rate of the n-exciton states ($1/\tau_n$) is assumed to be dominated by Auger recombination and scales with n following an independent carrier model, $\frac{1}{\tau_n} = \frac{1}{2} n^2 (n-1) k_A$.[27, 45-48] Here k_A is the Auger recombination rate constant and is related to the bi-exciton state

lifetime, $\frac{1}{\tau_2} = 2k_A$. The initial distribution of excitons at any given excitation intensity has already been determined by the analysis described above. The decay kinetics at all the excitation intensities can be simultaneous fit by eq 4.4 with k_A (or τ_2) as the only fitting parameter. As shown in Figures 4.2 A and 4.2 B, these kinetics are well described by this model, yielding bi- and tri-exciton lifetimes of 49 and 11 ps, respectively. This scaling law suggests that electrons and holes act as independent carriers in the Auger recombination process, consistent with previously reported multiexciton Auger recombination mechanisms in related QDs.[45, 46]

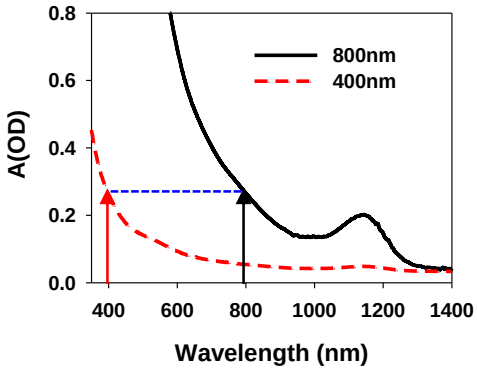

Figure 4.3. Absorption spectra of PbS QD samples for 400 nm (sample A, red dashed line) and 800 nm (sample B, black line) excitation. The arrows indicate that the two samples have the same OD at their respective excitation wavelengths.

In the second approach, we adopt a procedure developed by Ruhman and co-workers.[9, 40] Briefly, in this experiment, the concentration of the samples as well as the pump intensities was carefully controlled so as to obtain the same average exciton per QD distribution under 400 and 800 nm excitation, under such conditions, any difference in the number of generated exitons for 400 nm excitation can thus be attributed to the MEG process. Quantitatively, according to the Beer-Lambert law, the average excitons per QDs as function of the light path can be written as

$$w(l) = \frac{J_0 e^{-\sigma l c}}{c} \qquad (4.5)$$

where l is the light path, J_0 is the photon flux of the pump, σ is the absorption cross section of QD at pump wavelength, and c is the concentration of the QD solution. To achieve the identical $w(l)$ at two excitation wavelength, according to eq 4.5, the relationships, $\sigma_{400nm}c_{400nm} = \sigma_{800nm}c_{800nm}$ and $J_0(400nm)/c_{400nm} = J_0(800nm)/c_{800nm}$, must be satisfied. Since σ_{400nm} is 10 times larger than σ_{800nm}, the concentration of the QDs for 400 nm excitation is 10 times diluted than that for 800 nm excitation. As Figure 4.3, the same OD of the two samples at their respective excitation wavelengths suggests that the first relationship is satisfied. In TA measurement, we also adjusted the photon flux of the pumps to ensure $J_0(400nm) = \frac{1}{10}J_0(800nm)$ so that the second relationship is also satisfied.

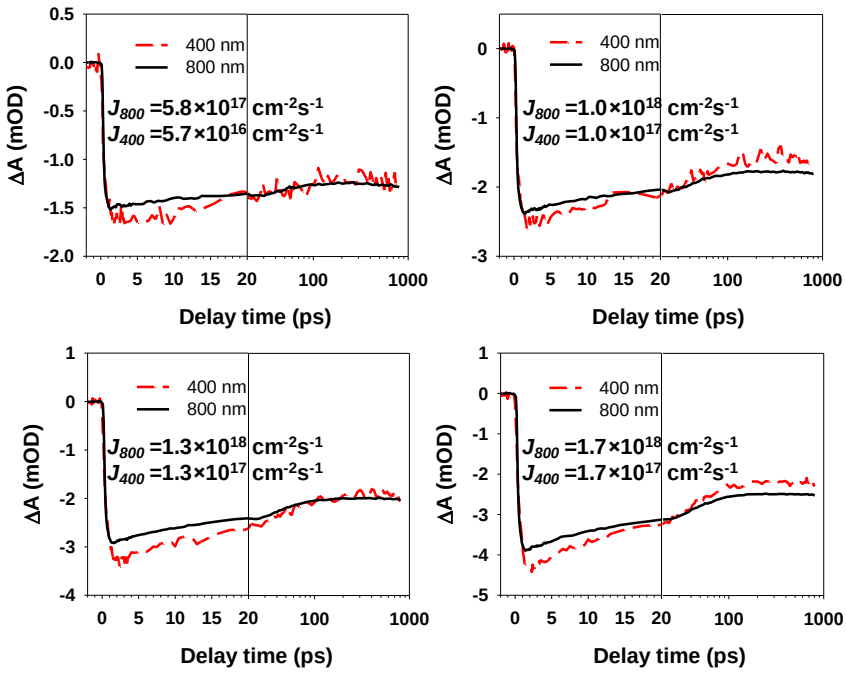

Figure 4.4. Comparison of 1S exciton bleach kinetics of PbS QD samples, pumped at 400 nm (red-dash lines) and 800 nm (black solid lines), at indicated excitation photon fluxes for four independent measurements. The kinetics for 800 nm excitations is scaled down by a factor of 10.

Comparisons of 1S exciton bleach kinetics of PbS QD samples pumped by 400 and 800 nm pulses are shown in Figure 4.4. The kinetics for 800 nm excitations is scaled down by a factor of 10 due to its 10-fold higher concentration. We find that, after correcting the relative concentrations of QDs, the initial 1S bleach amplitude at 400 nm excitation is larger than that at 800 nm excitation, suggesting the occurrence of MEG. The MEG efficiency of 113±3 % at 400 nm excitation is determined by ratio of the maximum 1S bleach signal of 400 nm excitation to the corrected maximum 1S bleach signal of 800 nm excitation, in agreement with that obtained from the first approach described above. However, the accuracy of this measurement depends critically on the ability to measure the relative photon flux of the 400 and 800 nm excitation beams, which can be difficult because of the variations of beam profiles and pump/probe overlap.

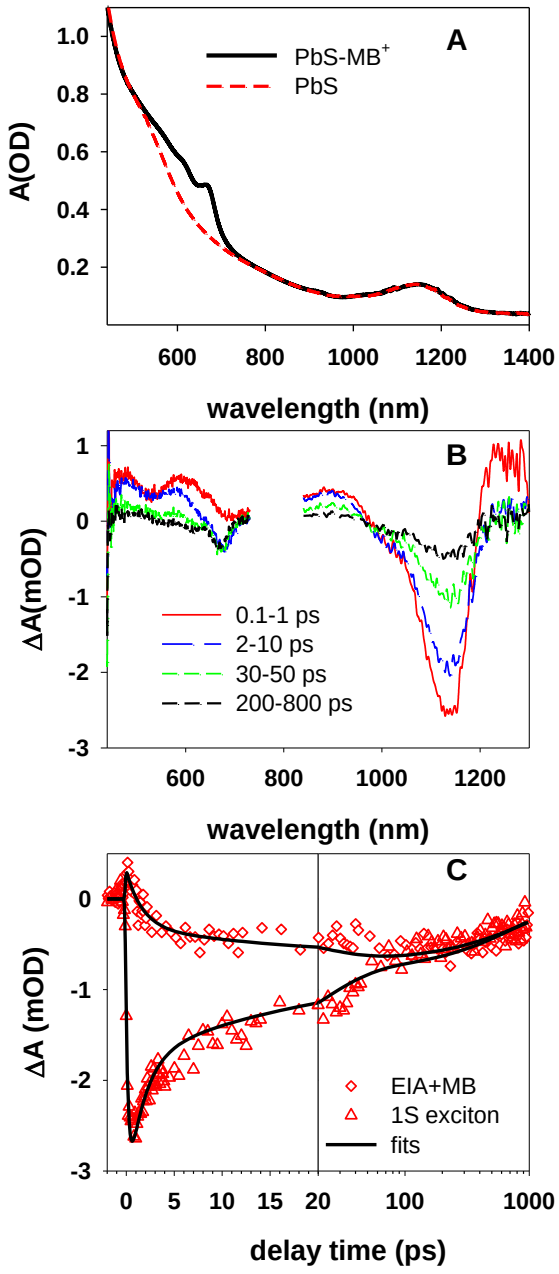

Figure 4.5. Transient spectra and kinetics of PbS-MB$^+$ complexes. (A) Static absorption spectrum of PbS QDs (red dash line) and PbS-MB$^+$ complexes (black solid line). (B) TA spectra of PbS-MB$^+$ complexes at indicated delay time windows after 800 nm excitation at the lowest fluence (w= 0.11). (C) TA kinetics of PbS-MB$^+$ complexes at 667 nm (EIA+MB) and at 1140 nm (1S exciton). The kinetics of EIA+MB has been normalized to the kinetic of 1S bleach at later delay

time for better comparison. Also shown are the fits of these kinetic traces (black solid lines). The x-axes in panel C is in linear scale from 0-20 ps and logarithmic scale from 20-1000ps.

4.2.3. Single Exciton Dissociation in PbS-MB^+.

Compared with free QDs, the absorption spectrum of PbS-MB^+ complexes (Figure 4.5 A) has an additional absorption band at 667 nm that corresponds to the ground state absorption of MB^+. We first examine the exciton dissociation dynamics in the complex with 800 nm pulse excitation at the lowest intensity, under which condition the majority of the excited QDs are in single exciton states. TA spectra of the complex at indicated delay times are shown in Figure 3B. In addition to the 1S exciton bleach at 1140 nm, MB^+ ground state bleach (GSB) at 667 nm, arising from the reduction of MB^+, is also observed, although it overlaps with the broad EIA feature (450-800nm). Unfortunately, because of the lack of probe light at < 450 nm (caused by the strong absorption of QDs), we could not monitor the anion absorption band of the MB^+ molecule at 420 nm.[49] In contrast to the long-lived 1S exciton bleach observed in free QDs, the 1S exciton bleach of the complex recovers over 90% within 1 ns due to the charge separation and recombination processes (Figure 4.5 C). A detailed assignment of the electron and hole features and analysis of kinetics of related PbS-MB^+ complexes have been discussed in Chapter 3. Following the same analysis, the kinetic traces in panel C is simultaneously fit, from which the half lifetimes of charge separation and recombination are determined to be 2.3 ps and 0.8 ns, respectively. Therefore, single excitons in PbS-MB^+ complexes can be efficiently dissociated by ultrafast electron transfer to MB^+.

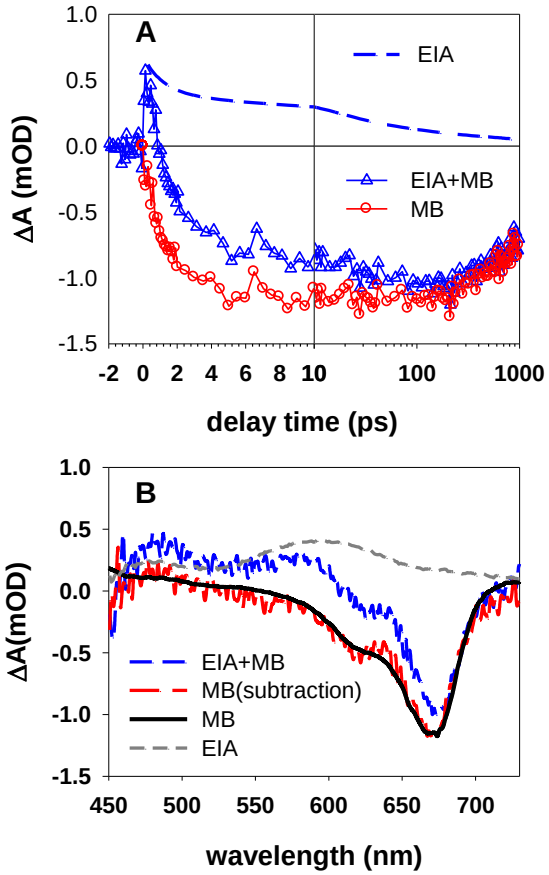

Figure 4.6. MB^+ ground state transient bleach kinetics and spectrum in PbS-MB^+ complexes. (A) Kinetic trace of MB^+ GSB (red open circles) obtained by subtracting the simulated EIA kinetics (blue long-dash line) from the total signal of EIA and MB GSB^+ (blue triangles) at 667 nm. The x-axes in the panel A is in linear scale from 0-10 ps and logarithmic scale from 10-1000ps. (B) TA spectrum of MB^+ at 80 ps (red long-dash line) obtained by subtracting the simulated EIA spectrum (gray short-dash line) from the total spectrum (blue medium-dash line) of MB^+ and EIA. The procedure yields a MB^+ bleach spectrum that is in excellent agreement with the MB^+ TA spectra obtained from CdSe-MB^+ complexes at 100 ns (black solid line). The TA spectra and kinetics were obtained with 800 nm excitation at a fluence of w=0.46

4.2.4. MEG and MED in PbS-MB^+ complexes.

To quantify the number of dissociated excitons in the PbS-MB^+ complex, pump intensity dependent measurements were also conducted. The complete sets of TA spectra of the complex at all the excitation intensities are shown in Appendix 1. Because MB^+ has negligible absorption at 800 or 400 nm, under the same excitation conditions, the number of absorbed photons per QD should be the same in PbS-MB^+ complexes and free QDs and has been determined above. Excitons in the PbS-MB^+ complex can be dissociated by electron transfer to MB^+ to form methylene blue radicals. The quantum yield for this process can be quantified by measuring the amplitude of the MB^+ GSB. However, due to the overlap of the MB^+ GSB and EIA signal, the contribution of the EIA signal has to be subtracted from the total signal at 667 nm. As shown in Figure 4.6 A, the EIA contribution can be simulated by scaling the fit of 1S exciton bleach kinetics of PbS-MB^+ because EIA has the same decay kinetics as 1S bleach. The scaling factor is obtained from the ratio of amplitudes of EIA at 667 nm to 1S exciton bleach at 1140 nm in free QDs. The growth of the pure MB^+ bleach signal that is obtained by subtracting EIA contribution from the overlapping signal is in agreement with exciton dissociation kinetics. The TA spectra of MB^+ can also be obtained by applying this subtraction procedure. The TA spectrum of MB^+ at 80 ps, obtained by this subtraction procedure (Figure 4.6 B), agrees with the TA spectrum of MB^+ bleach (black solid line) in CdSe-MB^+ complexes. The excellent agreement confirms the validity of the subtraction procedure.

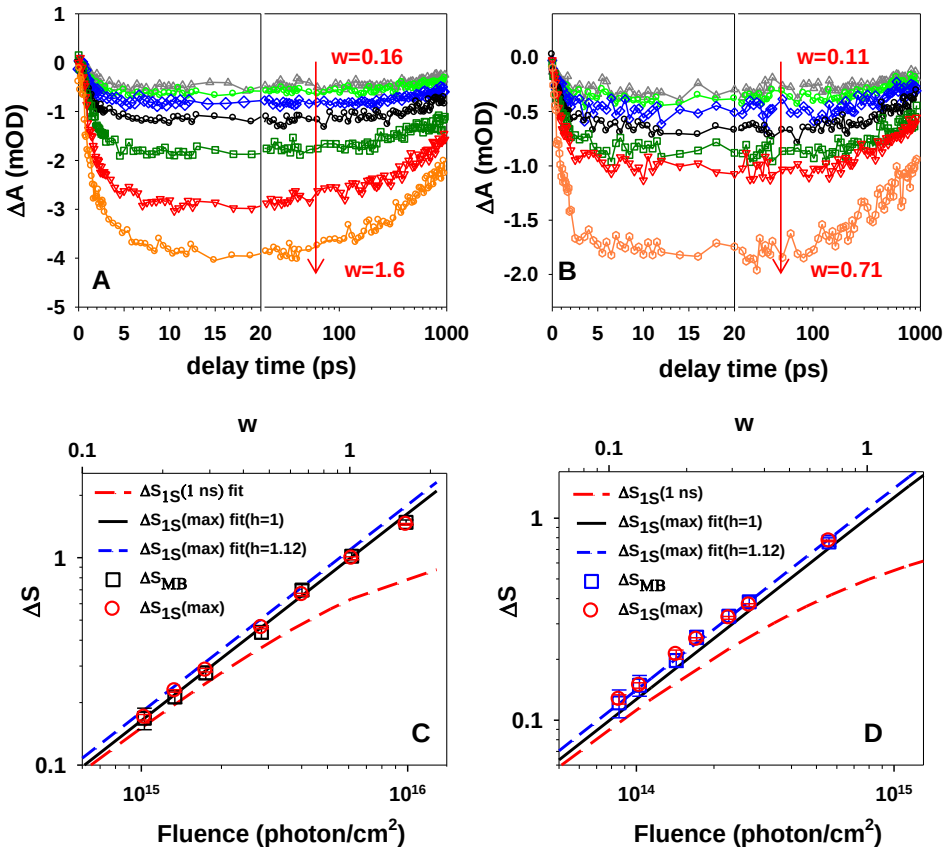

Figure 4.7. Excitation intensity dependence of MB^+ bleach in PbS-MB^+ complexes. Pump intensity dependent MB^+ GSB kineticsat 800 (A) and 400 nm (B) excitation. The experiments were conducted under the same excitation conditions as those for free QDs. The x-axes in panel A and B are in linear scale from 0-20 ps and logarithmic scale from 20-1000 ps. Normalized TA signal amplitude of MB^+ GSB as a function of the average number of absorbed photons per dot (top x-axis) and photon fluence (bottom x-axis) at 800 nm (C) and 400 nm (D) excitation. The normalized MB^+ GSB amplitude is proportional to the measured maximum MB^+ GSB bleach according to the scaling procedure described in the text. The error bars indicate the standard deviation of three measurements. Also shown in these two panels are normalized transient 1S exiton bleach signal, ΔS(max), and fits according to eq 4.3.

Figure 4.7 A and B show the subtracted MB^+ bleach kinetics under different intensities of 800 nm and 400 nm excitation, respectively. Because the charge separation process is much faster than the recombination, the maximum amplitudes of the GSB signals (ΔA_{MB}) indicate the total number of reduced MB^+ (and the total number of dissociated excitons). To improve signal to noise, we use the averaged value from 25-40 ps to represent ΔA_{MB}. We defined $\Delta S_{MB} = \Delta A_{MB} / \alpha(MB)$ to represent the average number of reduced MB^+ molecules per QD.[27] The scaling factor $\alpha(MB)$ can be obtained in the following way. Under the lowest intensity of 800 nm excitation (w=0.16), the excited QDs are dominated by single exciton states that are long lived (>> 1ns) in free QDs. Because of the ultrafast ET rate ($t_{1/2}$=2.3 ps), a unity quantum yield of exciton dissociation in PbS-MB^+ complexes and $\Delta S_{MB} = w$ can be assumed, from which the scaling factor $\alpha(MB)$ is determined. The same scaling factor is applied to ΔA_{MB} signals measured at higher excitation intensities. ΔS_{MB} as a function of photon fluence (bottom x-axis) and w (top x-axis) is shown in Figure 4.7 C and D for 800 nm and 400 nm excitation, respectively. It is clear that ΔS_{MB} follows ΔS_{1S}(max), indicating that all excitons (generated by MEG and multi-photon absorption) are dissociated by electron transfer to MB^+. This finding is consistent with the fact that the electron transfer rate in PbS-MB^+ complexes is much faster than the annihilation rates of biexciton and triexciton states (the dominating multi-exciton states generated under our excitation conditions). This finding also implies that the MEG efficiency in PbS-MB^+ complexes is the same as that in free QDs, unaffected by the presence of the electron acceptors.

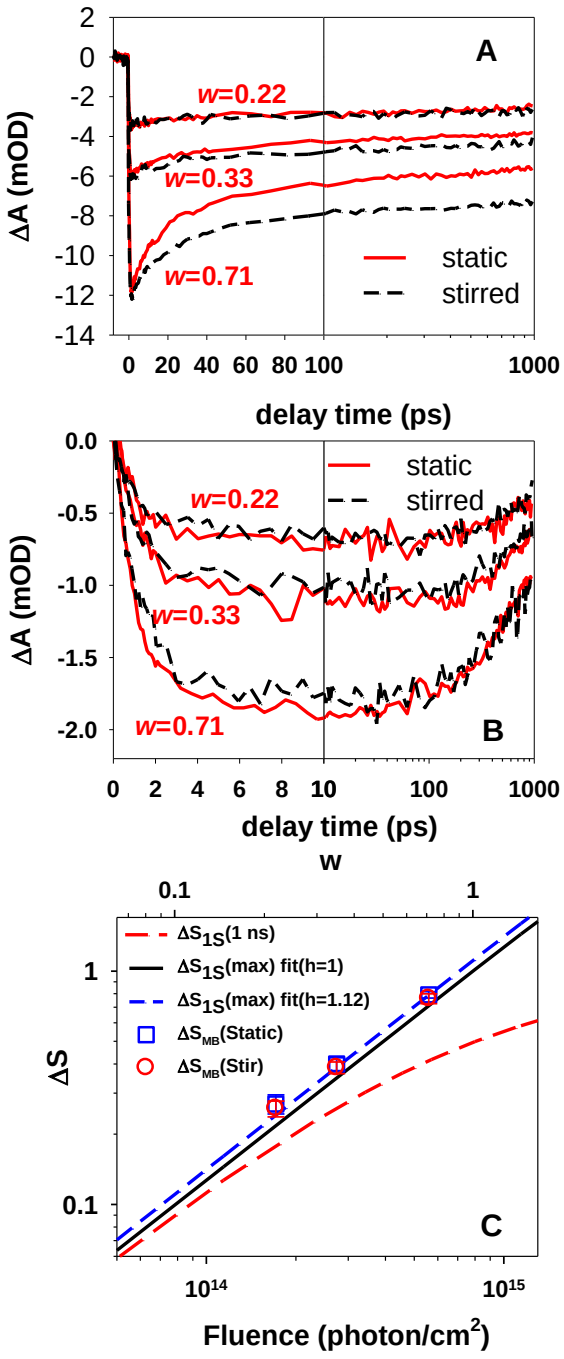

Figure 4.8. Comparison of (A) 1S exciton bleach and (B) MB^+ GSB bleach of static (red solid line) and stirred (black dashed line) PbS-MB^+ solutions under indicated intensity of 400 nm excitation. The x-axes in panel A and B are in linear scale from 0-100 ps and logarithmic scale from 100- 1000 ps. (C) Normalized MB^+ GSB amplitudes of the stirred and static QD-MB^+ solution as a function of *w* (top x-axis) and photon fluence (bottom x-axis). The error bars

indicate the standard deviation of three measurements. Also shown in panel C are fits according to eqs 4.2 and 4.3.

4.2.5. Effect of the charged PbS-MB^+ complexes.

Because QDs are usually immobilized in practical devices, continuous exposure can lead to charged QDs with shortened exciton lifetime.[44, 51, 52] In measurements where the ratio of fast decay (multi-exciton states) vs long-lived (single exciton) 1S exiton bleach components is used to determine the MEG efficiency, the charging of QDs in static samples is known to lead to erroneous high apparent MEG efficiencies.[13] In this experiment, we exposed the static samples to 400 nm excitation for 30 minutes to generate charged QDs in the excitation volume prior to TA measurement. Compared with the stirred sample, 1S exciton bleach of free QDs in the static and pretreated samples has a similar initial amplitude but recovers significantly faster, especially under higher excitation intensity (Figure 4.8 A), due to faster Auger recombination in charged QDs.[53] However, as shown in Figure 4.8 B, the difference between the MB^+ GSB kinetic traces of the static and stirred PbS-MB^+ samples is negligible, indicating that Auger recombination in charge QDs does not compete with the ultrafast electron transfer process and excitons are still efficiently dissociated in charged QD/MB^+ complexes. The normalized MB^+ GSB signals as a function of excitation intensity for the static/pretreated PbS-MB^+ sample is shown in Figure 6 C. These data points are also well fit by eq 3 with η =114±7%. It suggests that the efficiencies of MEG and MED are not significantly affected by the charging of QDs in the QD-acceptor complexes.

4.3. Conclusion.

In summary, we have investigated multiple exciton generation and annihilation dynamics in PbS QDs and multiple excition dissociation dynamics in PbS-MB^+ complexes by TA spectroscopy. The MEG yield of the QD at 400 nm excitation is determined to be 112±2 %. The number of dissociated excitons in the PbS-MB^+ complexes equals to the excitons generated in free QDs under the same excitation conditions, indicating that MEG is not affected by the adsorbed MB^+ molecules and all multiple excitons can be dissociated before exciton-exciton annihilation. Furthermore, charging of QDs in static samples of PbS and PbS-MB^+ does not affect the MEG and MED efficiencies.

Reference

1. Schaller, R. D.; Klimov, V. I. *Phys. Rev. Lett.* **2004,** 92, (18), 186601.

2. Ellingson, R. J.; Beard, M. C.; Johnson, J. C.; Yu, P. R.; Micic, O. I.; Nozik, A. J.; Shabaev, A.; Efros, A. L. *Nano Lett.* **2005,** 5, (5), 865-871.

3. Trinh, M. T.; Houtepen, A. J.; Schins, J. M.; Hanrath, T.; Piris, J.; Knulst, W.; Goossens, A. P. L. M.; Siebbeles, L. D. A. *Nano Lett.* **2008,** 8, (6), 1713-1718.

4. Ji, M. B.; Park, S.; Connor, S. T.; Mokari, T.; Cui, Y.; Gaffney, K. J. *Nano Lett.* **2009,** 9, (3), 1217-1222.

5. Cunningham, P. D.; Boercker, J. E.; Foos, E. E.; Lumb, M. P.; Smith, A. R.; Tischler, J. G.; Melinger, J. S. *Nano Lett.* **2011,** 11, (8), 3476-3481.

6. Nootz, G.; Padilha, L. A.; Levina, L.; Sukhovatkin, V.; Webster, S.; Brzozowski, L.; Sargent, E. H.; Hagan, D. J.; Van Stryland, E. W. *Phys. Rev. B* **2011,** 83, (15), 155302.

7. Pijpers, J. J. H.; Ulbricht, R.; Tielrooij, K. J.; Osherov, A.; Golan, Y.; Delerue, C.; Allan, G.; Bonn, M. *Nat. Phys.* **2009,** 5, (11), 811-814.

8. Nair, G.; Bawendi, M. G. *Phys. Rev. B* **2007,** 76, (8), 081304.

9. Gdor, I.; Sachs, H.; Roitblat, A.; Strasfeld, D. B.; Bawendi, M. G.; Ruhman, S. *ACS Nano* **2012,** 6, (4), 3269-3277.

10. Nair, G.; Geyer, S. M.; Chang, L.-Y.; Bawendi, M. G. *Phys. Rev. B* **2008,** 78, (12), 125325.

11. Miaja-Avila, L.; Tritsch, J. R.; Wolcott, A.; Chan, W. L.; Nelson, C. A.; Zhu, X. Y. *Nano Lett.* **2012,** 12, (3), 1588-1591.

12. Trinh, M. T.; Polak, L.; Schins, J. M.; Houtepen, A. J.; Vaxenburg, R.; Maikov, G. I.; Grinbom, G.; Midgett, A. G.; Luther, J. M.; Beard, M. C.; Nozik, A. J.; Bonn, M.; Lifshitz, E.; Siebbeles, L. D. A. *Nano Lett.* **2011,** 11, (4), 1623-1629.

13. McGuire, J. A.; Sykora, M.; Joo, J.; Pietryga, J. M.; Klimov, V. I. *Nano Lett.* **2010,** 10, (6), 2049-2057.

14. Stewart, J. T.; Padilha, L. A.; Qazilbash, M. M.; Pietryga, J. M.; Midgett, A. G.; Luther, J. M.; Beard, M. C.; Nozik, A. J.; Klimov, V. I. *Nano Lett.* **2011,** 12, (2), 622-628.

15. Hanna, M. C.; Nozik, A. J. *J. Appl. Phys.* **2006,** 100, (7), 074510-8.

16. Delerue, C.; Allan, G.; Pijpers, J. J. H.; Bonn, M. *Phys. Rev. B* **2010,** 81, (12), 125306.

17. Sukhovatkin, V.; Hinds, S.; Brzozowski, L.; Sargent, E. H. *Science* **2009,** 324, (5934), 1542-1544.

18. Sambur, J. B.; Novet, T.; Parkinson, B. A. *Science* **2010,** 330, (6000), 63-66.

19. Semonin, O. E.; Luther, J. M.; Choi, S.; Chen, H.-Y.; Gao, J.; Nozik, A. J.; Beard, M. C. *Science* **2011,** 334, (6062), 1530-1533.

20. Boulesbaa, A.; Issac, A.; Stockwell, D.; Huang, Z.; Huang, J.; Guo, J.; Lian, T. *J. Am. Chem. Soc.* **2007,** 129, (49), 15132-15133.

21. Huang, J.; Stockwell, D.; Huang, Z.; Mohler, D. L.; Lian, T. *J. Am. Chem. Soc.* **2008,** 130, (17), 5632-5633.

22. El-Sayed, M. A. *Acc. Chem. Res.* **2004,** 37, (5), 326-333.

23. Tagliazucchi, M.; Tice, D. B.; Sweeney, C. M.; Morris-Cohen, A. J.; Weiss, E. A. *ACS Nano* **2011,** 5, (12), 9907-9917.

24. Morris-Cohen, A. J.; Frederick, M. T.; Cass, L. C.; Weiss, E. A. *J. Am. Chem. Soc.* **2011,** 133, (26), 10146-10154.

25. Tvrdy, K.; Frantsuzov, P. A.; Kamat, P. V. *Proc. Natl. Acad. Sci. U. S. A.* **2011,** 108, (1), 29-34.

26. Robel, I.; Kuno, M.; Kamat, P. V. *J. Am. Chem. Soc.* **2007,** 129, (14), 4136-+.

27. Zhu, H.; Song, N.; Rodríguez-Córdoba, W.; Lian, T. *J. Am. Chem. Soc.* **2012,** 134, (9), 4250-4257.

28. Huang, J.; Huang, Z. Q.; Yang, Y.; Zhu, H. M.; Lian, T. Q. *J. Am. Chem. Soc.* **2010,** 132, (13), 4858-4864.

29. Matylitsky, V. V.; Dworak, L.; Breus, V. V.; Basche, T.; Wachtveitl, J. *J. Am. Chem. Soc.* **2009,** 131, (7), 2424.

30. Beard, M. C.; Midgett, A. G.; Law, M.; Semonin, O. E.; Ellingson, R. J.; Nozik, A. J. *Nano Lett.* **2009,** 9, (2), 836-845.

31. Isborn, C. M.; Prezhdo, O. V. *J. Phys. Chem. C* **2009,** 113, (29), 12617-12621.

32. Luther, J. M.; Beard, M. C.; Song, Q.; Law, M.; Ellingson, R. J.; Nozik, A. J. *Nano Lett.* **2007,** 7, (6), 1779-1784.

33. Yang, Y.; Rodríguez-Córdoba, W.; Xiang, X.; Lian, T. *Nano Lett.* **2011,** 12, (1), 303-309.

34. Yang, Y.; Rodríguez-Córdoba, W.; Lian, T. *J. Am. Chem. Soc.* **2011,** 133, (24), 9246-9249.

35. Wehrenberg, B. L.; Guyot-Sionnest, P. *J. Am. Chem. Soc.* **2003,** 125, (26), 7806-7807.

36. Kohn, S. E.; Yu, P. Y.; Petroff, Y.; Shen, Y. R.; Tsang, Y.; Cohen, M. L. *Phys. Rev. B* **1973,** 8, (4), 1477-1488.

37. Kanazawa, H.; Adachi, S. *J. Appl. Phys.* **1998,** 83, (11), 5997-6001.

38. Cho, B.; Peters, W. K.; Hill, R. J.; Courtney, T. L.; Jonas, D. M. *Nano Lett.* **2010,** 10, (7), 2498-2505.

39. McGuire, J. A.; Joo, J.; Pietryga, J. M.; Schaller, R. D.; Klimov, V. I. *Acc. Chem. Res.* **2008,** 41, (12), 1810-1819.

40. Ben-Lulu, M.; Mocatta, D.; Bonn, M.; Banin, U.; Ruhman, S. *Nano Lett.* **2008,** 8, (4), 1207-1211.

41. Song, N.; Zhu, H.; Jin, S.; Zhan, W.; Lian, T. *ACS Nano* **2010,** 5, (1), 613-621.

42. Klimov, V. I. *Annu. Rev. Phys. Chem.* **2007,** 58, 635-673.

43. Beard, M. C.; Knutsen, K. P.; Yu, P.; Luther, J. M.; Song, Q.; Metzger, W. K.; Ellingson, R. J.; Nozik, A. J. *Nano Lett.* **2007,** 7, (8), 2506-2512.

44. Nair, G.; Chang, L.-Y.; Geyer, S. M.; Bawendi, M. G. *Nano Lett.* **2011,** 11, (5), 2145-2151.

45. Klimov, V. I.; Mikhailovsky, A. A.; McBranch, D. W.; Leatherdale, C. A.; Bawendi, M. G. *Science* **2000,** 287, (5455), 1011-1013.

46. Klimov, V. I.; McGuire, J. A.; Schaller, R. D.; Rupasov, V. I. *Phys. Rev. B* **2008,** 77, (19), 195324.

47. Hilczer, M.; Tachiya, M. *J. Phys. Chem. C* **2009,** 113, (43), 18451-18454.

48. Barzykin, A. V.; Tachiya, M. *J. Phys.: Condens. Matter* **2007,** 19, (6), 065105.

49. Kamat, P. V.; Dimitrijevic, N. M.; Fessenden, R. W. *J. Phys. Chem.* **1987,** 91, (2), 396-401.

50. Zhu, H. M.; Yang, Y.; Song, N. H.; Rodriguez-Cordoba, W.; Lian, T. Q., Controlling Interfacial Charge Separation and Recombination Dynamics in QDs by Wave Function Engineering. In *Physical Chemistry of Interfaces and Nanomaterials X*, Silva, C., Ed. Spie-Int Soc Optical Engineering: Bellingham, 2011; Vol. 8098.

51. Tyagi, P.; Kambhampati, P. *J. Chem. Phys.* **2011,** 134, (9), 094706-10.

52. Jin, S.; Lian, T. *Nano Lett.* **2009,** 9, (6), 2448-2454.

53. Jha, P. P.; Guyot-Sionnest, P. *ACS Nano* **2009,** 3, (4), 1011-1015.

Appendix 1.

The TA spectra of PbS QD and PbS-MB$^+$ at different excitation intensities.

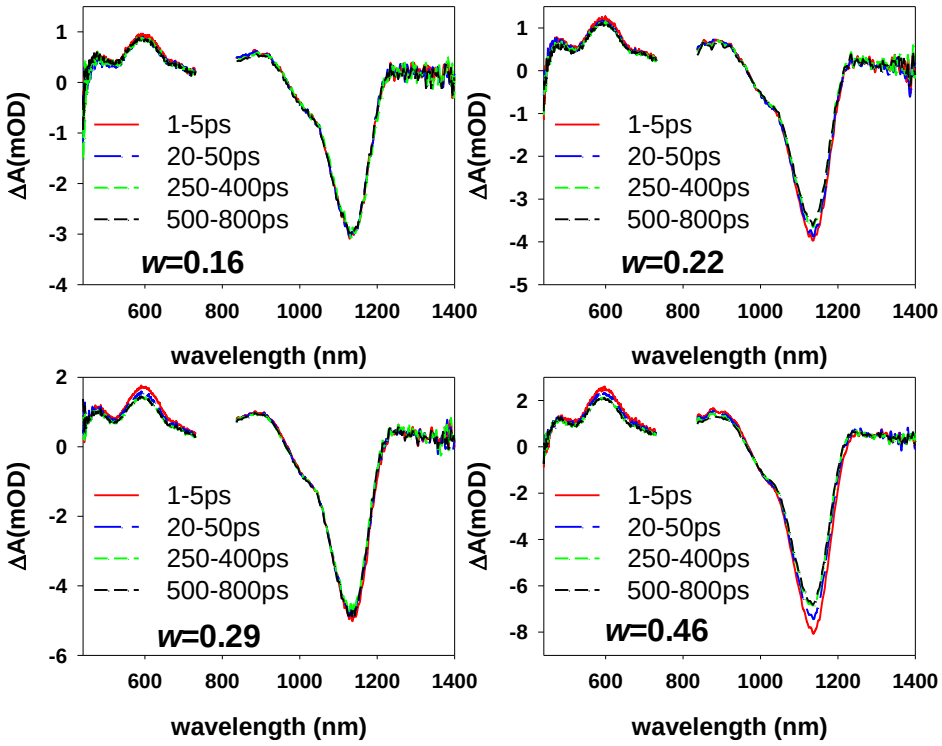

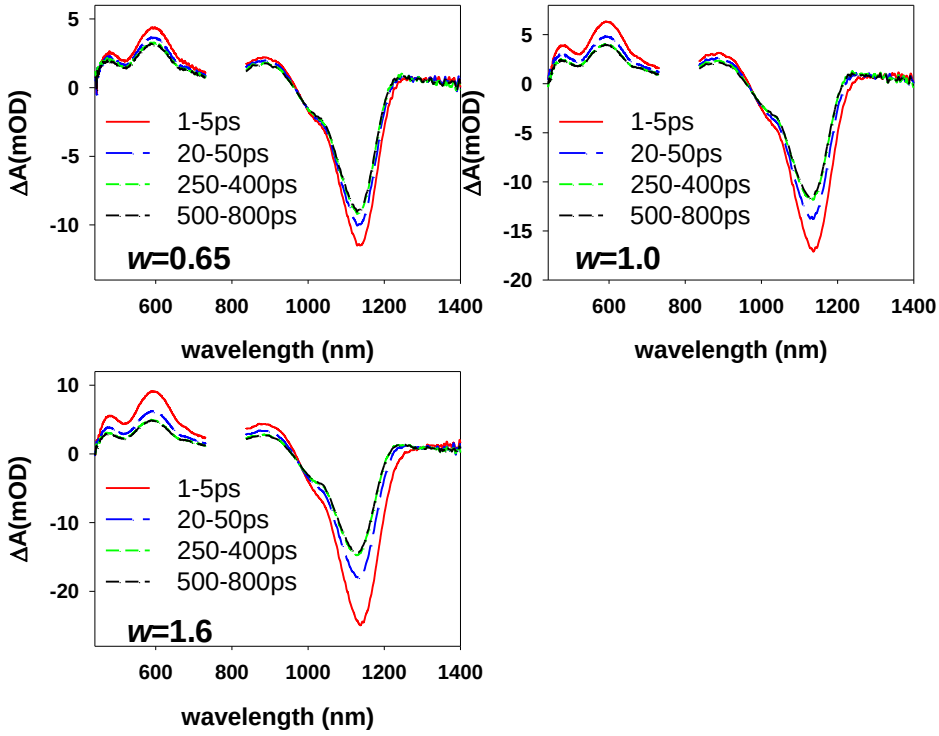

Figure A.4.1. TA spectra of PbS QDs under different intensities of 800 nm pump. The average number of absorbed photons per QD is indicated in each panel.

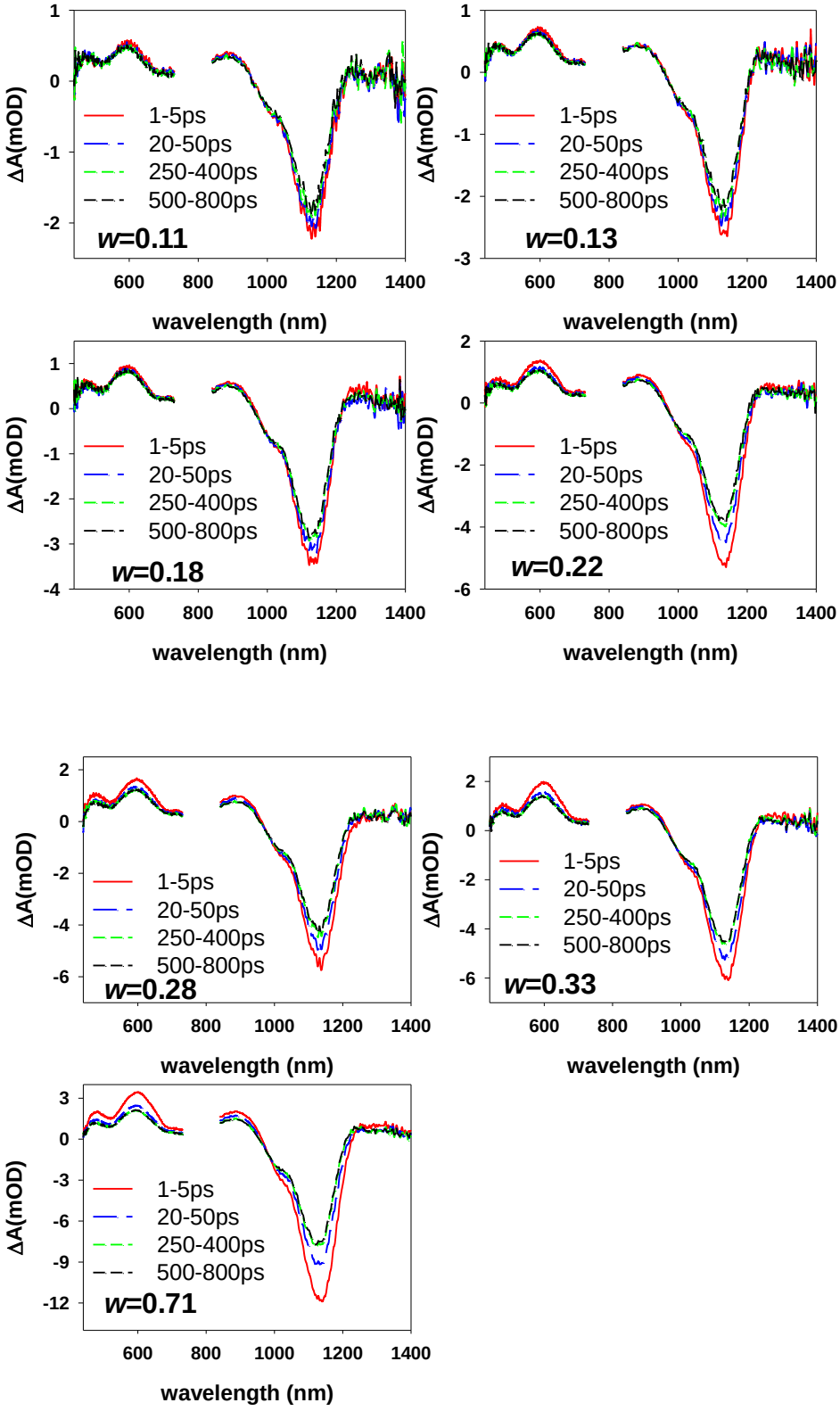
ΔA(mOD)
wavelength (nm)
1-5ps
20-50ps
250-400ps
500-800ps
w=0.11
w=0.13
w=0.18
w=0.22
w=0.28
w=0.33
w=0.71

Figure A.4.2. TA spectra of PbS QDs under different intensities of 400 nm pump. The average number of absorbed photons per QD is indicated in each panel.

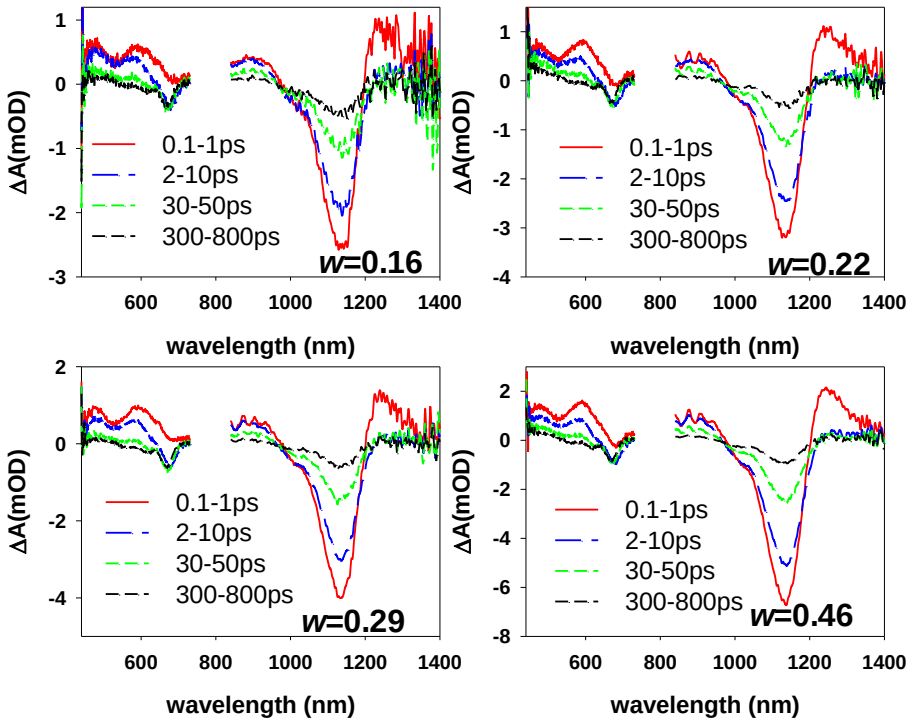

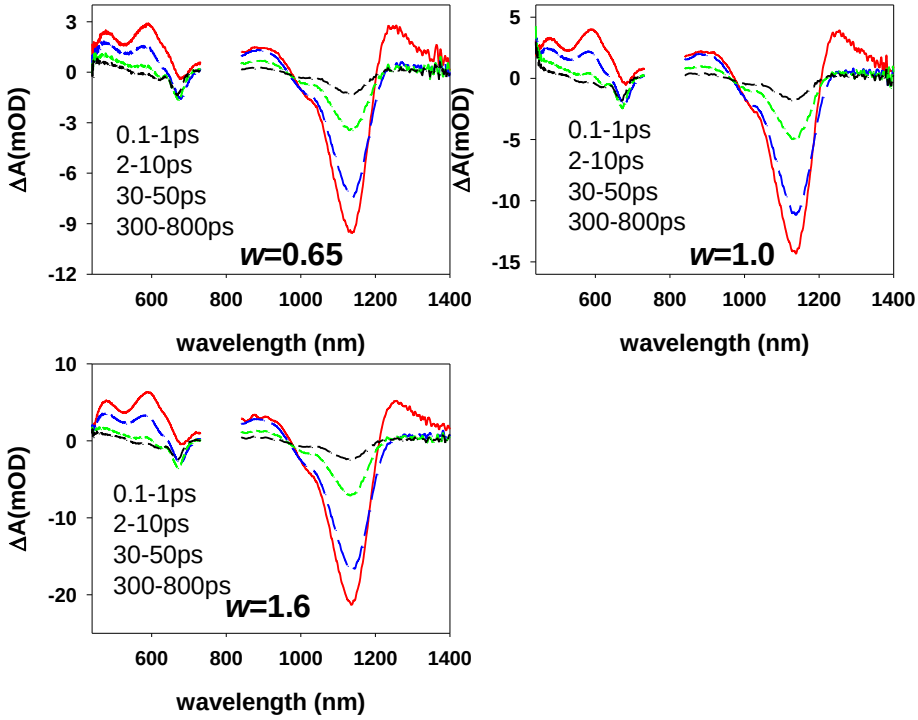

Figure A.4.3. TA spectra of PbS-MB+ complexes under different intensities of 800 nm pump. The average number of excitons per QD is indicated in each panel.

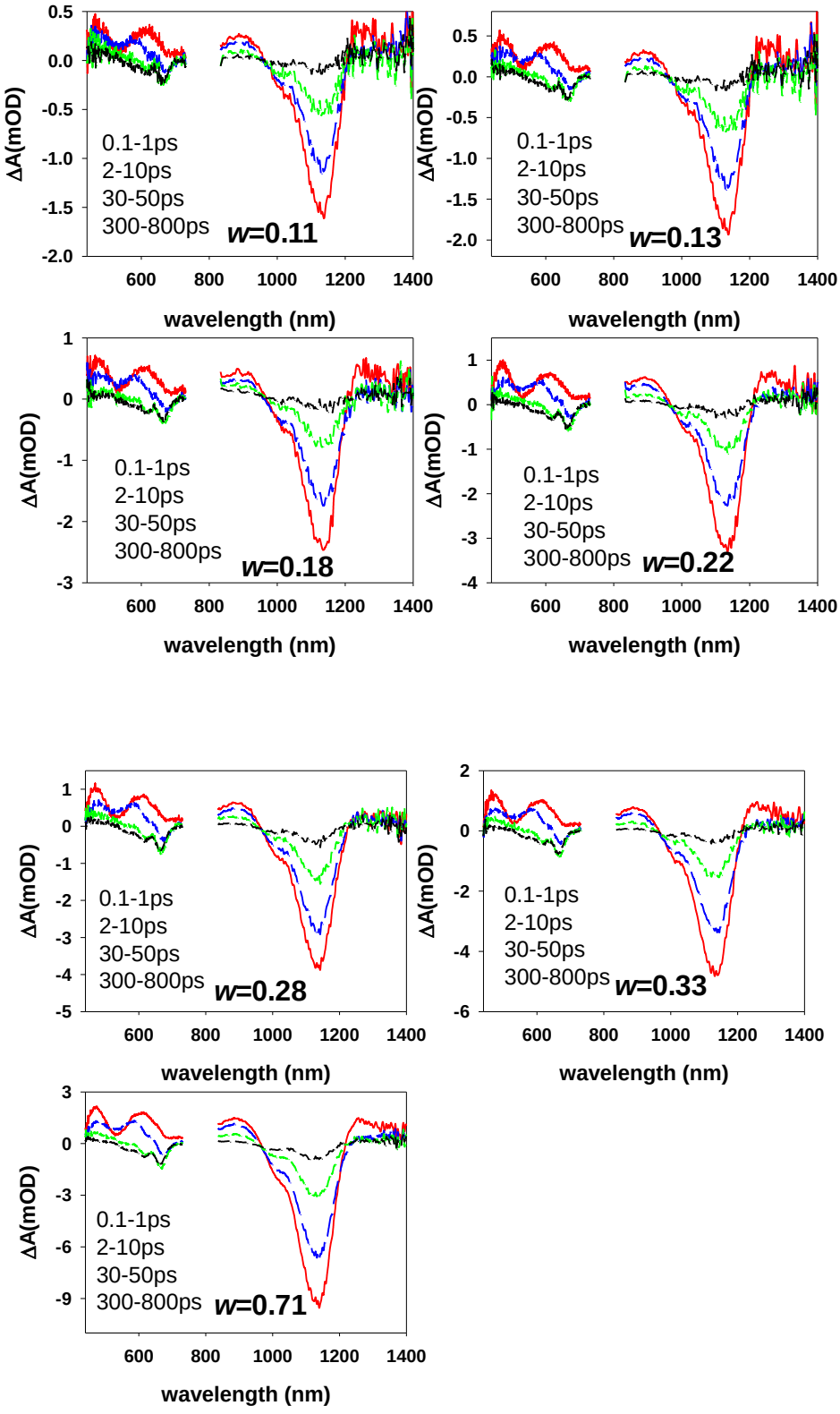
ΔA(mOD)
wavelength (nm)
0.1-1ps
2-10ps
30-50ps
300-800ps
w=0.11
w=0.13
w=0.18
w=0.22
w=0.28
w=0.33
w=0.71

Figure A.4.4. TA spectra of PbS-MB complexes under different intensities of 400 nm pump. The average number of excitons per QD is indicated in each panel.

Chapter 5. Strong Electronic Coupling and Ultrafast Electron Transfer between PbS Quantum Dots and TiO2 Nanocrystalline

5.1. Introduction.

Lead chalcogenide quantum dots (QD) have emerged as a promising class of materials for QD solar cells in recent years[1-4] due to theirs tunable energy gaps, broad spectral responses (from UV to the near IR),[2, 5, 6] and long exciton lifetimes.[7, 8] Furthermore, the possibilities of multiple exciton generation (MEG)[1, 9-12] and hot carrier extraction[13, 14] in these QDs offer exciting opportunities to improve the conversion efficiencies of QD sensitized solar cells by reducing the loss of high energy carriers, despite the modest efficiency of the MEG process reported so far.[14] For example, Zhu and coworkers reported ultrafast hot electron injection from PbSe QDs to rutile (110) TiO_2 single crystal surface,[13] with an estimated injection time of < 50 fs, competitive with the hot electron relaxation ~processes (0.2 – 6 ps[15, 16]) in PbSe QDs. More recently, in model solar cells consisted of PbS QD adsorbed on the anatase (001) TiO_2 single crystal surface, two-fold photocurrent enhancement (and nearly 180% absorbed photon-to-current conversion efficiency) at the near UV region was reported and was attributed to efficient multiple exciton generation and collection in these devices.[1] This report also suggests that the rates of interfacial electron transfer from PbS QDs to TiO_2 anatase single crystals are faster than the rates of exciton-exciton annihilation (10 – 100 ps[17, 18]).

The photocurrent density in the aforementioned TiO_2 single crystal-based model solar cells is rather small due to the low surface area of single crystals, which limits the amount of adsorbed QDs and light harvesting efficiency of the device.[1] The effective surface area (and light harvesting efficiency) can be improved by using nanocrystalline thin films, which have been successfully implemented for dye[19] as well as QD[20, 21] sensitized solar cells. It is important to note that MEG photocurrent enhancement has not been reported in solar cells based on lead salt QD sensitized TiO_2 nanocrystalline thin films.[3] Furthermore, recent studies of PbS and PbSe QDs on colloidal TiO_2 nanoparticles and nanocrystalline thin films have reported the lack of hot electron injection and slow electron transfer rates.[7, 22, 23] Bonn and coworkers concluded a lack of hot electron transfer from PbSe QDs to TiO_2 nanocrystalline thin films by comparing the kinetics measured by transient absorption, fluorescence quenching and Terahertz absorption, as well as photocurrent in devices.[22] Hyun and coworkers have investigated electron transfer dynamics in PbS-linker-TiO_2 nanoparticle complexes in solution by fluorescence quenching.[7, 23] They reported slow electron transfer times of a few to hundreds of nanoseconds in these complexes, which are over five orders of magnitude slower than the reported hot-electron transfer rate of PbSe to rutile TiO_2 single crystals. These large differences of electron transfer times and device performances for QDs on TiO_2 single crystals *vs* nanoparticles and nanocrystalline thin films are not understood.

In this chapter, we examine electron transfer dynamics in PbS QD sensitized TiO_2 nanocrystalline thin films by transient absorption (TA) spectroscopy. TA spectroscopy in the visible or near IR region has been shown to be a powerful tool for studying ET from CdX (X=S, Se, Te) QDs to TiO_2 and other electron acceptors because the 1S exciton bleach in excited CdX QDs is dominated by the state filling of the 1S electron level and provides a convenient probe of the dynamics of the 1S electron.[24-29] However, in PbS QDs, both 1S electrons and holes contribute to overlapping transient absorption features (1S exciton bleach and induced absorption) in the visible and near IR regions that cannot be easily separated.[22, 30] We showed that

by probing both the interband 1S exciton transition in the near IR and the intraband transitions of electrons and holes in the mid-IR, the electron and hole transfer dynamics in PbS QD sensitized TiO_2 nanocrystalline thin films can be unambiguously and independently probed. The assignment of these processes is further confirmed by varying the electronic coupling strength and electron transfer rate through the insertion of Al_2O_3 insulating layers between the QD and TiO_2. On TiO_2 nanocrystalline thin films, the electronic coupling between the QD electron levels and the TiO_2 conduction band (CB) is large, leading to a broadened 1S exciton band in both the static and transient absorption spectra and an instantaneous disappearance of the 1S electron intraband absorption in transient kinetics. Using News-Anderson model of chemisorptions, we estimated a coupling strength of 51±3 meV for the 1S electron level, which corresponds to an adiabatic electron transfer rate of ~ 13±1 fs from the PbS QD 1S level to the TiO_2 conduction band.

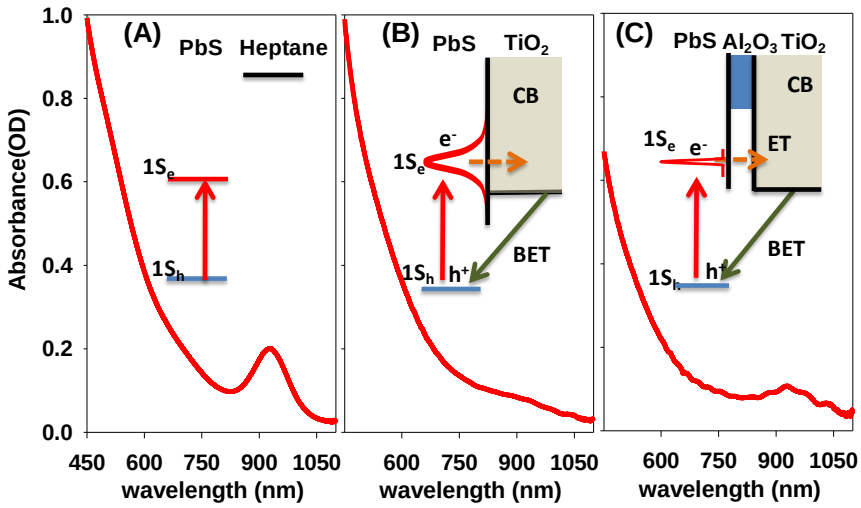

Figure 5.1. Steady state visible-NIR absorption spectra of PbS QDs in heptanes (A), on TiO_2 (B) and on $3Al_2O_3/TiO_2$(C). The absorptions of substrates and solvents have been subtracted from these spectra. Schematic energy level diagrams of the QD and substrate are shown in the insets.

5.2. Results and discussions.

5.2.1. Exciton band broadening in absorption spectra.

PbS QDs were prepared following a literature procedure.[5] The visible-NIR absorption spectrum of the QDs in heptane (Figure 5.1A) shows the first (1S) exciton absorption band at 936 nm. The corresponding QD diameter and energy of the 1S electron level were estimated to be 3.6 nm and -3.7 eV (*vs* vacuum), respectively.[7, 31] The CB edge of the TiO_2 nanocrystalline thin films is pH dependent[32] and was estimated to be -4.2 ± 0.15 eV for films that were exposed to air. [8, 33] Therefore, photo-induced electron injection from PbS QDs to TiO_2 is energetically allowed.

Nanocrystalline TiO_2 films on sapphire windows were prepared according to a reported method.[34] Sapphire windows were used in this study for their transparency in the mid-IR region (3-5 μm). The PbS QDs were attached on TiO_2 thin films by bi-functional linkers, 3-mercaptopropionic acid (MPA), following literature procedures.[20] Briefly, the TiO_2 film was immersed in a 5% (volume) methanol solution of MPA for 6 hours, followed by thorough rinsing with methanol to remove any weakly adsorbed MPAs. This process leads to the chemisorbed MPA molecules bound on the TiO_2 film through the carboxylic acid moiety and with the thiolate groups oriented outward for coupling with the PbS QDs. The functionalized TiO_2 films were then immersed into PbS heptane solutions for ~ 0.5 – 1.0 hours to attach the QDs. Finally, the QD-sensitized films were thoroughly rinsed with excess heptane to remove any weakly adsorbed PbS QDs. As seen in Figure 5.1 B, the PbS sensitized TiO_2 absorption spectrum shows a significant increase of absorption in the spectral range of 450-1100 nm, indicating the presence of PbS QDs. However, the PbS 1S exciton band, which is clearly present for QDs in heptane solution, can no longer be observed.

There are three possible reasons for the observed spectral broadening of exciton bands: increased inhomogeneous distribution of QD sizes, strong QD-QD coupling and strong QD-TiO_2 interaction. The occurrence of both oxidation (decreasing the dots size) and Oswald ripening

(increasing the dots size) can broaden the heterogeneous distribution of QDs size, causing the broadening of the exciton bands.[35-38] However, previous study has shown that smaller PbS QDs (with band gap of ~ 1.3 eV and similar to the ones used in the current experiment) are stable for over six days under ambient conditions, as evidenced by the lack of change in their absorption spectra.[36] Indeed, the visible-NIR absorption spectra of our PbS QDs in solution (result not shown), on sapphire windows and TiO_2 films show negligible change within 2 days. All TA measurements to be discussed below were conducted within 48 hours of sample preparation and the samples were kept in dark (except during measurement) to ensure negligible contribution of sample aging effects. Furthermore, absorption spectra of freshly prepared PbS/TiO_2 samples under nitrogen protection also show a lack of the 1S exciton peak, suggesting that its absence is not caused by oxidation and/or Ostwald ripening.

Exciton peaks can also be broadened in coupled QDs when they are in close contact.[39-42] This is often achieved by removing their surface ligands or cross-linking by short di-thiol molecules.[39, 43, 44] In our experiment, the oleic acid (OA) ligands are still present on the QD surface after their attachment to the TiO_2 films or deposition on the sapphire window surface, which is confirmed by comparing the FTIR spectra of the OA ligands in these samples. In addition, the visible-NIR absorption spectrum of the QDs deposited on sapphire window is nearly the same as the QD solutions, suggesting that the interaction between the OA capped QDs are not strong enough to account for the broadened 1S exciton band of QDs on TiO_2.

Finally, the only remaining possibility for the broadened exciton bands is the strong mixing of the QD and TiO_2 conduction band levels, as illustrated in the inset of Figure 5.1B. The 1S hole level of the QD is located in the band gap of TiO_2, while the 1S and higher electron levels are above the TiO_2 CB edge and in resonant with the CB levels. Because of the strong confinement effect, the electron wave functions can greatly extend beyond the surface of QDs, enabling strong interaction with the CB of TiO_2 and the broadening of the 1S and higher electron levels and their corresponding exciton bands. It should be noted that strong mixing of molecular adsorbate levels

with the TiO_2 CB levels has been reported previously.[45] The observation of hot electron injection also led to an estimate of strong mixing between the PbSe QD 1P level with the CB of TiO_2 rutile (110) single crystal, although the broadening of the exciton bands was not directly observed.[46]

To provide direct supporting evidence of the broadening mechanism of the 1S exciton band, we investigated its dependence on the strength of the QD-TiO_2 coupling. The coupling strength was modulated by inserting Al_2O_3 layers of various thicknesses between the QDs and TiO_2 thin films. Because of the higher CB edge of Al_2O_3, it should act as a tunneling barrier between the QD and TiO_2 CB levels. Therefore, their coupling strength should decrease exponentially with the Al_2O_3 thickness. Two samples, $1Al_2O_3/TiO_2$ and $3Al_2O_3/TiO_2$, with one and three cycles, respectively, of Al_2O_3 deposition and sintering were prepared for the study.[47-49] Although the exact thicknesses of the Al_2O_3 over layers have not been determined and their distributions are likely heterogeneous, the average thicknesses are expected to increase with the number of deposition – sintering cycles. These films were then sensitized by QDs following the same procedure for the TiO_2 films described above. As shown in Figure 5.1C, the absorption spectrum of the $PbS/3Al_2O_3/TiO_2$ film clearly shows the first exciton absorption peak, suggesting that the electronic coupling between the PbS QD 1S exciton and the TiO_2 CB levels is indeed weakened by the Al_2O_3 layer.

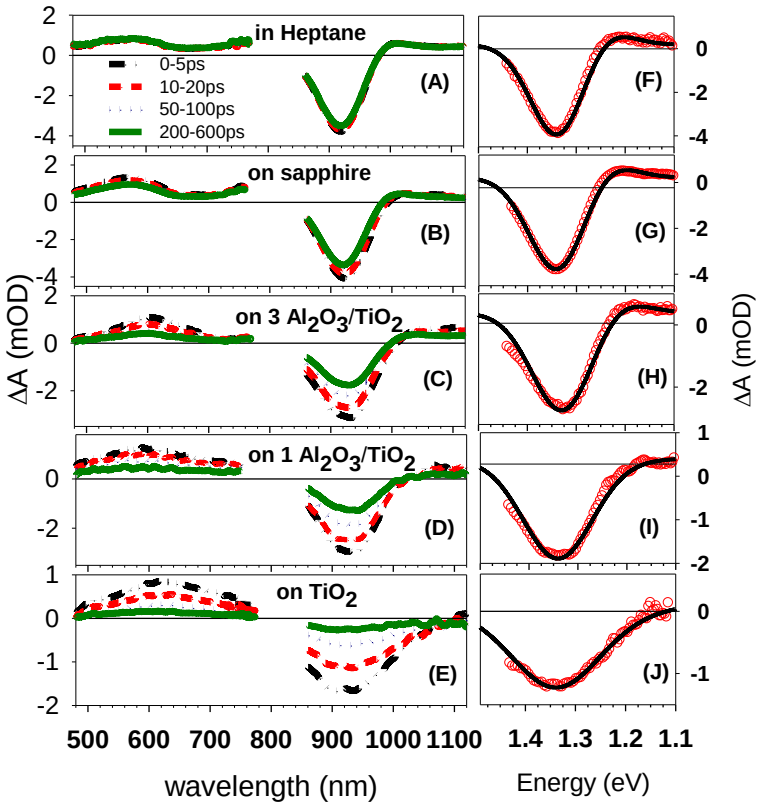

Figure 5.2. (left panels) Averaged visible and near IR TA spectra at indicated delay time windows after 800 nm excitation and (right panels) comparison of simulated (black lines) and measured (red circle) 1S exciton bleach spectra at 10 - 20 ps of PbS QDs in heptanes (A, F), on sapphire window (B, G), on $3Al_2O_3/TiO_2$ (C, H), on $1Al_2O_3/TiO_2$ (D, I), and on TiO_2 (E, J). Data near 800 nm was not shown because of the scattering of the pump beam. The 1S exciton bleach is fit by the News-Anderson model of chemisorptions (see main text for details).

5.2.2. Visible-NIR transient absorption measurements.

The spectral width of the exciton bands and the dynamics of electrons and holes can be directly probed by TA spectroscopy. The experimental setups for the TA measurement in the visible-NIR and mid-IR regions are described in Chapter 2. The visible-NIR TA spectra of isolated PbS QDs in heptane measured after 800 nm excitation are shown in Figure 5.2 A. A clear

bleach of 1S exciton band near 920 nm and an induced absorption feature from 450 to 800 nm are observed. The 1S exciton bleach is attributed to the state filling of 1S electron and hole levels,[30, 50] and the positive feature in the visible region is caused by the red-shift of higher energy bands induced by the presence of the 1S exciton.[51-53] The recovery of these two TA features is less than 10% within 600 ps, indicating that most excited QDs are in the long-lived single exciton state. The TA spectra of QDs deposited on sapphire windows (Figure 5.2 B) show similar TA spectral and dynamic features, suggesting negligible interaction of the 1S electrons and holes between the QDs and with the insulating substrate (sapphire window). However, the TA spectra for PbS on TiO_2 measured under the same excitation conditions (Figure 5.2 E) show a much more broadened 1S exciton bleach and a faster bleach recovery (> 90% within 600 ps). As shown in Figure 5.2 C and 5.2 D, both the width of the 1S exciton bleach and its rate of recovery decrease with the Al_2O_3 insulating layer thickness. It is interesting to note that a clear although broad 1S exciton bleach was observed in the TA spectra, which is much more pronounced than the 1S exciton band in the static absorption spectrum (Figure 5.1 B) of PbS/TiO_2 samples. The reason for this discrepancy will be provided below.

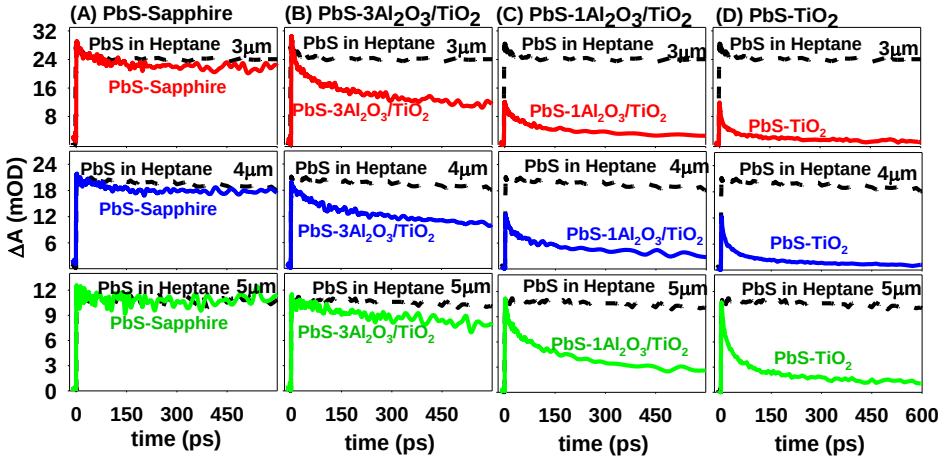

Figure 5.3. Comparisons of mid-IR kinetics of PbS QDs in heptane (black dotted lines) and on sapphire window (A), $3Al_2O_3/TiO_2$(B), $1Al_2O_3/TiO_2$(C), and TiO_2 (D) at 3 (top panels, red lines),

4 (middle panels, blue lines) and 5 (bottom panels, green lines) μm after 800nm excitation. The signals from each substrate have been scaled by a normalization factor such that it has the same initial amplitude at 5 μm as QDs in heptane.

5.2.3. Mid-IR transient absorption measurements.

We have shown previously that the TA features of PbS QDs in the visible and near IR regions contain overlapping contributions of both the electrons and holes, making it difficult to differentiate electron and hole transfer dynamics.[30] However, the 1S electron ($1S_e \rightarrow 1P_e$) and hole ($1S_h \rightarrow 1P_h$) intraband absorptions at the mid-IR region have different peak positions, which enables a direct and independent probe of the electron and hole dynamics. The size of the QDs used in this study is similar to that in Chapter 3 (~8 meV shift in the 1S exciton peak position). Therefore, it is reasonable to assume that they have similar peak positions for the electron and hole intraband absorptions in the mid-IR: the absorption at 5 μm is dominated by the 1S hole and absorption at 3 μm contains both the 1S electron and hole contributions.[30]

The transient IR kinetics of PbS QDs on different substrates are shown in Figure 5.3. For better comparison, the transient signal amplitudes of QDs on each substrate at different probe wavelength (3, 4 and 5 μm) have been scaled by a common factor such that the initial amplitude at 5 μm matches that of QDs in heptane. In the absence any ultrafast hole decay dynamics or broadening of hole levels, this scaling ensures the same initial number of excitons in these samples. The validity of such scaling scheme is confirmed by the TA kinetics of PbS QDs on sapphire window. As shown in Figure 5.3 A, the scaled transient IR kinetics are identical to those of QDs in heptane, consistent with the lack of fast electron and hole decay process within 600 ps in these samples.

As shown in Figure 5.3 C and 5.3 D, unlike QDs in the heptane solution, the scaled kinetics for QDs on TiO_2 and $1Al_2O_3/TiO_2$ show only ~50% and ~25% initial amplitudes at 4 and 3 μm, respectively. Furthermore, kinetics traces at 3 and 4 μm are nearly the same as the hole kinetics at 5 μm and the 1S exciton bleach recovery kinetics at 920 nm, indicating that all measured signals are dominated by the hole dynamics. These kinetics suggest that in both samples, the lifetime of the conduction band electrons are too short (<< 150 fs, the time resolution of this experiment) to be detected in the current measurement. Ultrafast charge separation generates an injected electron in TiO_2 with a hole remaining in the VB of PbS. Their recombination leads to the observed 1S exciton bleach recovery in the near IR and the decay of the 1S hole intraband absorption in the mid-IR.

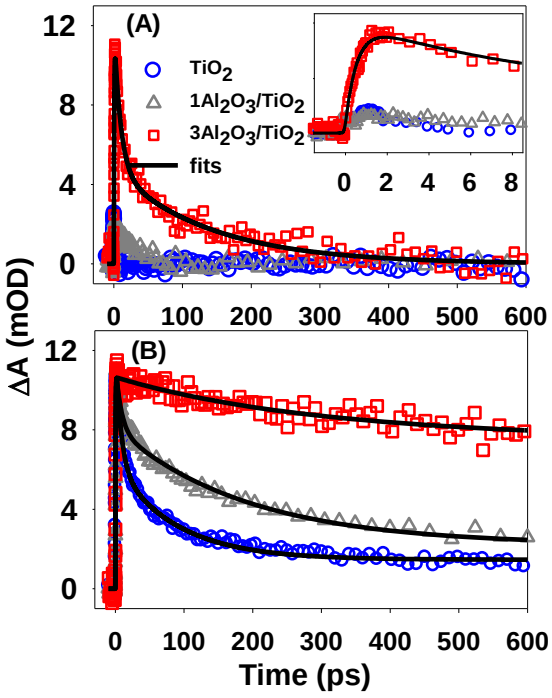

Figure 5.4. Comparison of electron injection (A) and charge recombination (B) kinetics of PbS QDs on TiO_2, $1Al_2O_3/TiO_2$, and $3Al_2O_3/TiO2$. The electron injection kinetics is represented by the kinetics of 1S electron, which is obtained by subtracting the hole contribution from the signal

at 3 μm (see text). The inset in A shows an expanded view of the data at early delay times. The recombination kinetics is monitored by the decay of the 1S hole signal at 5 μm. The black solid lines are multi-exponential fits to these kinetic traces.

For QDs on $3Al_2O_3/TiO_2$ film, the scaled TA kinetics at 3, 4 and 5 μm show the same initial amplitudes as QDs in solution (Figure 5.3 B) but wavelength dependent fast decay components within 600 ps. The kinetics at the different wavelengths shows similar decay trend at the long delay time, but the kinetics at shorter wavelength shows the larger contribution of fast decay component. The kinetics at 5 μm can be attributed to the hole decay, which is a direct measure of the charge recombination process. The kinetics at 3 and 4 μm contains both the 1S electron and hole contributions, but they can be separated because the kinetics of the hole and its contribution to the signal can be independently determined. As shown in Figure 5.3 C and 5.3 D, the initial signal at 3 μm of PbS QDs in heptanes contains ~25% hole contribution. Assuming a similar hole contribution to the kinetics of PbS QDs on $3Al_2O_3/TiO_2$, it can be subtracted to yield the 1S electron-only kinetics shown in Figure 5.4 A. The decay kinetics can be fit by a bi-exponential function with amplitudes and time constants (A_i, τ_i) of (0.61, 10 ps) and (0.39, 141 ps), respectively. From these fitting parameters, an amplitude-weighted average time constant of 61 ps was calculated to represent the average electron transfer time. Electron-only decay kinetics for PbS QDs on TiO_2 and $1Al_2O_3/TiO_2$ can also be obtained by similar subtracting procedure, as shown in Figure 5.4 A. However, these kinetics show only a small instrument response limited spike at t=0, consistent with much faster electron transfer rates in these samples. A comparison of hole kinetics at 5 μm, shown in Figure 5.4 B, shows that the charge recombination rate slows down with increasing Al_2O_3 layer thicknesses. Since all these kinetic traces contain the ultraslow (> 1 ns) components that cannot be accurately examined due to the delay time range, the half-lives, listed in Table 5.1, were used to represent the average charge recombination time.

Table 5.1. Summary of 1S electron level broadening, electron injection time and charge recombination time of PbS QDs on different substrates.

substrates	energy broadening (Δ)	electron injection	recombination
TiO_2	49 meV	13 fs [a]	32 ps
$1Al_2O_3/TiO_2$	17 meV	38 fs [a]	93 ps
$3Al_2O_3/TiO_2$	<1 meV	61 ps [b]	>1ns

[a] calculated from the 1S exciton spectral broadening;

[b] calculated from the 1S electron decay kinetics.

5.2.4. Strong electronic coupling and adiabatic electron transfer.

The electron injection rate from PbS QDs to TiO_2 is too fast to be measured directly with the time resolution in current experiment. However, fast electron transfer processes lead to the broadened 1S exciton band, which is evident in both the steady state absorption (Figure 5.1) and TA (Figure 5.2) spectra. The broadening of a discrete adsorbate electronic level resulted from mixing with a continuum of substrate states can be described by the Newns-Anderson model for chemisorptions.[54, 55] This model was recently used to estimate the electronic coupling strength responsible for the hot electron injection from PbSe QDs absorbed to rutile (110) TiO_2 single crystal surface, although the spectra broadening was not directly observed.[46] Here, we apply this model to fit the 1S exciton bleach in the TA spectrum, which enables the determination of the coupling strength and the electron transfer time.

According to the News-Anderson model for chemisorptions, the mixing of a discrete adsorbate level with continuum states in a solid leads to the broadening of the adsorbate level. The density of states of the broadened absorbate level as a function of energy ε is given by: [55]

$$\rho(\varepsilon, \Delta_{ET}) = \frac{1}{\pi} \frac{\Delta_{ET}}{(\varepsilon - \varepsilon_{1S})^2 + \Delta_{ET}^2} \qquad (5.1)$$

where ε_{1s} is the energy of the 1S electron level prior to the adsorption; Δ_{ET} is the width of the energy broadening, dependent on the electronic coupling strength between the adsorbate and substrate. We have assumed that Δ_{ET} is independent of energy, which is reasonable within a small range of energy. According to the Heisenberg uncertainty principle, the increase of the homogenous spectral line width, $2\Delta_{ET}$, corresponds an decrease of the lifetime, $\tau = \hbar / \Delta_{ET}$, of the electron in this broadened level. This shortened 1S electron lifetime corresponds to the electron transfer time from the 1S electron level to the TiO_2. We have also assumed that the broadening of the 1S hole level, located in the band gap of TiO_2, is negligible, and the broadened 1S electron level is responsible for the observed broadening of 1S exciton bands in the steady state and transient spectra.

For QDs in heptane solution, there is an intrinsic broadening of the 1S exciton band in the absence of any interaction with the substrate. This intrinsic line shape can be well described by a Gaussian function, $G(\varepsilon, \varepsilon_{1S}, \Delta_0)$, with a full width at the half maximum Δ_0 of 141 meV, and peak position ε_{1S} of 1.31 eV. It contains the contribution of a homogenous line-width of the 1S exciton transition and an inhomogeneous distribution of exciton energy, which can result from a distribution of QD sizes and shapes. A Gaussian line shape suggests the dominant contribution of inhomogeneous broadenings. Assuming the same QD-substrate electronic coupling strength for all QDs, the total exciton lineshape, $F(\varepsilon)$, is given by the convolution of the intrinsic heterogeneous distribution, $G(\varepsilon; \varepsilon_{1S}, \Delta_0)$, with the QD-substrate coupling induced broadening, $\rho(\varepsilon; \Delta_{ET})$:

$$F(\varepsilon) = G(\varepsilon; \varepsilon_{1S}, \Delta_0) * \rho(\varepsilon; \Delta_{ET}) \qquad (5.2)$$

The 1S exciton bleach in the transient different spectra result from two main contributions: a decrease in absorbance due to the filling of the 1S electron and hole levels and a red-shift of the exciton band due to exciton-exciton interaction. It can be expressed as equation 3:

$$\Delta F(\varepsilon)=F(\varepsilon+\varepsilon_{XX})-F(\varepsilon)+PA \qquad (5.3)$$

where ε_{XX} is the bi-exciton binding energy in the QD. We have also added a constant, PA, to account for a broad positive absorption feature throughout the near IR region. This feature has been attributed to the presence of hole in the QD, although the exact nature of the transition is not well understood.[8] Similar broad hole absorption features have also been observed in CdSe QDs.[24, 56-58]

The transient spectra of 1S exciton bleach for PbS QDs in heptane and on sapphire window are well fit by this model as shown in Figure 5.2 F and G. In these fits, the QD/substrate induced broadening is set to zero and the intrinsic peak position and width are determined from the absorption spectra. The fits yield a biexciton shift, ε_{XX} ~ -0.006 eV, as the only fitting parameter. The same bi-exciton shift is assumed for all other samples.

For 1S exciton bleach of PbS QDs on semiconductor films, the intrinsic exciton line shape (peak position and width) cannot be accurately determined from the static absorption spectra and they may differ from those for QDs on sapphire window or in heptane due to different dielectric environment. However, from the ~ 61 ps electron transfer time determined directly from transient kinetics of PbS QDs on $3Al_2O_3/TiO_2$, the ET induced broadening can be estimated to be << 1 meV. Therefore, we set Δ_{ET} = 0 in this sample, and the transient 1S exciton bleach feature is determined by the intrinsic line-shape of the QD exciton band. The 1S exciton bleach can be well fit by this model with an intrinsic Gaussian peak position ε_{1S} of 1.30 eV and width Δ_0 of 158 meV, as shown in Figure 5.2 H. This Gaussian line shape also describes well the absorption spectrum, although the spectrum contains considerable noise due to interference of the TiO_2 films. The same Δ_0 and ε_{1S} are assumed in the simulations of other TiO_2 samples. The 1S exciton bleach spectra of $PbS/1Al_2O_3/TiO_2$ and PbS/TiO2 can then be fit by eq 5.3, yielding Δ_{ET} = 21±12

and 51±3 meV, respectively. The error bars for the broadenings were determined from measurements of 3 different samples. The larger uncertainty of the measured broadening for PbS on $1Al_2O_3/TiO_2$ is attributed to the poor control of the homogeneity and thicknesses of the Al_2O_3 overlayer in different samples.[47, 59] According to the uncertainty principle, the electron transfer time can thus be calculated to be ~38±18 fs for $PbS/1Al_2O_3/TiO_2$ and ~13±1 fs for PbS/TiO_2. These results are also consistent with the <<150 fs injection time estimated from the direct time resolved measurement of the 1S electron intraband absorption in the mid-IR (Figure 5.4 A).

In the fitting model described above, we have assumed the same QD-adsorbate coupling strength for all QDs. There likely exists a distribution of interaction strengths due to the presence of different adsorption sites. Unfortunately, the extent of this distribution cannot be independently determined from the current data. The coupling strength and ET rate reported here should be considered as average values. It is important to point out that the observed broadening of the 1S exciton band cannot be attributed to an increase in the QD size distribution caused by oxidation or Ostwald ripening.[35-38] In addition to the reasons discussed above, these mechanisms would affect both the electron and hole intraband transitions equally and would not lead to shortened 1S electron lifetimes, which were clearly observed for PbS QDs on TiO_2 and $1Al_2O_3/TiO_2$.

The comparison of absorption spectra of QDs in heptane and on TiO_2 indicates the broadening of higher energy exciton bands. The extents of broadening of these bands are not determined in the current study. The broadening of the QD electron levels depends on the QD-substrate coupling strength and the density of TiO_2 CB band states.[49,50] The latter should increase with energy above the CB band edge. The coupling strength should also increases for higher QD electron levels due to increased extension of wave functions outside the QD surface. This is a consequence of a finite confinement potential of the electron,[60, 61] and can be understood also from the energy dependent effective tunneling barrier height. Both the energy dependent density of states and coupling strength suggest larger broadenings of higher electron levels in the QD and faster electron transfer rates. The study of the electron transfer from these higher energy states is

going to be discussed in the next chapter. The absorption spectrum is a sum of all transitions to these overlapping and broadened electron levels, which completely smear out the exciton features for QDs on TiO_2. However, the transient bleach only results from electron and hole levels that are occupied, i.e. the 1S electron and hole levels in this experiment. Therefore, only the 1S exciton band bleach is observed, free from the overlapping and broadened higher energy transitions. Effectively, optical excitation burns out a 1S exciton feature in the broad visible-NIR absorption spectrum of QDs on TiO_2, which enables the observation of the 1S exciton band in the TA spectra even when this feature is obscured in the steady state absorption spectra.

The observed ~ 13 fs electron transfer from the 1S electron level of PbS QDs to TiO_2 nanocrystalline thin films is consistent with a recent report of hot electron injection from PbSe to rutile (110) TiO_2 surface, in which the injection time from the 1P electron level was estimated to be < 50 fs.[13, 46] Although the injection rate from the 1P level was not determined in this study, it is likely to be faster based on the discussion above. Our result is not consistent with recent reports of the lack of hot-electron injection from PbSe QDs to nanocrystalline thin films,[22] and slow electron transfer (a few to hundreds of nanoseconds) in PbS-linker-TiO_2 nanoparticle complexes in solution.[7, 23] The reasons for these differences are not clear and will be addressed in future studies.

The strong coupling between the QD and TiO_2 suggests that electron transfer proceeds adiabatically. Such ET processes are barrier less if $\Delta > 2\lambda/\pi$, where λ is the total reorganization energy.[62, 63] Because of the lack of solvent in the current system, λ is determined by the QD and TiO_2. The reorganization energies of both particles are expected to be small because of delocalized electrons and small electron-phonon coupling in these materials. A reorganization energy of ~10 meV for ET from QDs has been estimated from an experimental study of the driving force dependence of ET rates.[64, 65] Assuming similar reorganization energy in the current system, photoinduced ET from PbS QDs on TiO_2 would be barrier less. This leads to a following microscopic picture of this ET process: the optical excitation generates a wave-packet with the

electron localized on the QD, which undergoes ultrafast and barrier less propagation into the TiO_2 conduction band due to the strong mixing of QD and TiO_2 electron levels. Similar notions have been suggested previously for related interfacial ET processes between molecules and semiconductor electrodes.[66-69]

5.3 Conclusion.

In summary, electron transfer dynamics from PbS QDs to TiO_2 nanocrystalline films were studied by transient absorption spectroscopy. In addition to the 1S exciton band in the near IR, the electron and hole dynamics were independently probed by their intraband transitions in the mid-IR to directly follow the electron transfer and charge recombination processes, respectively. The effects of QD-substrate and QD-QD interactions were investigated by comparing QDs on TiO_2 with QDs in heptanes solutions, on insulating sapphire window substrates, and on TiO_2 coated with varying thickness of Al_2O_3 insulating layers. This comparison shows that the strong QD-TiO_2 interaction leads to the broadening of the 1S exciton band in the static and transient absorption spectra as well as << 150 fs injection time from the QD to TiO_2. The broadening of the 1S exciton band can be well fit by the News-Anderson model of chemisorption, yielding a coupling strength between the QD 1S electron level and the TiO_2 CB of ~51±3 meV and a corresponding electron transfer time ~13±1 fs. The injected electrons in TiO_2 recombine with the 1S holes in the PbS QDs with a half-life of 32 ps. Both the electron injection and charge recombination times were shown to decrease with increasing thickness of Al_2O_3 overlayers on TiO_2. Our findings suggest the possibility of extracting hot carriers and multiple excitons in solar cells based on PbS QD sensitized TiO_2 nanocrystalline thin films, similar to recent demonstrations of such processes of related QDs on bulk TiO_2 single crystals. [1, 13]

References

1. Sambur, J. B.; Novet, T.; Parkinson, B. A. *Science* **2010,** 330, (6000), 63-66.

2. Sargent, E. H. *Nat Photon* **2009,** 3, (6), 325-331.

3. Pattantyus-Abraham, A. G.; Kramer, I. J.; Barkhouse, A. R.; Wang, X. H.; Konstantatos, G.; Debnath, R.; Levina, L.; Raabe, I.; Nazeeruddin, M. K.; Gratzel, M.; Sargent, E. H. *ACS Nano* **2010,** 4, (6), 3374-3380.

4. Luther, J. M.; Law, M.; Beard, M. C.; Song, Q.; Reese, M. O.; Ellingson, R. J.; Nozik, A. J. *Nano Lett.* **2008,** 8, (10), 3488-3492.

5. Hines, M. A.; Scholes, G. D. *Adv. Mater.* **2003,** 15, (21), 1844-1849.

6. Murray, C. B.; Sun, S.; Gaschler, W.; Doyle, H.; Betley, T. A.; Kagan, C. R. *IBM J. Res. & Dev.* **2001,** 45, (1), 47-56.

7. Hyun, B. R.; Zhong, Y. W.; Bartnik, A. C.; Sun, L. F.; Abruna, H. D.; Wise, F. W.; Goodreau, J. D.; Matthews, J. R.; Leslie, T. M.; Borrelli, N. F. *ACS Nano* **2008,** 2, (11), 2206-2212.

8. Leventis, H. C.; O'Mahony, F.; Akhtar, J.; Afzaal, M.; O'Brien, P.; Haque, S. A. *J. Am. Chem. Soc.* **2010,** 132, (8), 2743-2750.

9. Pijpers, J. J. H.; Ulbricht, R.; Tielrooij, K. J.; Osherov, A.; Golan, Y.; Delerue, C.; Allan, G.; Bonn, M. *Nat. Phys.* **2009,** 5, (11), 811-814.

10. McGuire, J. A.; Sykora, M.; Joo, J.; Pietryga, J. M.; Klimov, V. I. *Nano Lett.* **2010,** 10, (6), 2049-2057.

11. Beard, M. C.; Midgett, A. G.; Hanna, M. C.; Luther, J. M.; Hughes, B. K.; Nozik, A. J. *Nano Lett.* **2010,** 10, (8), 3019-3027.

12. Nair, G.; Geyer, S. M.; Chang, L.-Y.; Bawendi, M. G. *Phys. Rev. B* **2008,** 78, (12), 125325.

13. Tisdale, W. A.; Williams, K. J.; Timp, B. A.; Norris, D. J.; Aydil, E. S.; Zhu, X. Y. *Science* **2010,** 328, (5985), 1543-1547.

14. Nozik, A. J. *Physica E: Low-dimensional Systems and Nanostructures* **2002,** 14, (1-2), 115-120.

15. Schaller, R. D.; Pietryga, J. M.; Goupalov, S. V.; Petruska, M. A.; Ivanov, S. A.; Klimov, V. I. *Phys. Rev. Lett.* **2005,** 95, (19), 196401.

16. Harbold, J. M.; Du, H.; Krauss, T. D.; Cho, K.-S.; Murray, C. B.; Wise, F. W. *Phys. Rev. B* **2005,** 72, (19), 195312.

17. Schaller, R. D.; Sykora, M.; Pietryga, J. M.; Klimov, V. I. *Nano Lett.* **2006,** 6, (3), 424-429.

18. Klimov, V. I.; McGuire, J. A.; Schaller, R. D.; Rupasov, V. I. *Phys. Rev. B* **2008,** 77, (19), -.

19. O'Regan, B.; Gratzel, M. *Nature* **1991,** 353, (6346), 737-740.

20. Robel, I.; Subramanian, V.; Kuno, M.; Kamat, P. V. *J. Am. Chem. Soc.* **2006,** 128, (7), 2385-2393.

21. Plass, R.; Pelet, S.; Krueger, J.; Gratzel, M.; Bach, U. *J. Phys. Chem. B* **2002,** 106, (31), 7578-7580.

22. Pijpers, J. J. H.; Koole, R.; Evers, W. H.; Houtepen, A. J.; Boehme, S.; Donega, C. D.; Vanmaekelbergh, D.; Bonn, M. *J. Phys. Chem. C* **2010,** 114, (44), 18866-18873.

23. Hyun, B.-R.; Bartnik, A. C.; Sun, L.; Hanrath, T.; Wise, F. W. *Nano Lett.* **2011,** 11, (5), 2126-2132.

24. Burda, C.; Link, S.; Mohamed, M.; El-Sayed, M. *J. Phys. Chem. B* **2001,** 105, (49), 12286-12292.

25. Klimov, V. I. *Annu. Rev. Phys. Chem.* **2007,** 58, 635-673.

26. Robel, I.; Kuno, M.; Kamat, P. V. *J. Am. Chem. Soc.* **2007,** 129, (14), 4136-+.

27. Zhu, H.; Song, N.; Lian, T. *J. Am. Chem. Soc.* **2010,** 132, (42), 15038-15045.

28. Huang, J.; Stockwell, D.; Huang, Z.; Mohler, D. L.; Lian, T. *J. Am. Chem. Soc.* **2008,** 130, (17), 5632-5633.

29. Huang, J.; Huang, Z. Q.; Yang, Y.; Zhu, H. M.; Lian, T. Q. *J. Am. Chem. Soc.* **2010,** 132, (13), 4858-4864.

30. Yang, Y.; Rodríguez-Córdoba, W.; Lian, T. *J. Am. Chem. Soc.* **2011,** 133, (24), 9246-9249.

31. Kang, I.; Wise, F. W. *J. Opt. Soc. Am. B* **1997,** 14, (7), 1632-1646.

32. Rothenberger, G.; Fitzmaurice, D.; Graetzel, M. *J. Phys. Chem.* **1992,** 96, (14), 5983-5986.

33. Asbury, J. B.; Hao, E.; Wang, Y.; Lian, T. *J. Phys. Chem. B* **2000,** 104, (50), 11957-11964.

34. Zaban, A.; Ferrere, S.; Sprague, J.; Gregg, B. A. *J. Phys. Chem. B* **1997,** 101, (1), 55-57.

35. Ihly, R.; Tolentino, J.; Liu, Y.; Gibbs, M.; Law, M. *ACS Nano* **2011**, ASAP.

36. Tang, J.; Brzozowski, L.; Barkhouse, D. A. R.; Wang, X.; Debnath, R.; Wolowiec, R.; Palmiano, E.; Levina, L.; Pattantyus-Abraham, A. G.; Jamakosmanovic, D.; Sargent, E. H. *ACS Nano* **2010,** 4, (2), 869-878.

37. Law, M.; Luther, J. M.; Song, Q.; Hughes, B. K.; Perkins, C. L.; Nozik, A. J. *J. Am. Chem. Soc.* **2008,** 130, (18), 5974-5985.

38. Schapotschnikow, P.; van Huis, M. A.; Zandbergen, H. W.; Vanmaekelbergh, D. l.; Vlugt, T. J. H. *Nano Lett.* **2010,** 10, (10), 3966-3971.

39. Liljeroth, P.; Overgaag, K.; Urbieta, A.; Grandidier, B.; Hickey, S. G.; Vanmaekelbergh, D.; euml. *Phys. Rev. Lett.* **2006,** 97, (9), 096803.

40. Talgorn, E.; Gao, Y.; Aerts, M.; Kunneman, L. T.; Schins, J. M.; Savenije, T. J.; van HuisMarijn, A.; van der ZantHerre, S. J.; Houtepen, A. J.; SiebbelesLaurens, D. A. *Nat Nano* **2011,** ASAP.

41. Döllefeld, H.; Weller, H.; Eychmüller, A. *Nano Lett.* **2001,** 1, (5), 267-269.

42. Artemyev, M. V.; Woggon, U.; Jaschinski, H.; Gurinovich, L. I.; Gaponenko, S. V. *J. Phys. Chem. B* **2000,** 104, (49), 11617-11621.

43. Williams, K. J.; Tisdale, W. A.; Leschkies, K. S.; Haugstad, G.; Norris, D. J.; Aydil, E. S.; Zhu, X. Y. *ACS Nano* **2009,** 3, (6), 1532-1538.

44. Choi, J. J.; Luria, J.; Hyun, B. R.; Bartnik, A. C.; Sun, L. F.; Lim, Y. F.; Marohn, J. A.; Wise, F. W.; Hanrath, T. *Nano Lett.* **2010,** 10, (5), 1805-1811.

45. Schnadt, J.; Bruhwiler, P. A.; Patthey, L.; O'Shea, J. N.; Sodergren, S.; Odelius, M.; Ahuja, R.; Karis, O.; Bassler, M.; Persson, P.; Siegbahn, H.; Lunell, S.; Martensson, N. *Nature* **2002,** 418, (6898), 620-623.

46. Tisdale, W. A.; Zhu, X. Y. *Proc. Natl. Acad. Sci. U. S. A.* **2011,** 108, (3), 965-970.

47. Guo, J.; She, C.; Lian, T. *J. Phys. Chem. C* **2007,** 111, (25), 8979-8987.

48. Palomares, E.; Clifford, J. N.; Haque, S. A.; Lutz, T.; Durrant, J. R. *J. Am. Chem. Soc.* **2002,** 125, (2), 475-482.

49. Palomares, E.; Clifford, J. N.; Haque, S. A.; Lutz, T.; Durrant, J. R. *Chem. Commun.* **2002**, (14), 1464-1465.

50. Wehrenberg, B. L.; Guyot-Sionnest, P. *J. Am. Chem. Soc.* **2003,** 125, (26), 7806-7807.

51. Kohn, S. E.; Yu, P. Y.; Petroff, Y.; Shen, Y. R.; Tsang, Y.; Cohen, M. L. *Phys. Rev. B* **1973,** 8, (4), 1477-1488.

52. Kanazawa, H.; Adachi, S. *J. Appl. Phys.* **1998,** 83, (11), 5997-6001.

53. Cho, B.; Peters, W. K.; Hill, R. J.; Courtney, T. L.; Jonas, D. M. *Nano Lett.* **2010,** 10, (7), 2498-2505.

54. Anderson, P. W. *Phys. Rev.* **1961,** 124, (1), 41.

55. Newns, D. M. *Phys. Rev.* **1969,** 178, (3), 1123.

56. Klimov, V. I.; Mikhailovsky, A. A.; McBranch, D. W.; Leatherdale, C. A.; Bawendi, M. G. *Phys. Rev. B* **2000,** 61, (20), R13349.

57. Klimov, V. I. *J. Phys. Chem. B* **2000,** 104, (26), 6112-6123.

58. Huang, J.; Huang, Z.; Jin, S.; Lian, T. *J. Phys. Chem. C* **2008,** 112, (49), 19734-19738.

59. Alarcón, H.; Boschloo, G.; Mendoza, P.; Solis, J. L.; Hagfeldt, A. *J. Phys. Chem. B* **2005,** 109, (39), 18483-18490.

60. Brus, L. *J. Chem. Phys.* **1984,** 80, (9), 4403.

61. Brus, L. E. *J. Chem. Phys.* **1983,** 79, (11), 5566-5571.

62. Schmickler, W. *J. Electroanal. Chem.* **1986,** 204, (1-2), 31-43.

63. Smith, B. *J. Chem. Phys.* **1993,** 99, (9), 6517.

64. Tvrdy, K.; Frantsuzov, P. A.; Kamat, P. V. *Proc. Natl. Acad. Sci. U. S. A.* **2011,** 108, (1), 29-34.

65. Hyun, B.-R.; Bartnik, A. C.; Lee, J.-K.; Imoto, H.; Sun, L.; Choi, J. J.; Chujo, Y.; Hanrath, T.; Ober, C. K.; Wise, F. W. *Nano Lett.* **2009,** 10, (1), 318-323.

66. Lanzafame, J. M.; Palese, S.; Wang, D.; Miller, R. J. D.; Muenter, A. A. *J. Phys. Chem.* **1994,** 98, (43), 11020-11033.

67. Gundlach, L.; Ernstorfer, R.; Willig, F. *Prog. Surf. Sci.* **2007,** 82, (4-6), 355-377.

68. Prezhdo, O. V.; Duncan, W. R.; Prezhdo, V. V. *Acc. Chem. Res.* **2008,** 41, (2), 339-348.

69. Zhu, X. Y. *Surf. Sci. Rep.* **2004,** 56, (1-2), 1-83.

Chapter 6. Efficient Room Temperature Hot Electron Transfer from PbS QDs to Nanocrystalline Oxide Films

6.1.Introduction.

In recent years, quantum dots (QDs) have been intensively investigated as light harvesting materials for solar energy conversion due to their many unique properties. It has been well known and extensively investigated that strong quantum confinement in these materials leads to size dependent tunable optical and electronic properties.[1-4] More recent studies reveal that strong confinement, which leads to large amplitudes of electrons and holes outside the QD surface, also increases electron coupling strengths for interfacial electron and/or hole transfer to their respective acceptors, leading to ultrafast exciton dissociation rates.[5-16]. Because the wave functions of electron and holes in quantum confined heterostructures can be readily tuned by the dimension and composition of materials (i.e. wave function engineering), these materials also offer additional controls of single and multiple exciton lifetimes as well as charge separation and recombination rates.[17-20]. Strongly quantum confinement was also thought to enhance multiple exciton generation by one absorbed photons in quantum dots, although this notion is still a subject of intense debate and the reported efficiencies in QDs are still quite modest in the visible to near UV spectral region.[21-27] Hot electrons and holes in solar cells composed of bulk semiconductors can typically relax on the subpicosecond time scale to conduction and valence band edges, respectively, before their extraction to external circuit, thus reducing the overall solar-to-electrical power conversion efficiency. It has been long expected that the discrete energy levels in QDs increase the lifetime of hot carriers due to the presence of "phonon bottle neck",[28] which may allow their extraction prior to their relaxation in quantum dot based solar cells.[29, 30]

Extensive research on hot carrier lifetimes in quantum dots has reported short carrier relaxation lifetimes (picosecond to subpicosecond) in quantum dots due to the presence of

multiple relaxation pathways, such as Auger assisted recombination, multiphonon emission, and energy transfer to ligand vibration.[31-39] In principle, hot carrier extraction can be achieved through the reduction of hot carrier relaxation rate and/or enhancement of interfacial transfer rates. For examples, Pandey and co-workers slowed that by reducing the electron and hole overlap in type II core/multishell structures, hot carrier lifetime as long as 1 ns can be achieved,[28] and the increased lifetime of hot electrons in similar structures enable the hot electron trapping by the surface states (before their relaxation to the band edge).[40] The ultrafast interfacial ET rate in strongly quantum confined QDs also suggests the possibility of hot carrier transfer even with limited hot carrier lifetime. Indeed, hot electron transfer (with a lifetime of < 50 fs) from PbSe QDs to rutile TiO_2 crystals at low temperature (<200 K) has been reported.[9] Interestingly and unfortunately, this study shows that the hot-carrier transfer efficiency decreases rapidly at higher temperature and becomes negligible at room temperature. Additionally, instead of single crystals, practical QD-sensitized solar cells require the use of high surface area nanoporous TiO_2 thin films to achieve sufficient light harvesting. Thus, it is important to study the extraction of hot carriers for QDs on nanoporous TiO_2 surface at room temperatures.

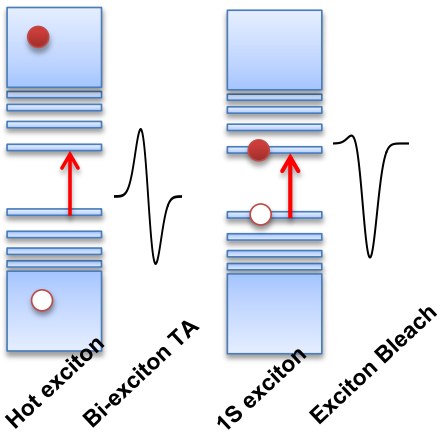

Figure 6.1 Schematic of the biexciton absorption (left) and 1S exciton bleach (right) shown in TA spectra. The biexciton absorption arises from the red-shift of 1S absorption in presence of hot electron. The 1S bleach is attributed to the state filling of both 1S electron and hole state.

In this chapter, we report hot electron transfer from PbS QDs to nanoporous TiO_2 thin films at room temperature. We have chosen this system because of previous report of ultrafast (~6.4 fs) electron transfer from PbS QD to TiO_2 nanocrystalline thin films as well as relatively high power conversion efficiency in solar cells composed of PbS/TiO_2.[10, 41] By transient absorption (TA) spectroscopy, we monitored directly the dynamics of hot and relaxed electrons in these QDs through their distinct TA features.[28, 37] As shown in Figure 6.1, the hot exciton reduces the 1S exciton transition energy and leads to a derivative feature of the 1S absorption band in the TA difference spectra, while the 1S exciton results in a state-filling induced bleach signal at the 1S exciton absorption region. By comparing the amplitudes of spectral features of hot and bandedge electrons, we determined that the hot electron injection yield (ratio of injected electron to total electron) to be 18±4 % in PbS /Al_2O_3/TiO_2 system with 0.39 nm thick Al_2O_3 layer at 2.12 eV pulse excitation.

6.2. Results and discussions.

6.2.1. Hot exciton induced TA in free PbS QDs.

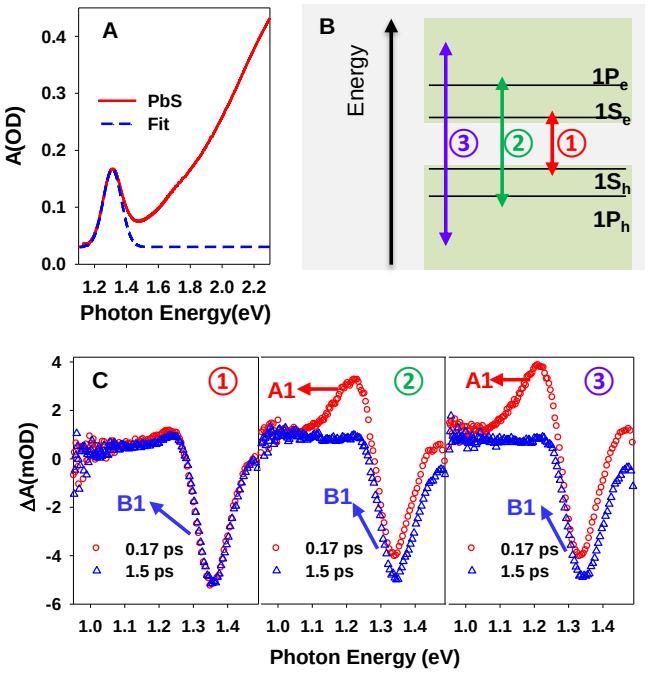

Figure 6.2. Transient spectra at different excitation energy. (A) Visible-NIR absorption spectrum of PbS QDs in a heptane solution (red solid line) and a fit by a Gaussian function (blue dashed line). (B) Energy levels in the QDs (black lines) and the three excitations energies used in the study: 1.39 (red), 2.12 (green), and 3.10 eV (blue). (C) TA spectra of the PbS QDs in heptane at indicated delay times after excitation at the three pump wavelengths shown in panel B.

The synthesis of PbS QDs for this study is described in Chapter 2. As displayed in Figure 6.2 A, the absorption spectrum of the QDs in a heptane solution shows a prominent 1S exciton absorption band that can be fit by a Gaussian function. The center of the 1S exciton band is 1.31 eV, from which the diameter and 1P transition energy is estimated to be 3.7 nm and 2.06 eV, respectively, according to the theoretical model reported by Wise and co-workers.[42] As indicated in Figure 6.2 B, we excited the QDs at 1.39, 2.12 and 3.10 eV to directly generate the 1S, 1P and higher energy excitons, respectively. The TA spectra of the QDs excited by the indicated pump energy are shown in Figure 6.2 C. The pump intensities were adjusted to generate the same amount of the 1S exciton bleach signals at 1.5 ps delay time for different excitation wavelengths.

For the 1.39 eV excitation, the 1S exciton bleach, indicated as B1, caused by populating the 1S exciton state was completely formed within 0.17 ps. However, at the other two excitation wavelengthes, a prominent absorption feature at ~1.2 eV, denoted as A1, was observed in addition to the 1S exciton bleach, and this feature decays quickly to a broad absorption by 1.5 ps, accompanied by the formation of the 1S exciton bleach. These pump energy dependent TA spectra suggest that A1 feature is related to the hot exictons (those with energy higher than 1S exciton). Similar TA feature have also been reported in other types of QDs, such as PbSe,[25] PbS,[43] CdSe[35, 37] and CdSe/ZnSe core-shell QDs,[28] and attributed to the reduction of the 1S exciton transition in the presence of hot excitons (i.e. the bi-exciton interaction energy). The biexicton interaction energy is significantly reduced for the 1S-1S exciton pair, which is responsible for the formation of the broad red-shifted positive TA feature (a less pronounced A1 feature) in in later delay times of Figure 6.2 C.[10]

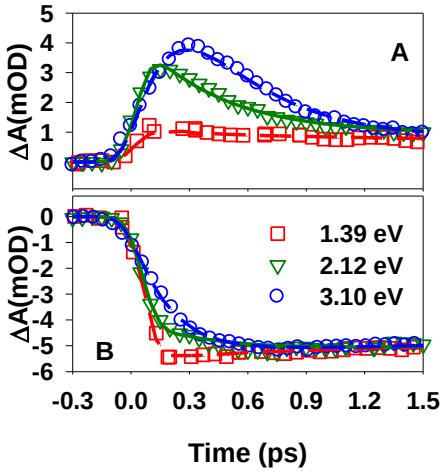

Figure 6.3. (A) The comparison of the A1 kinetics and (B) B1 kinetics of the PbS QD solution excited by the indicated pumps. Also plotted are the exponential fits (lines).

The kinetics of A1 and B1 features of the PbS QD excited at 1.39, 2.12, and 3.10 eV are compared in Figure 6.3 A and B, respectively. The comparison clearly shows that the initial formation and decay kinetics of A1 and B1 features are dependent on the excitation energy; and the kinetics for excitation to higher exciton states become the same as that for direct 1S excition after ~1ps, indicating that the same amount of the 1S excitons eventually formed and the spectral features are dominated by the 1S excitons after ~1ps, indicating the complete formation of the 1S state after this delay time. Also shown in Figure 6.3, the initial formation and decay kinetics can be well fit by exponential functions. For 1.39 eV pump, the instantaneous formation of 1S exciton induced absorption and B1 kinetics is observed, indicating a lack of hot carrier relaxation process, which is consistent with the direction excitation into the 1S exciton state. For the 2.12 eV pump, the A1 feature was formed instantaneously and its decay rate was 2.3±0.4 ps^{-1}. The B1 growth kinetics contains an instantaneous rise, and a component with a growth rate of 2.3±0.5 ps^{-1} that is the same as the decay of A1 feature. Since 1P exciton was directly created at this excitation wavelength, the instantaneous growth for both A1 and B1 features can be attributed to the 1P exciton induced redshift of 1S exciton band, forming an induced absorption feature (A1) and a bleach of 1S exciton band (B1). The decay of A1 and the slow growth component of B1 can be both attributed to the decay of 1P exciton to the 1S level. At 3.10 eV excitation, the formation rates of A1 and B1 are 5.8±0.8 and 5.3±0.8 ps^{-1}, respectively, which is slower than those at lower energy excitation. The A1 feature decays with a rate constant of 2.6±0.4 ps^{-1}, similar to the relaxation of the 1P electron discussed above, indicating that A1 feature is dominated by 1P exciton and the 1P exciton decay is the rate limiting step in the hot electron relaxation process. Since many energy levels exist between the initially generated excitons and the 1P exciton, the growth of the A1 and B1 features can be attributed to the cascade of the hot exciton relaxation process to the 1P level.[24, 44] Thus, we can establish that the A1 feature can be used to probe the 1P exciton or higher energy excitons, and B1 feature after ~1ps reflects the population of the 1S excitons.

6.2.2. 1S electron injection in PbS QDs/ Al_2O_3/TiO_2.

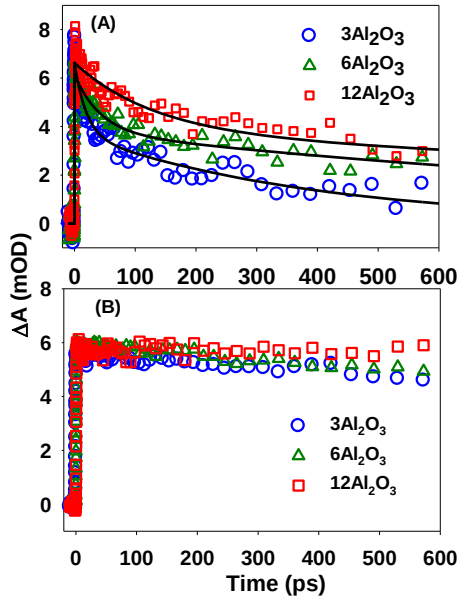

Figure 6.4. Comparisons of (A) 1S electron and (B) 1S hole intraband transition kinetics for PbS QDs on TiO_2 films with different Al_2O_3 coating thicknesses. These kinetics were normalized at early delay time for better comparison. All three samples were excited at 1.55 eV.

In the previous chapter, we have demonstrated that the 1S electron injection from PbS QDs could compete with the hot electron relaxation due to the strong electronic coupling. However, the estimated electron transfer time (~ 6.1 fs) is much faster than our instrument response, preventing the direct probe of 1P exciton dynamics. We also showed that the rate of 1S electron injection can be retarded by inserting Al_2O_3 layers between TiO_2 and PbS QD. With appropriate choice of insulating layer thickness, it is possible to directly resolve the transfer of hot electrons from the 1P and higher levels. In this study, we have chosen atomic layer deposition (ALD) technique to coat the Al_2O_3 layers on TiO_2 film, which is known to achieve better thickness

control compared to the chemical bath deposition method that was used in the previous study. The average thickness of Al_2O_3 layer is known to increase by 0.13 nm per ALD cycle. In this chapter, we denote the TiO_2 films coated with Al_2O_3 by the ALD cycle. For example, $3Al_2O_3$ stands for the TiO_2 film coated by Al_2O_3 with 3 ALD cycles. Figure 6.4 shows the comparison of 1S electron injection and recombination kinetics in QD/Al_2O_3/TiO_2 films with indicated Al_2O_3 ALD cycles. These kinetics were obtained by probing the electron and hole intraband transitions in the mid-IR region as discussed in Chapter 3 and 5. The 1S electron injection kinetics were fit by bi-exponential functions and the fitting parameters are listed in Table 6.1. The rates of electron injection and recombination decrease with increase of Al_2O_3 layer thickness. In films with 3 or more layer of Al_2O_3, the time constant for electron transfer from the 1S level should be much slower than the hot electron injection that is expected to be comparable with the hot electron relaxation (< 1 ps^{-1}), we can thus distinguish the hot electron injection and 1S electron injection when inserting 3 or more than 3 layers of Al_2O_3 (Al_2O_3 thickness ≥ 0.39 nm).

Table 6.1. List of the fitting parameters for 1S electron injection kinetics. The bi-exponential function is expressed as: $A(t) = A_0(A_1 e^{-\frac{t}{\tau_1}} + A_1 e^{-\frac{t}{\tau_1}})$.

	A_0(mOD)	A_1 (100%)	τ_1 (ps)	A_2 (100%)	τ_2 (ns)
$3Al_2O_3$	6.6	44	19.0±3.5	56	0.40±0.12
$6Al_2O_3$		38	42.3±14.3	62	1.31±0.87
$12Al_2O_3$		39	104.8±41.2	60	3.76±4.50

6.2.3. 1P electron injection in PbS QDs/ Al_2O_3/TiO_2.

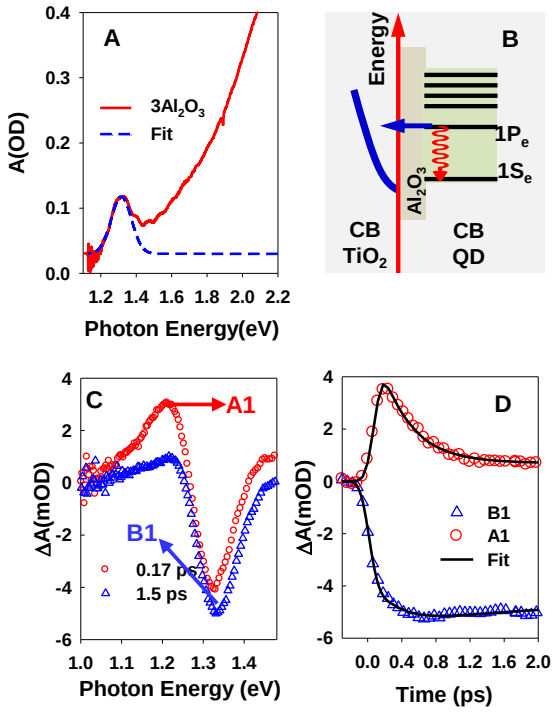

Figure 6.5. (A) Visible-NIR absorption spectrum of PbS QDs on TiO_2 with 3 ALD layers ($3Al_2O_3$) and Gaussian fit. (B) Schematic illustration of the 1P electron injection from PbS to $3Al_2O_3/TiO_2$ films. (C) TA spectra of the $PbS/3Al_2O_3/TiO_2$ at indicated delay times after 2.12eV excitation. (D) A1 (red circles) and B1 (blue triangles) kinetics and their fits (dashed lines) by exponential growth and decay functions.

Figure 6.5 A shows the absorption spectrum of PbS QDs on $3Al_2O_3$ ($PbS/3Al_2O_3/TiO_2$). The Gaussian fitting of the 1S exciton absorption band confirms that the adsorption of QDs leads to negligible spectral broadening of the 1S excition transition, in agreement with the slow 1S electron transfer rate discussed above. To investigate the 1P electron injection, we directly excited the 1P exciton at 2.12 eV. As elucidated in Figure 6.5 B, the 1P electron can either relax to 1S state or transfer to the CB of TiO_2 by tunneling through the Al_2O_3 layer. The injection yield is defined as the ratio of the number of injected electron to the number of the 1P electron. As shown in Figure 6.5 C, like in the free PbS QDs, at 0.17 ps , the TA spectrum shows a clear A1

feature centered at ~1.2 eV, indicating the presence of 1P exciton. At 1.5 ps, the A1 feature has decay and the TA spectrum is dominated by the state filling induced exciton bleach signal (B1 feature). As shown in Figure 6.5 D, the A1 and B1 kinetics can be fit according to the model used to describe the kinetics of free QDs (Figure 6.3). The best exponential fits reveal a 1P excion decay rate constant of 2.7±0.4 ps^{-1}, which is slightly faster than the 1P exciton relaxation rate in free QDs, although the difference is within the error bar of the measurement. A reduced 1P exciton lifetime could be consistent with the presence of additional 1P electron decay channel by hot electron transfer to TiO_2. Since A1 feature arises from both 1P electron and hole, the 1P electron kinetics cannot be isolated from A1 kinetics. Without knowing the 1P electron kinetics, we are not able to estimate the 1P electron injection yield by the ratio of the 1P electron injection rate to the total decay rate of 1P electron. However, if a part of the 1P electrons is injected to the TiO_2 film, the amount of electrons relaxing to the 1S electron levels is reduced and smaller 1S exciton bleach can be expected. Thus, we can estimate the hot injection yield by comparing the amplitude of A1 and B1 feature.

As demonstrated in Appendix 1, the 1S electron and hole contribute equally to the 1S exciton bleach. The 1S exciton bleach (maximum amplitude of B1 feature, $B1_{max}$) should be proportional to the total number of 1S electron and holes and can be expressed as:

$$N(1S_e + 1S_h) = \alpha_{1S} B1_{max} \quad (6.1)$$

where α_{1S} is a constant related to the absorption coefficient of 1S electron and hole. The maximum amplitude of the A1 feature should be proportional to the number of 1P exciton and can be written as:

$$N(1P) = \alpha_{1P} A1_{max} \quad (6.2)$$

where α_{1P} is a constant related to the absorption coefficient of the 1P induced A1 feature. In the PbS solution, one 1P exciton should form one 1S electron and one 1S hole, $N(1S_e + 1S_h) =$

$2N(1P)$. Based on the TA measurement of PbS solution, we can introduce a scaling factor $\alpha=2\alpha_{1P}/\alpha_{1S}=B1_{max}/A1_{max}=1.69\pm0.06$.

For $PbS/3Al_2O_3/TiO_2$, in the presence of 1P electron injection, the number of the 1S electron should be smaller than 1P exciton, but the number of the 1S hole should be equal to the number of the 1P exciton. Combining eqs 6.1 and 6.2, the number of the 1S electron can be written as:

$$N(1S_e) = N(1S_e + 1S_h) - N(1S_h) = \alpha_{1S}B1_{max} - \alpha_{1P}A1_{max} \quad (6.3)$$

Then, the hot injection yield (η) can be calculated by the following equation:

$$\eta = \frac{N(1P_e) - N(1S_e)}{N(1P_e)} = 1 - \frac{\alpha_{1S}B1_{max} - \alpha_{1P}A1_{max}}{\alpha_{1P}A1_{max}} = 2 - \frac{2B1_{max}}{\alpha A1_{max}} \quad (6.4)$$

According to eq 6.4, the 1P electron injection yield for $PbS/3Al_2O_3/TiO_2$ is determined to be 18 ± 4 %.

6.2.4. Hot electron injection from high energy level (higher than 1P) of PbS to TiO_2

To exploring the electrons injection from high energy state (higher than 1P state), we need to increase the excitation photon energy to generate higher energy exctions. However, as indicated by the 3.10 eV pump TA experiment, the electron relaxation from the higher energy level is much faster than the 1P electron relaxation, considering the temporal width of the laser pulses (~150 fs) in this experiment, the recorded A1 feature is probably not caused by the initially generated exciton but some unknown levels higher than 1P. In addition, the observed A1 amplitude is likely smaller than the real value because of the non-instantaneous growth arising from the cascading hot exciton relaxation process and the fast decay. TA measurements with faster time resolution or alternatively techniques would be needed. We are planning on using time-resolved terahertz technique to study the hot electron injection from energy levels higher than 1P. This technique will allow us to directly follow the injected electron kinetics in conduction band of the TiO_2.

Theoretically, the dependence of hot electron transfer yield on the excitation energy and Al_2O_3 thickness can be predicted by an electron transfer (ET) model. In this model, above the 1P electron level, space between energy levels is very small and the conduction band becomes nearly continuous. The electron at higher energy position can either relax to lower energy position with relaxation rate k_R or transfer to the film with ET rate k_{ET}. Thus, the hot electron injection efficiency can be written as

$$\eta(E,d) = 1 - \prod_{i=0}^{\frac{E}{\delta E}} \frac{k_R(E_i)}{k_{ET}(E_i,d) + k_R(E_i)} \quad (6.5)$$

where δE is defined as the energy space between two energy levels. The ET rate (k_{ET}) can be described by the following expression[45]

$$k_{ET}(E) = \frac{2\pi}{\hbar}\int_0^{\infty} dE\rho(E)S(E)\frac{1}{\sqrt{4\pi\lambda k_B T}}\exp[-\frac{(\lambda + \Delta G - E)^2}{4\lambda k_B T}] \quad (6.6)$$

where ρ(E) is the density of state of TiO_2 that is proportional to square root of energy in the free electron approximation; ΔG is the energy difference between hot electron state and the conduction bandedge of TiO_2; and λ is the total reorganization energy; S(E) is the tunneling probability that is related to the barrier height and tunneling length (Al_2O_3 layer thickness), expressed as

$$S(E,d) \propto \exp\left(-\frac{\sqrt{8m}}{\hbar}\sqrt{\beta(V_B - E)}d\right) \quad (6.7)$$

where m is the effective mass of electron (m=0.4m_0, m_0 is the mass of free electron) in the Al_2O_3 layer,[46] β is a constant, d is the thickness of the Al_2O_3 layer, V_B is the energy difference between Al_2O_3 CB edge (-0.5 eV vs vacuum)[47] and PbS QD 1S level (-3.7 eV *vs* vacuum),[42, 48] and V_B–E is the energy barrier for electron with energy E. The tunneling probability is thus function of both electron energy and Al_2O_3 layer thickness. Due to the rigid structures of the QDs and TiO_2

nanoparticles, the total reorganization energy (λ) is small (<10 meV)[14, 49] and we can assume that the electron transfer between resonant energy levels dominates the electron transfer rate. Therefore, The hot electron transfer rate, k_{ET}(E,d), is proportional to the product of ρ(E) and S(E,d), and can be expressed as $k_{ET}(E,d)=C_1 \cdot \rho(E) \cdot S(E,d)$ where C_1 is a constant. It was shown previously that hot electron relaxation rate in PbSe QDs was proportional to the electron energy, although the mechanism of the relaxation needs further investigation.[24] Due to the similar electronic structure of PbS and PbSe,[42] we assume that k_R(E) is also proportional to the electron energy, expressed as $k_R(E)= C_2 \cdot E$. Thus, we can substitute the expressions of both k_{ET}(E,d) and k_R(E) into eq. 6.5 to obtain the hot electron injection yield as function of electron energy (E) and Al_2O_3 thickness (d):

$$\eta(E,d) = 1 - \prod_{i=0}^{\frac{E}{\delta E}} \frac{C_2 E_i}{C_1 \rho(E_i) S(E_i,d) + C_2 E_i} \qquad (6.8)$$

The plots of η as function of electron energy or Al_2O_3 layer thickness are shown in Figure 6.6. We can see that the hot injection yield increases with the increase of electron energy and decrease of the aluminum oxide film thickness.

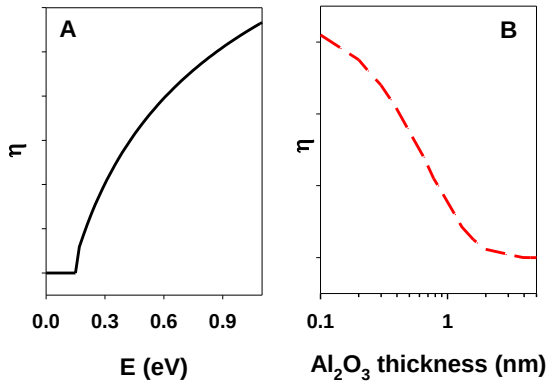

Figure 6.6. The calculated η as function of (A) electron energy or (B) Al_2O_3 layer thickness. The equation of these plots are shown as eq 6.8.

6.3. Conclusion.

In summary, we found that the hot injection efficiency from PbS to TiO_2 coated by 0.33 nm Al_2O_3 layer was as high as 18±4 %. Our results demonstrate that extracting hot electron from lead chalcogenide QDs by oxide films is possible, and considerable injection efficiency can be achieved even in the system that back ET is significantly suppressed by insulating layers.

Reference.

1. Bawendi, M. G.; Steigerwald, M. L.; Brus, L. E. *Annu. Rev. Phys. Chem.* **1990,** 41, (1), 477-496.

2. Murray, C. B.; Kagan, C. R.; Bawendi, M. G. *Annu. Rev. Mater. Sci.* **2000,** 30, (1), 545-610.

3. Choi, C. L.; Alivisatos, A. P. *Annu. Rev. Phys. Chem.* **2010,** 61, (1), 369-389.

4. Efros, A. L.; Rosen, M. *Annu. Rev. Mater. Sci.* **2000,** 30, (1), 475-521.

5. Knowles, K. E.; Malicki, M.; Weiss, E. A. *J. Am. Chem. Soc.* **2012,** 134, (30), 12470-12473.

6. Burda, C.; Green, T. C.; Link, S.; El-Sayed, M. A. *J. Phys. Chem. B* **1999,** 103, (11), 1783-1788.

7. Hyun, B. R.; Zhong, Y. W.; Bartnik, A. C.; Sun, L. F.; Abruna, H. D.; Wise, F. W.; Goodreau, J. D.; Matthews, J. R.; Leslie, T. M.; Borrelli, N. F. *ACS Nano* **2008,** 2, (11), 2206-2212.

8. Jin, S.; Lian, T. *Nano Lett.* **2009,** 9, (6), 2448-2454.

9. Tisdale, W. A.; Williams, K. J.; Timp, B. A.; Norris, D. J.; Aydil, E. S.; Zhu, X. Y. *Science* **2010,** 328, (5985), 1543-1547.

10. Yang, Y.; Rodríguez-Córdoba, W.; Xiang, X.; Lian, T. *Nano Lett.* **2011,** 12, (1), 303-309.

11. Cánovas, E.; Moll, P.; Jensen, S. A.; Gao, Y.; Houtepen, A. J.; Siebbeles, L. D. A.; Kinge, S.; Bonn, M. *Nano Lett.* **2011,** 11, (12), 5234-5239.

12. Huang, J.; Huang, Z.; Jin, S.; Lian, T. *J. Phys. Chem. C* **2008,** 112, (49), 19734-19738.

13. Matylitsky, V. V.; Dworak, L.; Breus, V. V.; Basche, T.; Wachtveitl, J. *J. Am. Chem. Soc.* **2009,** 131, (7), 2424.

14. Tvrdy, K.; Frantsuzov, P. A.; Kamat, P. V. *Proc. Natl. Acad. Sci. U. S. A.* **2011,** 108, (1), 29-34.

15. Zhu, H.; Yang, Y.; Lian, T. *Acc. Chem. Res.* **2012**.

16. Tseng, H.-W.; Wilker, M. B.; Damrauer, N. H.; Dukovic, G. *J. Am. Chem. Soc.* **2013**.

17. Zhu, H.; Song, N.; Lian, T. *J. Am. Chem. Soc.* **2011,** 133, (22), 8762-8771.

18. Zhu, H.; Song, N.; Lian, T. *J. Am. Chem. Soc.* **2010,** 132, (42), 15038-15045.

19. Brovelli, S.; Schaller, R. D.; Crooker, S. A.; García-Santamaría, F.; Chen, Y.; Viswanatha, R.; Hollingsworth, J. A.; Htoon, H.; Klimov, V. I. *Nat Commun* **2011,** 2, 280.

20. Oron, D.; Kazes, M.; Banin, U. *Phys. Rev. B* **2007,** 75, (3), 035330.

21. Semonin, O. E.; Luther, J. M.; Choi, S.; Chen, H.-Y.; Gao, J.; Nozik, A. J.; Beard, M. C. *Science* **2011,** 334, (6062), 1530-1533.

22. Sambur, J. B.; Novet, T.; Parkinson, B. A. *Science* **2010,** 330, (6000), 63-66.

23. Yang, Y.; Rodríguez-Córdoba, W.; Lian, T. *Nano Lett.* **2012,** 12, (8), 4235-4241.

24. Miaja-Avila, L.; Tritsch, J. R.; Wolcott, A.; Chan, W. L.; Nelson, C. A.; Zhu, X. Y. *Nano Lett.* **2012,** 12, (3), 1588-1591.

25. Gdor, I.; Sachs, H.; Roitblat, A.; Strasfeld, D. B.; Bawendi, M. G.; Ruhman, S. *ACS Nano* **2012,** 6, (4), 3269-3277.

26. Stewart, J. T.; Padilha, L. A.; Qazilbash, M. M.; Pietryga, J. M.; Midgett, A. G.; Luther, J. M.; Beard, M. C.; Nozik, A. J.; Klimov, V. I. *Nano Lett.* **2011,** 12, (2), 622-628.

27. Pijpers, J. J. H.; Ulbricht, R.; Tielrooij, K. J.; Osherov, A.; Golan, Y.; Delerue, C.; Allan, G.; Bonn, M. *Nat. Phys.* **2009,** 5, (11), 811-814.

28. Pandey, A.; Guyot-Sionnest, P. *Science* **2008,** 322, (5903), 929-932.

29. Nozik, A. J. *Annu. Rev. Phys. Chem.* **2001,** 52, (1), 193-231.

30. Nozik, A. J. *Phys. E* **2002,** 14, (1-2), 115-120.

31. Guyot-Sionnest, P.; Wehrenberg, B.; Yu, D. *J. Chem. Phys.* **2005,** 123, (7), 074709-7.

32. Wehrenberg, B. L.; Wang, C. J.; Guyot-Sionnest, P. *J. Phys. Chem. B* **2002,** 106, (41), 10634-10640.

33. Harbold, J. M.; Du, H.; Krauss, T. D.; Cho, K.-S.; Murray, C. B.; Wise, F. W. *Phys. Rev. B* **2005,** 72, (19), 195312.

34. Schaller, R. D.; Pietryga, J. M.; Goupalov, S. V.; Petruska, M. A.; Ivanov, S. A.; Klimov, V. I. *Phys. Rev. Lett.* **2005,** 95, (19), 196401.

35. Klimov, V. I.; Mikhailovsky, A. A.; McBranch, D. W.; Leatherdale, C. A.; Bawendi, M. G. *Phys. Rev. B* **2000,** 61, (20), R13349.

36. Klimov, V. I. *J. Phys. Chem. B* **2000,** 104, (26), 6112-6123.

37. Klimov, V. I.; McBranch, D. W. *Phys. Rev. Lett.* **1998,** 80, (18), 4028-4031.

38. Cooney, R. R.; Sewall, S. L.; Anderson, K. E. H.; Dias, E. A.; Kambhampati, P. *Phys. Rev. Lett.* **2007,** 98, (17), 177403.

39. Kilina, S. V.; Craig, C. F.; Kilin, D. S.; Prezhdo, O. V. *J. Phys. Chem. C* **2007,** 111, (12), 4871-4878.

40. Pandey, A.; Guyot-Sionnest, P. *J. Phys. Chem. Lett.* **2009,** 1, (1), 45-47.

41. Tang, J.; Kemp, K. W.; Hoogland, S.; Jeong, K. S.; Liu, H.; Levina, L.; Furukawa, M.; Wang, X.; Debnath, R.; Cha, D.; Chou, K. W.; Fischer, A.; Amassian, A.; Asbury, J. B.; Sargent, E. H. *Nat. Mater.* **2011,** 10, (10), 765-771.

42. Kang, I.; Wise, F. W. *J. Opt. Soc. Am. B* **1997,** 14, (7), 1632-1646.

43. Nootz, G.; Padilha, L. A.; Levina, L.; Sukhovatkin, V.; Webster, S.; Brzozowski, L.; Sargent, E. H.; Hagan, D. J.; Van Stryland, E. W. *Phys. Rev. B* **2011,** 83, (15), 155302.

44. Klimov, V. I.; Mikhailovsky, A. A.; McBranch, D. W.; Leatherdale, C. A.; Bawendi, M. G. *Science* **2000,** 287, (5455), 1011-1013.

45. Miller, R. J. D.; McLendon, G. L.; Nozik, A. J.; Schmickler, W.; Willig, F. *Surface Electron Transfer Processes; VCH: New York* **1995**.

46. No, S. Y.; Eom, D.; Hwang, C. S.; Kim, H. J. *J. Electrochem. Soc.* **2006,** 153, (6), F87-F93.

47. Palomares, E.; Clifford, J. N.; Haque, S. A.; Lutz, T.; Durrant, J. R. *J. Am. Chem. Soc.* **2002,** 125, (2), 475-482.

48. Yang, Y.; Rodríguez-Córdoba, W.; Lian, T. *J. Am. Chem. Soc.* **2011,** 133, (24), 9246-9249.

49. Scholes, G. D.; Jones, M.; Kumar, S. *J. Phys. Chem. C* **2007,** 111, (37), 13777-13785.

Appendix 1.

To determine the relative contribution of 1S electron and hole to the 1S exciton bleach, we use the MB^+ molecule as electron acceptor to dissociate the 1S electron and hole of the QDs. The analysis is same as in our previous study in chapter 3, in which the kinetics of 1S(h)→ 1P(h) intraband transition at 5 μm is scaled and compared with the 1S interband kinetics to obtain the respective 1S electron and hole contributions. The TA spectra and the corresponding kinetics of free PbS and PbS-MB^+ complex are shown in Figure A.1 A and B, respectively. In panel B, the normalized intraband transition kinetics indicates the 1S hole dynamics and the 1S bleach kinetics represents the total dynamics of 1S electron and hole. Hence, the ratio of the initial amplitude of this normalized intraband transition kinetics to the 1S bleach kinetics is the the fraction of the 1S hole caused bleach out of the total 1S exciton bleach. This ratio is determined as 50%, indicating that the 1S electron and 1S hole contribute equally to the 1S exciton bleach.

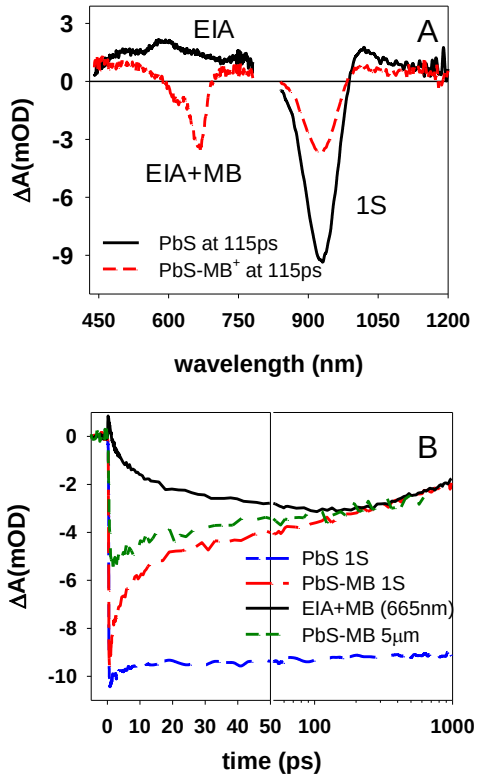

Figure A.6.1. (A) The transient spectra of PbS QDs (black solid line) and PbS-MB^+ complexes (red dashed line) at 115 ps delay time. (B) The kinetics of 1S bleach (red medium dashed line), overlapping of exciton induced absorption (EIA) and MB^+ ground state bleach (MB) (black solid line), and 1S(e)→1P(h) intraband transition at 5 μm (blue medium dash) of the complex. The intraband transition was normalized to match the 1S bleach decay and EIA+MB at long-term delay time. Also shown is the 1S bleach kinetics of free QDs (blue short dashed line). It should be noted that the electron transfer and recombination rate in this experiment are slower than them in chapter 3, which is attributed to the lower ratio of MB^+ to QDs in this experiment.

Chapter 7. Coupled Electron and Hole Transport in CdSe Tetrapod Nanocrystals

7.1. Introduction.

Recently, the advance in synthesis of the heterostructured semiconductor nanocrystals offers exciting opportunities for the applications of solar energy conversion. The electronic structures in these nanocrystals can be engineered for desired photon conversion processes by varying the size, shape, composition and crystal structure of the constituent components in the heterostructures,.[1-7] Indeed, many types of heterostructured nanocrystals, like core-shell, tetrapod, and dot-in-rod nanostructures, are designed to more efficiently harvest sunlight and deliver the photo-induced charges for solar energy conversion.[4, 8-12]

Among these heterostuctures, branched morphology has attracted intensive interest in solar-to-fuel conversion.[4, 10, 11] The one dimensional (1D) branch can serve as an efficient antenna for light harvesting due to the giant absorption coefficient.[13, 14] The charge carrier generated in the branch can then be directed to the reaction sites. Since the solar-to-fuel conversion reactions such as light driven water splitting or CO_2 reduction require multiple charges in one reaction step, to achieve high energy conversion efficiency under solar flux, the excited artificial molecules must be able to keep absorbing photons and transporting charge carriers to reaction site. Unlike conventional molecules, the electronic structure of the semiconductor nanocrytals is not significantly changed in the presence of electron and/or hole, which make the excited particles as the excellent light harvesters. However, the charge carrier transport process in excited artificial molecules still remains open questions due to the lack of studies.

In this chapter, we investigated the charge transport dynamics in the excited CdSe tetrapod (TP) by the two- and three-pulse transient absorption (2P-TA and 3P-TA) spectroscopy. CdSe TP

nanocrystals are composed of a core at the center and four branches. The 2P-TA measurement showed that the electron initially in the branch of CdSe TP quickly relaxed to the center (τ ~1.5 ps) and resulted in a long lived first excited state (τ ~0.83 ns). In the 3P-TA measurement, we found that, in the presence of an electron in the core, the photo-generated electrons in the branch of the excited TPs showed two different behaviors due to the Pauli Exclusion Principle. Half of these electrons with the same spin as the electrons at the core stay in the branches, while the other half with the opposite spin are transported to the center with a rate similar to the TP without an electron in the core. The electron transport kinetics was not retarded by the repulsion of pre-excited electron localized in the core, suggesting the coupled electron and hole transport, which was possibly due to the large exciton binding energy caused by 1D dielectric confinement in the braches.

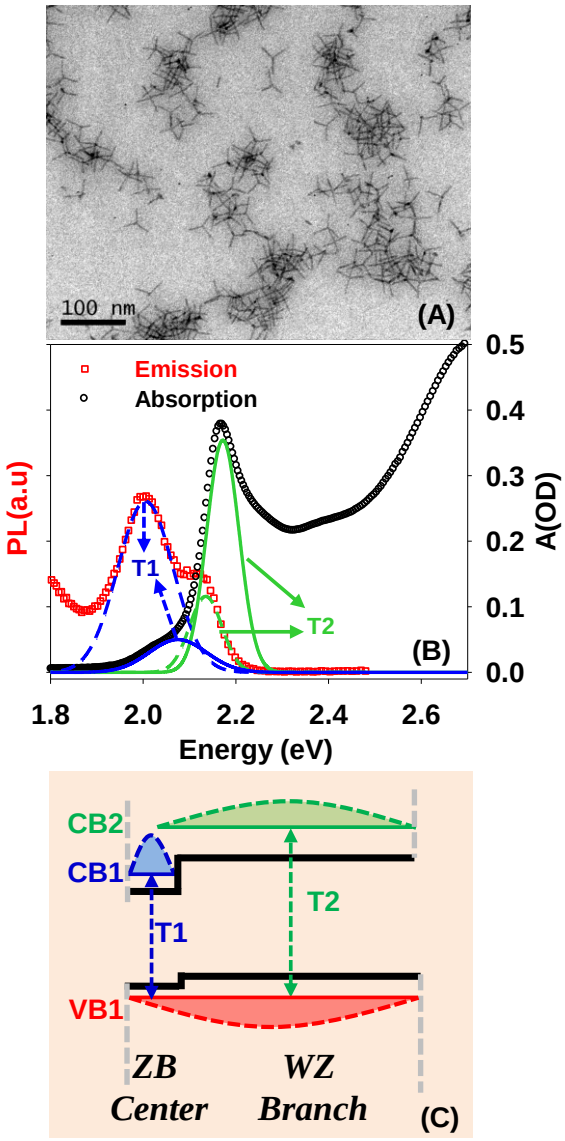

Figure 7.1. (A) TEM image of CdSe TP. (B) Absorption and emission spectra of CdSe TP. Two peaks are resolved by Gaussian fits of the spectra near band gap and assigned to two different transitions as indicated as T1 (blue lines) and T2 (green lines). (B) Schematic diagram of the electronic energy levels and electron and hole wavefunctions in CdSe TP. Two lowest electron states, CB1 and CB2, are mainly localized in center and branch of the TP, respectively. The lowest hole state, VB1, is delocalized in the entire nanostructure. Transitions from VB1 to CB1 and CB2 correspond to the two lowest transitions T1 and T2 in absorption and emission spectra. Black solid lines indicate the band alignment of the bulk ZB and WZ CdSe.

7.2 Results and discussions.

7.2.1. Band alignment and electronic transitions in CdSe TPs.

The CdSe TP was synthesized by slightly modifying a published procedure,[15-17] and the specifics were described in Chapter 2. In the current paper, TP was dispersed in chloroform solution for spectroscopic studies. The TEM image (Figure 7.1 A) of the investigated sample shows that branches of the TP are 23.3±2.4 nm in length and 2.4±0.4 nm in diameter. The absorption spectrum of the sample is shown in Figure 7.1 B. Two absorption bands near band gap are clearly resolved by the fit of two Gaussian functions. The centers and widths (FWHM) of these absorption bands are determined as (2.07 eV, 132 meV) and (2.17 eV, 82 meV) from the best fits. Also shown in this figure is emission spectrum. The Gaussian fit gives the centers and widths of the two emission bands near band gap as (2.01 eV, 132 meV) and (2.13 eV, 82 meV). According to the band width, the absorption and emission bands are attributed to two transitions indicated as T1 and T2 and the Stokes shifts for T1 and T2 are 69 and 40 meV. The origin of T1 and T2 is going to be discussed in the following paragraph.

Previous studies have demonstrated that CdSe TP nanocrystals comprise a center in zinc blend (ZB) structure and four branches in wurtzite (WZ) structure.[18-20] The conduction band (CB) and valence band (VB) offsets between the bulk WZ and ZB CdSe are 94 and 35 meV, respectively, resulting in a type II band alignment.[21] However, due to the stronger quantum confinement in the branches (radial direction) than in the center, the CB offset is further enlarged, while the VB offset is reduced. According to the effective mass calculation (Appendix 1), the VB offset of the reported sample is estimated as ~6 meV, the VB of TPs is thus barrier-less at room temperature (K_bT~26 meV), suggesting a quasi-type II band alignment in the sample. As

elucidated in Figure 7.1 C, the lowest electron state (CB1) of the TP is localized in the center due to the energy gap between this state and the lowest electron state in the branches (CB2). The lowest hole state (VB1) of the TP is delocalized in the entire nanostructure because of the lack of energy barrier. The assumption of the wave-function density distribution for these states based on the respective energy levels is consistent with theoretical calculation based on semiempirical pseudopotential method.[22] According to the electronic structure sketched in Figure 7.1 C, T1 and T2 can be assigned to the transitions from VB1 to CB1 at the center and to CB2 in the branch, respectively. Because the four 1D branches have much larger absorption cross sections than the core at the center,[13, 14] the absorption at T2 transition should be much stronger than that at T1 transition, which was confirmed by the absorption spectra in Figure 7.1 B.

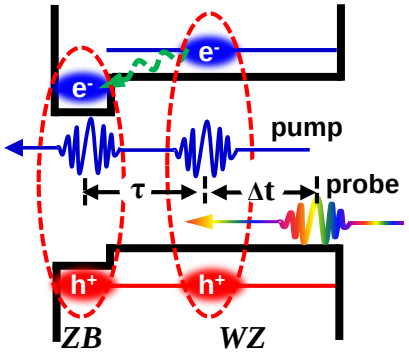

Figure 7.2. Schematic illustration of the 3P-TA experiment (see main text for details).

7.2.2. Three-pulse and two-pulse TA measurements.

To unambiguously monitor the exciton dynamics in the excited CdSe TPs, 3P-TA technique is exploited by adding a pre-pump pulse in the common 2P-TA measurement. As shown in Figure

7.2, the pre-pump is introduced into the system in advance of the pump by τ, and the probe pulse is delayed by Δt after the pump. The photon energy of the pre-pump is 3.1 eV, same as the pump. The probe is broad band in visible region (1.6-2.9 eV). The intensity of the pre-pump is tuned to excite all nanocrystals in the excitation zone. The delay τ is chosen to allow all the multiple excitons decays to single excitons when the pump arrives at that excitation zone. The intensity of the pump is the same as in 2P-TA measurement. By varying Δt, the probe can interrogate the exciton created by the pump in the excited TPs. The detail information of the setup is described in Chapter 2.

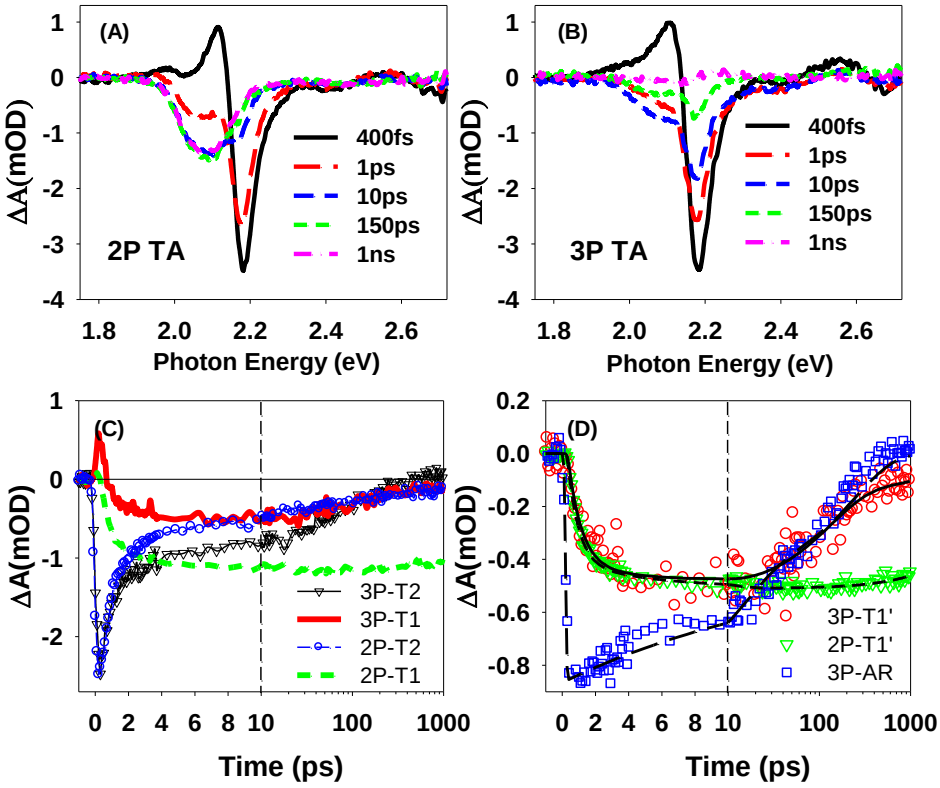

Figure 7.3. TA spectra of CdSe TP for the (A) 2P and (B) 3P experiments. (C) Kinetics of T1 and T2 bleach in 2P (2P-T1 and 2P-T2) and 3P (3P-T1, 3P-T2) experiments (see the main text for T1 and T2 assignments). (D) Comparison of the 2P-T1 and 3P-T1 kinetics after subtracting the bi-

exciton contribution. 2P-T1 kinetics was also scaled by multiplying ½. Also plotted is the difference kinetics (3P-AR) from 3P-T2 minus ½(2P-T2), reflecting the Auger process of the two excitons generated by two pump in the 3P experiment (see the main text). The black lines are the fits.

We started with investigating the exciton dynamics in TPs by the 2P-TA spectroscopy. Figure 7.3 A shows the TA spectra of the sample recorded at the indicated time delay after a single excitation. In this experiment, the pump intensity is as low as 1.0 nJ/pulse to avoid multiple photon absorption by a single TP. Two distinctive bleach signals centering at 2.18 and 2.07 eV are detected, corresponding to the photobleaching of T2 and T1 absorption bands, respectively. The widths of these two bleach peaks are also in good agreements with their corresponding absorption band. By measuring the electron transfer from the TP to molecular electron acceptors (Appendix 2), we demonstrated that the bleach was only caused by the state filling of electron states. The TA measurement of TP with electron acceptors is going to be discussed later. At short delay time (<10 ps), the formation of T1 bleach and recovery of T2 bleach occur simultaneously. The T1 bleach arrives at the maximum when the T2 bleach fully recovers. This TA spectra evolution suggests that the electron initially populates CB2 state in the branches, consistent with the fact that the branch has much larger absorption coefficient at the excitation region, and then migrates to the CB1 state at the center. The completely formed T1 bleach shows negligible decay until 1ns, indicating the long life time of the single electron in CB1 state. The lifetime of the electron in CB1 is determined as 90.7±5.8 ns by the nanosecond TA measurement.

To investigate the exciton dynamics in the excited TPs, the 3P-TA experiment was conducted by introducing a pre-pump into the 2P-TA measurement discussed above and keeping other experimental conditions identical. To guarantee that every nanocrystal is excited by the first

pump, a pump power dependent experiment is carried out. Like in quantum dots, multiple excitons in TPs generated by multiple excitations are short lived due to the ultrafast Auger process. At long time delay (~1 ns), the bleach signal at long time delay is attributed to the long lived single electron in CB1 state. In this experiment, the T1 bleach signal (at 2.03 V) at 1ns was saturated to ~12 mOD when the intensity of the pump was larger than 200 nJ/pulse, suggesting that all TPs were excited beyond this excitation intensity. The intensity of the pre-pump was set as 312 nJ/pulse to ensure exciting all nanocrystals. The Auger recombination annihilated most of the multiple excitons before 350 ps, so the delay τ was set as 362 ps. Figure 7.3 B shows the TA spectra of the sample recorded at the indicated delay time (Δt). The two bleach peaks, T1 and T2, can still be observed. The maximum amplitude of T2 bleach is the same as that in the 2P-TA experiment, implying that the amount of excitons generated by pump in 3P-TA measurement is as many as that in 2P-TA measurement. T1 bleach formation is accompanied by the T2 bleach recovery, but the T2 bleach is not fully recovered when the T1 bleach arrives at the maximum. The T1 bleach undergoes a fast decay after the fully formation, which is attributed by the fast Auger process between the new exciton and the pre-excited exciton.[23] At 1ns, the residue of the TA spectrum resembles the derivative of the absorption spectrum. This small TA signal is possibly due to the Stark effect induced spectral shifting arising from the redistribution of the holes in TP after the Auger process.[1, 24] The maximum signal of T1 bleach is only half large as that in the 2P-TA experiment due to the Pauli Exclusion Principle, according to which two electrons with same spin cannot occupy the same CB1 state. Since half of the electrons generated by the pump possess the same spin as the electron in CB1 state arising from the pre-pump, only the other half can populate the half occupied CB1 state and raise the T1 bleach. The detail mechanism of the electron spin relaxation in quantum confined nanocrystals is not discussed in current study.

The TA kinetics of T1 and T2 bleach are shown in Figure 7.3 C. As indicated by the legend, the kinetics of T1 and T2 bleach for the 2P-TA or 3P-TA experiment are referred as 2P-T1 and 2P-T2, or, 3P-T1 and 3P-T2, respectively. For both experiments, the kinetics of T1 and T2 bleach are recorded at 2.03 and 2.22 eV of the TA spectra to avoid the overlapping region of the two bleach peaks. The comparison shows that 3P-T2 decays slower than 2P-T2 and 3P-T1 decays faster than 2P-T1. The maximum amplitudes of 2P-T2 and 3P-T2 are the same, but maximum amplitude of 2P-T1 is twice larger than 3P-T1. Since bi-exciton induced T2 absorption (the positive spectral feature at the lower energy side of the T1 bleach[25, 26]) overlaps with T1 bleach, the corrected T1 bleach kinetics can be obtained by subtracting the bi-exciton contribution from the T1 kinetics. The bi-exciton decay kinetics was independently probed at 1.87-1.85 eV photon energy. As shown in Figure 3D, the corrected 2P-T1 was scaled by multiplying ½ and then compared with the corrected 3P-T1. The 2P-T1 and 3P-T1 formation lifetimes are determined as 1.5±0.2 ps and 1.6±0.4 ps from the bi-exponential fits, and the consistent formation trend of these two kinetic traces suggests the similar electron transport rate. The Auger recombination rate is also estimated as 129±35 ps by fitting the 3P-T1 recovery. Because only half of the electrons at the CB2 state in the excited TPs can relax to the CB1 state due to the Pauli Exclusion Principle, 3P-T2 kinetics should contain the contribution from the other half electrons at the CB2 state, which is responsible for the different T2 bleach kinetics in the 2P-TA and 3P-TA experiments. We can use 2P-T2 kinetics with its amplitude scaled to half (½(2P-T2)) to simulate the contribution of the electrons that are allowed to relax to the CB1, thus the kinetics of the rest electrons will be the difference kinetics between 3P-T2 and ½(2P-T2), which is linearly scaled and compared with 3P-T1 kinetics in Figure 7.3 D (indicated as 3P-AR). The lifetime of the 3P-AR decay is determined as 137±48 ps from the bi-exponential fit, which is in agreement with the 3P-T1 recovery (129±35 ps), indicating the electrons remaining in CB2 state undergo the similar Auger process as the electrons relaxed to CB1. The small discrepancy at long time delay (500-1000ps) is due to the derivative-like TA spectrum (Figure 3B, TA spectrum at 1ns).

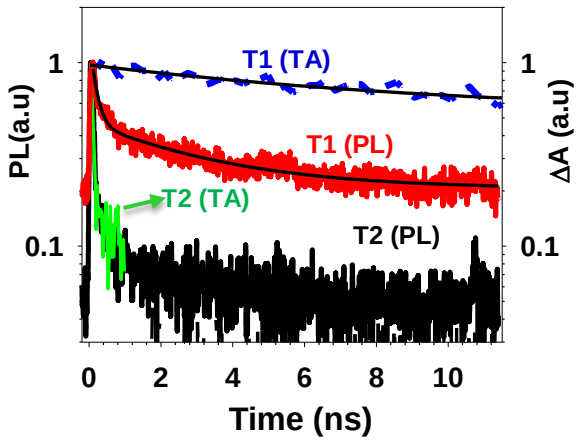

Figure 7.4. Decay kinetics of the photoluminescence (PL) from T1 and T2 transition and the inversed TA kinetics of T1and T2 bleach. These kinetic trances are normalized to 1 at 0.2 ns. The black solid lines are the bi-exponential fits.

7.2.3. Association of electron and hole transport.

To follow the kinetics of holes in the TP, the time resolved photoluminescence (PL) experiment were carried out. The TP sample was excited at 3.1 eV. The florescence of the sample was sent to a monochromator and then detected by a PMT. According to the emission spectrum shown in Figure 7.2, we are able to selectively measure kinetics of the PL from T1 and T2 transition (T1-PL and T2-PL) by detecting at 1.97 and 2.19 eV, respectively. Figure 7.4 shows normalized the T1-PL and T2-PL kinetics as well as the TA kinetics of T1 and T2 bleach that are inversed and normalized to 1 at 0.1 ns. T2-PL decays more than 90% within 400 ps, consistent with the T2 bleach decay in TA measurement. This consistence suggests that T2-PL quenching is dominated by the electron moving from CB2 to CB1. T1-PL decays much faster than T1 bleach,

indicating that the quenching of PL for T1 transition is determined by the lifetime of hole instead of electron in CB1 state. The lifetime of the hole can be measured as ~825±52 ps from the T1-PL kinetics. The hole trap states possibly account for the short life time of the holes, supported by the strong trap state emission (the broad peak centering at 1.63 eV[27, 28]) in the emission spectrum (Figure 7.1 B). On the other hand, the PL measurement also implies that the hole should be delocalized and mobile on the timescale of electron transport.

Due to the delocalized VB1 and relatively slow hole trapping (τ~ 0.83 ns), the hole wave-function should be extended in the whole nanostructure on the timescale of electron transport. In this case, transporting an electron to the center that is already occupied by another electron must be retarded by the Coulomb repulsion between two electrons although this repulsion is partially screened by the delocalized holes. This scenario is, however, contrary to our experimental observation. As demonstrated by our previous study of the exciton dissociation in 1D nanostructure, the large binding energy of exciton as consequence of the 1D dielectric confinement effect will cause a strong association between the electron and hole.[29-32] Therefore, in the 1D branch of the TPs, the electron and hole could possibly move together to the center due to the large binding energy. Since the exciton pair is neutral, the first exciton cannot electrically repel or attract the second one if we neglect the polarization of exciton states, which can well explain the similar electron transport kinetics in the branches of the unexcited and excited TPs.

7.3. Conclusion.

In conclusion, we demonstrated that in CdSe TP the electrons initially generated in the branches could be quickly transported to the center ($\tau_{1/2}$ ~1ps) by 2P-TA measurement. Our 3P-TA experiment showed that, due to the Pauli Exclusion Principle, half of the new generated

electrons in excited TPs could be transported to the center as fast as in unexcited TPs, while the other half stay in the branch. The similar electron transport rate in excited and unexcited TPs indicates the coupled electron and hole transport probably resulting from the large exciton binding energy in the braches. Our finding suggests that if the artificial molecules can deliver the charges to the catalysts faster than Auger recombination, the efficiency of light absorbing and charge transporting will be the same for them in excited state and in ground state. For the multiple electron (hole) catalytic reaction, the efficiency of multiple electrons (holes) collection is also limited by the degeneracy of the electron (hole) states due to the Pauli Exclusion Principle.

Reference.

1. Zhu, H.; Song, N.; Lian, T. *J. Am. Chem. Soc.* **2010,** 132, (42), 15038-15045.

2. Zhu, H.; Song, N.; Lian, T. *J. Am. Chem. Soc.* **2011,** 133, (22), 8762-8771.

3. Zhu, H.; Lian, T. *J. Am. Chem. Soc.* **2012,** 134, (27), 11289-11297.

4. Zhu, H.; Song, N.; Lv, H.; Hill, C. L.; Lian, T. *J. Am. Chem. Soc.* **2012,** 134, (28), 11701-11708.

5. Zhu, H.; Song, N.; Rodríguez-Córdoba, W.; Lian, T. *J. Am. Chem. Soc.* **2012,** 134, (9), 4250-4257.

6. Justo, Y.; Goris, B.; Kamal, J. S.; Geiregat, P.; Bals, S.; Hens, Z. *J. Am. Chem. Soc.* **2012,** 134, (12), 5484-5487.

7. Zavelani-Rossi, M.; Lupo, M. G.; Tassone, F.; Manna, L.; Lanzani, G. *Nano Lett.* **2010,** 10, (8), 3142-3150.

8. Huang, J.; Mulfort, K. L.; Du, P.; Chen, L. X. *J. Am. Chem. Soc.* **2012,** 134, (40), 16472-16475.

9. Acharya, K. P.; Khnayzer, R. S.; O'Connor, T.; Diederich, G.; Kirsanova, M.; Klinkova, A.; Roth, D.; Kinder, E.; Imboden, M.; Zamkov, M. *Nano Lett.* **2011,** 11, (7), 2919-2926.

10. Khon, E.; Lambright, K.; Khnayzer, R. S.; Moroz, P.; Perera, D.; Butaeva, E.; Lambright, S.; Castellano, F. N.; Zamkov, M. *Nano Lett.* **2013,** 13, (5), 2016-23.

11. Amirav, L.; Alivisatos, A. P. *J. Phys. Chem. Lett.* **2010,** 1, (7), 1051-1054.

12. Huynh, W. U.; Dittmer, J. J.; Alivisatos, A. P. *Science* **2002,** 295, (5564), 2425-2427.

13. Giblin, J.; Kuno, M. *J. Phys. Chem. Lett.* **2010,** 1, (23), 3340-3348.

14. Talapin, D. V.; Nelson, J. H.; Shevchenko, E. V.; Aloni, S.; Sadtler, B.; Alivisatos, A. P. *Nano Lett.* **2007,** 7, (10), 2951-2959.

15. Fiore, A.; Mastria, R.; Lupo, M. G.; Lanzani, G.; Giannini, C.; Carlino, E.; Morello, G.; De Giorgi, M.; Li, Y.; Cingolani, R.; Manna, L. *J. Am. Chem. Soc.* **2009,** 131, (6), 2274-2282.

16. Nghia, N. X.; Hai, L. B.; Luyen, N. T.; Nga, P. T.; Lieu, N. T. T.; Phan, T.-L. *J. Phys. Chem. C* **2012,** 116, (48), 25517-25524.

17. Peng, Z. A.; Peng, X. *J. Am. Chem. Soc.* **2002,** 124, (13), 3343-3353.

18. Manna, L.; Milliron, D. J.; Meisel, A.; Scher, E. C.; Alivisatos, A. P. *Nat. Mater.* **2003,** 2, (6), 382-385.

19. Tari, D.; De Giorgi, M.; Della Sala, F.; Carbone, L.; Krahne, R.; Manna, L.; Cingolani, R.; Kudera, S.; Parak, W. J. *Appl. Phys. Lett.* **2005,** 87, (22), 224101-3.

20. Malkmus, S.; Kudera, S.; Manna, L.; Parak, W. J.; Braun, M. *J. Phys. Chem. B* **2006,** 110, (35), 17334-17338.

21. Wei, S.-H.; Zhang, S. B. *Phys. Rev. B* **2000,** 62, (11), 6944-6947.

22. Li, J.; Wang. *Nano Lett.* **2003,** 3, (10), 1357-1363.

23. Klimov, V. I.; Mikhailovsky, A. A.; McBranch, D. W.; Leatherdale, C. A.; Bawendi, M. G. *Science* **2000,** 287, (5455), 1011-1013.

24. Wu, K.; Zhu, H.; Liu, Z.; Rodríguez-Córdoba, W.; Lian, T. *J. Am. Chem. Soc.* **2012,** 134, (25), 10337-10340.

25. Klimov, V. I.; McBranch, D. W. *Phys. Rev. Lett.* **1998,** 80, (18), 4028-4031.

26. Pandey, A.; Guyot-Sionnest, P. *Science* **2008,** 322, (5903), 929-932.

27. Saunders, A. E.; Ghezelbash, A.; Sood, P.; Korgel, B. A. *Langmuir* **2008,** 24, (16), 9043-9049.

28. Wei, H. H.-Y.; Evans, C. M.; Swartz, B. D.; Neukirch, A. J.; Young, J.; Prezhdo, O. V.; Krauss, T. D. *Nano Lett.* **2012,** 12, (9), 4465-4471.

29. Wu, K.; Rodríguez-Córdoba, W. E.; Liu, Z.; Zhu, H.; Lian, T. *ACS Nano* **2013**.

30. Shabaev, A.; Efros, A. L. *Nano Lett.* **2004,** 4, (10), 1821-1825.

31. Mauser, C.; Da Como, E.; Baldauf, J.; Rogach, A. L.; Huang, J.; Talapin, D. V.; Feldmann, J. *Phys. Rev. B* **2010,** 82, (8), 081306.

32. She, C.; Bryant, G. W.; Demortière, A.; Shevchenko, E. V.; Pelton, M. *Phys. Rev. B* **2013,** 87, (15), 155427.

33. Brus, L. *J. Chem. Phys.* **1984,** 80, (9), 4403.

34. Huang, J.; Huang, Z. Q.; Yang, Y.; Zhu, H. M.; Lian, T. Q. *J. Am. Chem. Soc.* **2010,** 132, (13), 4858-4864.

Appendix 1.

Estimation of electron and hole confinement energy in CdSe tetrapods.

The band gap of a quantum confined nanocrystal can be written as:

$$E_g(QC) = E_g(bulk) + E_k + E_{e-h} \qquad (1)$$

where $E_g(QC)$ is the bandgap of the quantum confined component that can be determined by absorption spectrum, $E_g(bulk)$ is the band gap for bulk materials, $E_k$is the confinement energy, and E_{e-h} is the electron and hole Coulomb attraction energy. The CdSe bulk band gap, $E_g(bulk)$, is 1.74 for zinc blend structure and 1.799 for wurtzite structure. To estimate the confinement energy of the core and branch in TPs, we need to calculate the electron and hole Coulomb attraction energy. To simplify the calculation, we can assume a spherical confinement for the core, and the Coulomb attraction between the electron and hole at the lowest states can be approximated as[33]

$$E_{e-h} \approx -1.786 \frac{e^2}{\varepsilon_{CdSe} r} \qquad (2)$$

where r is the radius of the core, and ε_{CdSe} is the dielectric constant of CdSe (ε_{CdSe} =10). Assuming that the diameter of the core is the same as the diameter of the branch, r=1.2±2 nm, Coulomb energy can thus be estimated as -132 meV according to eq 2.

In the 1D confined branch, the electron-hole Coulomb attraction can be written as[30]

$$E_{e-h} \approx -\frac{e^2}{\varepsilon' \rho} \qquad (3)$$

where ρ is the effective screening length that 0.7 of the branch radius (1.2±0.2 nm), and ε' is the dielectric constant of dispersion medium (for chloroform, ε' = 4.81). Then the Coulomb energy

can be calculated as -356 meV. If we assign the low energy transition (T1 at 2.07 eV) to the band gap transition in the core and the high-energy transition (T2 at 2.17 eV) to the band gap transition in the branch, according to eq (1), the confinement energy in the core and branch can then be estimated as 547 and 732 meV, respectively. Since the effective mass of electron and hole is $0.13m_0$ and $0.45m_0$ where m_0 is mass of free electron, the confinement energy of the hole will be 123 and 164 meV in the core and branch. For the bulk materials, the valence band of wurtzite structure is 35 meV higher than that of zinc blend structure, the valence band edge of the branch is going to be 6 meV higher than that of the core in the CdSe tetrapods.

Appendix 2.

Interfacial electron transfer from CdSe tetrapod to molecular electron acceptor

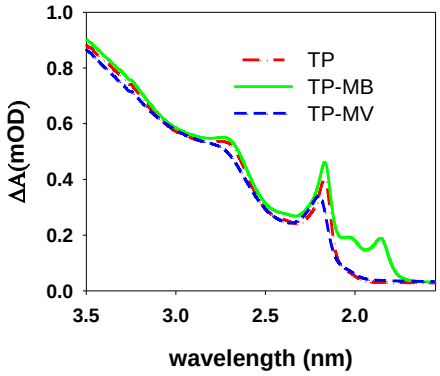

Figure A.7.1. The absorption spectra of CdSeTP, TP-methylene blue (MB^+) complex, and TP-methyl viologen (MV^{2+}) complex. The MB^+ and MV^{2+} were reported as efficient electron acceptors for many QDs.[5, 34]

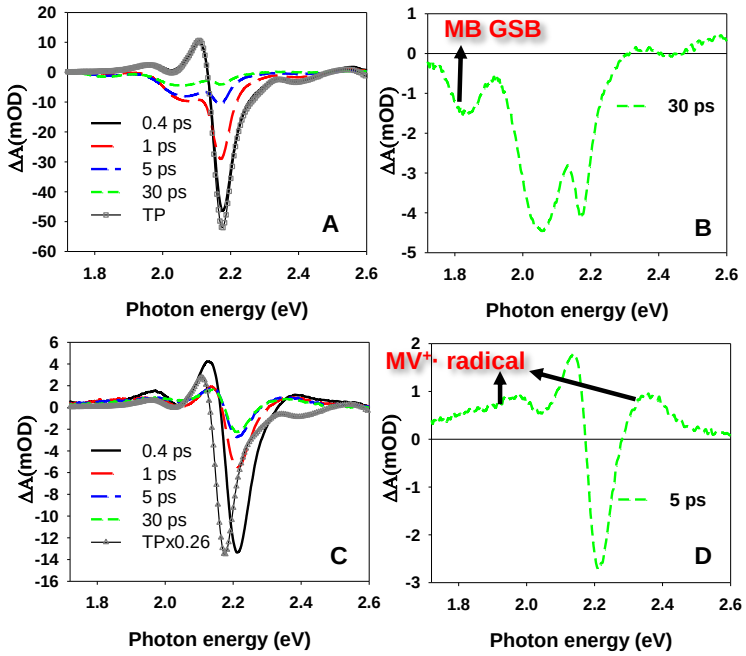

Figure A.7.2. The TA absorption spectra of (A) TP-MB^+ and (C) TP-MV^{2+} complex. Also shown in panel A and B are the CdSe TP absorption spectra recorded at 0.4 ps under the same excitation intensity (19 nJ/pulse). The expanded view of the TA recorded at 30 ps for (B) TP-MB^+ and (D) TP-MV^{2+}.

Compared with free TPs, TP-MB^+ complex has an additional absorption band centering at 1.86 eV that is assigned to the ground state abruption band of methylene blue (Figure A.7.1). In this figure we also find that the T2 transition is blue shifted by 30 meV probably due to the electronic coupling between MV^{2+} and TP. As shown in Figure A.7.2, the T1 and T2 bleach undergo fast recoveries in the presence of MB^+ and MV^{2+}, accompanied by the formation of MB ground state bleach (MB GSB) and absorption of methyl viologen radical ($MV^{+}\cdot$) suggest the electron transfer from TP to the adsorbed molecules. The TA spectrum of the free TP measured under the same excitation condition is also compared in these two figures. For TP-MB^+, the fully formed MB GSB at 30 ps suggests the completion of the electron transfer, but the T1 and T2 bleach does not completely recover by this delay time. The remaining bleach signals are possibly

caused by the free TPs in the mixture solution, and further investigation is ongoing. For TP-MV^{2+}, the absorption of $MV^{+}\cdot$ is fully formed after 5 ps. The T1 and T2 bleach completely recover by this delay time, and remaining TA absorption resembles the derivative of the absorption spectrum, which has been assign to the charge separated states.[3, 24] In sum, the full recovery of the T1 and T2 bleach as consequence of the electron transfer suggests that T1 and T2 bleach is caused the state filling of the CB1 and CB2 in the conduction band.

Appendix 3.

Abbreviations. CdSe, cadmium selenide; TP, tetrapod; 2P-TA, two pulse transient absorption; 3P-TA, three pulse transient absorption; PL, photoluminescence; CB, conduction band; VB, valence band; CB1, the first electron state in conduction band; CB2, the second electron state in conduction band; VB1, the first hole state in valence band.

Chapter 8. Bulk Transport and Interfacial Transfer Dynamics of Photogenerated Carriers in CdSe Quantum Dot Solid Electrodes

http://pubs.acs.org/doi/pdf/10.1021/nl401573x

8.1. Introduction.

In recent years, semiconductor quantum dots (QDs) has been investigated intensely as a light harvesting material for solar-driven hydrogen production.[1-11] Comparing with conventional molecular chromophores, QDs possess many superior properties, including tunable absorption spectra, large extinction coefficients in the visible-to-near IR range, long exciton lifetimes, fast electron transfer rates, and capability of multiple electron delivery.[3, 12] However, so far, most of the reported solar-to-H_2 generation studies involve half reactions ($2H^+ + 2e^- \rightarrow H_2$) in solutions, in which the electrons are provided by sacrificial electron donors. One way to eliminate sacrificial electron donor is to connect the water reduction components with water oxidation electrodes in full water splitting devices, with the latter providing the protons and electrons needed for the reduction half of the cell. Inspired by QD sensitized polymer film electrodes[13] and the emerging QD-solid based solar cells,[14-18] photoelectro-chemical cells,[19] and photo detectors,[20, 21] we are exploring QD solids as photoelectrodes for light-driven hydrogen generation. These QD solid electrodes can exhibit high photoconductivity due to strong coupling between adjacent QDs,[22-25] while maintaining the size dependent characteristics arising from quantum confinement in individual QDs.

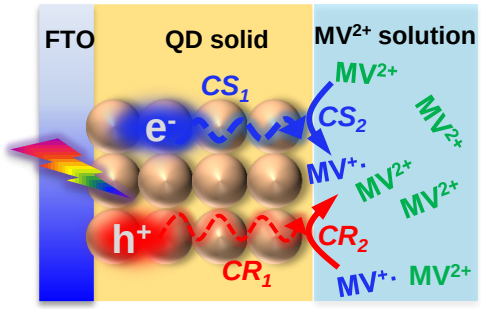

Figure 8.1. Schematic illustration of the charge carrier transport in QD solids (CS1 and CR1) and interfacial transfer at the surface (CS2 and CR2).

In this report, we investigated the dynamics of charge transport and interfacial charge transfer of CdSe QD solid electrodes immersed in aqueous solution of methyl viologen (MV^{2+}) by transient absorption (TA) spectroscopy. As shown in Figure 8.1, photogenerated electrons in the solid were transported through the QDs (denoted as CS1) before reaching the surface to reduce MV^{2+} (denoted as CS2), which competes with efficiency-limiting electron-hole recombination processes in the bulk.[26] Similarly, photogenerated holes also migrated to the surface (denoted as CR1) before recombining (denoted as CR2) with the electron in the reduced MV^{2+}. The interfacial charge transfer (CS2 and CR2) rates were determined by examining isolated CdSe QD-MV^{2+} complexes in solution. For QD solids immersed in MV^{2+} solution, by monitoring the 1S exciton bleach of the solid and the absorption of reduced MV^{2+}, we determined the electron and hole transport (CS1 and CR1) rates in the solid. We showed that all photogenerated electrons could reduce MV^{2+} prior to recombination with the hole, suggesting the feasibility of using such electrodes in photoelectrochemical cells. The film thickness dependence of the electron transport rates were shown to be well described by diffusion controlled electron transport within the QD solid.

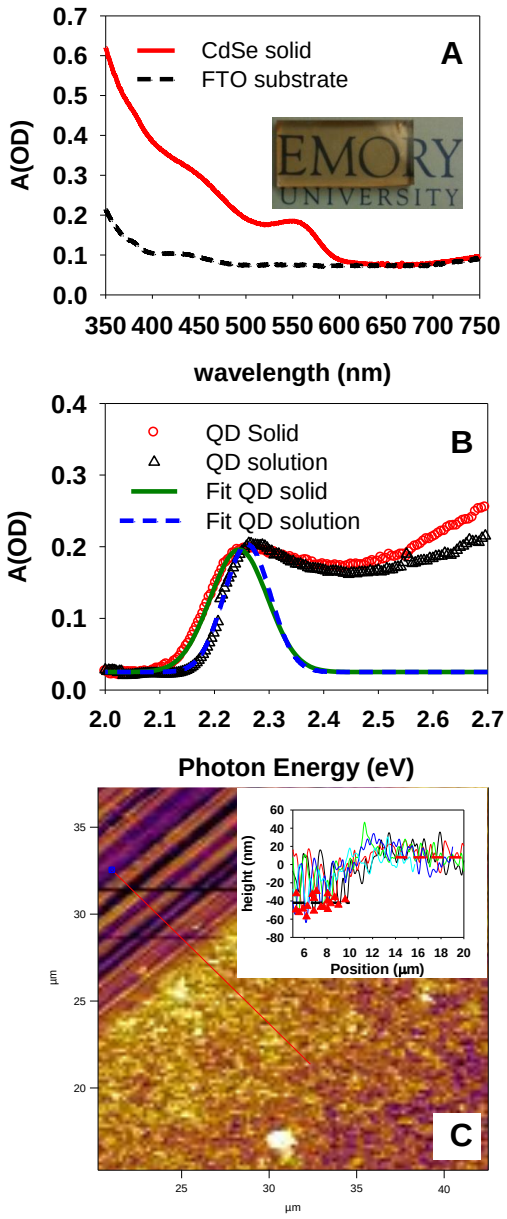

Figure 8.2. (A) UV-Vis absorption spectra of a CdSe QD solid (red solid line) and the FTO substrate (black dashed line). Inset is a photograph of the QD solid. (B) Comparison of the 1S exciton absorption bands between the QD solid (red circle) and QD solution (black triangle). The spectrum of the QD solid is obtained by subtracting FTO substrate absorption from the total absorption. Also shown are Gaussian fits of 1S exciton band of the QD solid (green dashed line) and QD solution (blue solid line). (C) Atomic force micrograph of a CdSe QD solid film. The top

corner has been scratched to expose the substrate. Inset shows height profile corresponding to the red line in the AFM image. The red dashed line represents the average heights of the unscratched region. The red triangles represent the lowest points in the scratched region and the black dashed line indicates the average heights of these points.

8.2. Results and discussions.

8.2.1. Absorption spectrum, exciton band broadening and solid thickness.

CdSe QD solids were prepared by layer-by-layer spin coating using ethanedithiol as cross-linking molecules. All solids were annealed at 120 ºC in air for 30 minutes before use. A more detailed procedure is described in the Chapter 2. Figure 8.2A shows the UV-Vis absorption spectrum of a QD solid sample used for TA study. A prominent 1S exciton absorption band centering at 551 nm can be observed, indicating the preservation of quantum confinement in the QD solid. Also plotted is the absorption spectrum of the substrate, FTO glass, showing a strong absorption in UV region and weak broad absorption beyond 650 nm. A photograph of the QD solid is shown in the inset, demonstrating high homogeneity of film. As shown in Figure 8.1 B, the 1S exciton absorption bands of the QD solid and the QD solution are fit by Gaussian functions. The best fit reveals that, compared with QD solution, the 1S exciton peak of the QD solid was broadened by 21 meV (ΔFWHM~21 meV) and red-shifted by ~13 meV. This spectral broadening and red-shifting have been attributed to 1S electron state delocalization caused by strong electronic coupling between adjacent dots.[22, 27, 28] The diameter of the QDs is estimated to be ~3.0 nm according to an empirical relationship between the wavelength of the first excitonic peak (548nm) and particle size for QDs in solution.[29, 30] The atomic force micrograph (AFM) of the CdSe QD solid on FTO is shown in Figure 8.2 C. Since the solid was purposely scratched, the

thickness of the QD solid is the height difference between QD solid surface and FTO surface that was exposed on the scratched areas. The height profile corresponding to the red line across the scratched and unscratched area shows a thickness of 50±6 nm.

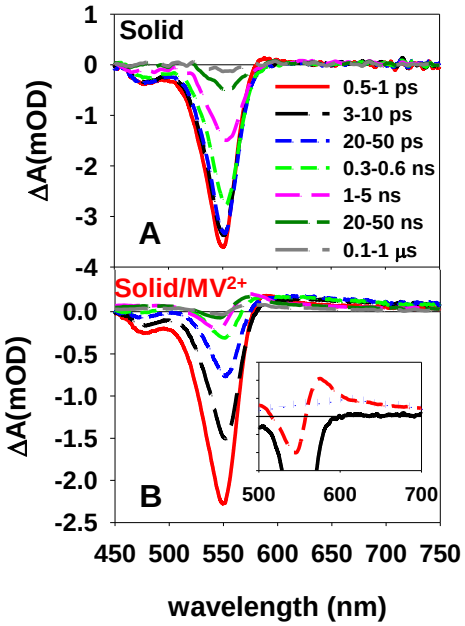

Figure 8.3. Transient absorption spectra of CdSe solid in water containing 0 mM (A) and 25 mM (B) of MV^{2+} at indicated delay times after 400 nm excitation. (Inset) Expanded view of averaged TA spectra of Solid (black solid line) and Solid/MV^{2+} (red dashed line) from 1 to 5 ns . Also shown for comparison in the inset is a $MV^{+}\cdot$ radical absorption spectrum (blue dotted line).

8.2.2. TA measurements of QD solid and QD solid in MV^{2+} solution.

We first investigated carrier dynamics in QD solids immersed in water in the absence of MV^{2+}(referred to as Solid hereafter) by transient absorption spectroscopy. The details of the

femtosecond and nanosecond spectrometers used for this study are provided in the supporting information. As shown in Fig 8.3 A, their TA spectra measured with 400 nm excitation show a long lived 1S exciton bleach that completely recovers after 1 μs. It has been shown that the 1S exciton bleach signal in CdSe QDs can be attributed to the state-filling of the 1S electron level, which provides a convenient probe of 1S electron dynamics.[31, 32] Figure 8.3 B shows the transient spectra of a CdSe solid electrode immersed in an aqueous solution of MV^{2+} with a concentration of 25 mM (Solid/MV^{2+}). An expanded view of Solid/MV^{2+} TA spectrum (at 1-5 ns) is shown in Figure 8.3 B inset along with a comparison with $MV^{+}\cdot$ radical absorption spectrum and the TA spectrum for Solid (at 1-5 ns). Compared to CdSe solid in water, the 1S exciton bleach undergoes a much faster recovery, indicating short-lived 1S electrons. Simultaneously, a broad methyl viologen radical ($MV^{+\cdot}$) absorption band appears from ~600 - 750 nm, indicating electron transfer from QDs to MV^{2+}.[33-35] After 1 ns, the TA signal in the exciton bleach region evolves into derivative of the absorption spectrum, which can be attributed the Stark effect induced shift of QD exciton bands in charge separated state.[34] All these spectral features (bleach recovery, $MV^{+\cdot}$ absorption and Stark effect signal) confirm electron transfer from the QD solid to MV^{2+} molecules.

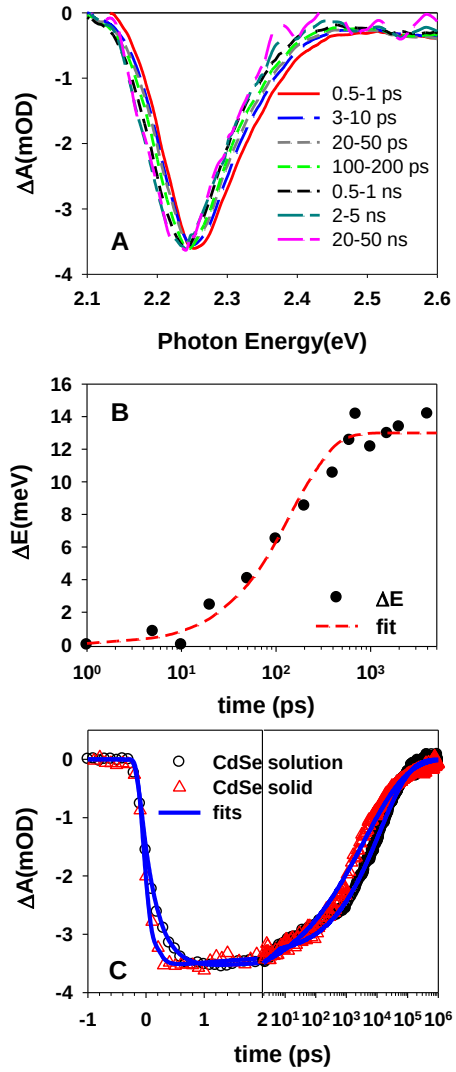

Figure 8.4. (A) Comparison of normalized 1S exciton bleach spectra of Solid in water. The 1S exciton bleach signals at indicated delay times are normalized to that at 0.5-1 ps. (B) 1S exciton peak shifting as a function of time (full circles) in Solid and its fit to a single exponential function (red dashed line). ΔE represents the 1S exciton peak shifting since 1ps. The best single exponential fit yields a half-life of 102±18 ps. (C) Comparison of the 1S exciton bleach kinetics of Solid and QD solution. The x-axis was in linear scale at -1 to 2 ps and in logarithmic scale at 2-1000 ns. The blue solid lines stretched exponential fits.

Figure 8.4 A shows that the peak of the 1S exciton bleach shifts to lower energy with increasing delay time until ~2 ns for Solid, which was not observed for free QDs. This time dependent exciton peak shift in QD solids can be attributed to hopping of electrons or excitons to larger QDs.[27] As shown in Figure 8.4 B, the 1S exciton bleach peak shifting is plotted as function of time and fit by a single exponential function that reveals a half-life of 102±18 ps. The kinetics of 1S bleach formation and decay in QD solids and free QDs are compared in Figure 8.4 C. The kinetics in the QD solid was obtained by averaging the TA signal from 2.27 to 2.23 eV to eliminate the influence of peak shifting. The fit of the kinetics shows that the half-life of the bleach formation is 90±17 fs and 208±7 fs in QD solids and free QD solution, respectively, indicating a faster hot electron relaxation from the initially excited level to the 1S electron level in the QD solid. A similar phenomenon has been observed in PbS QD solids and have been attributed to enhanced phonon assisted thermalization caused by strong electronic coupling between QDs.[27] The bleach decay can be fitted by stretched exponential functions, with a half-life of 1.2±0.1 and 5.4±0.2 ns in the QD solid and free QDs, respectively, indicating long lived 1S electrons in both materials.

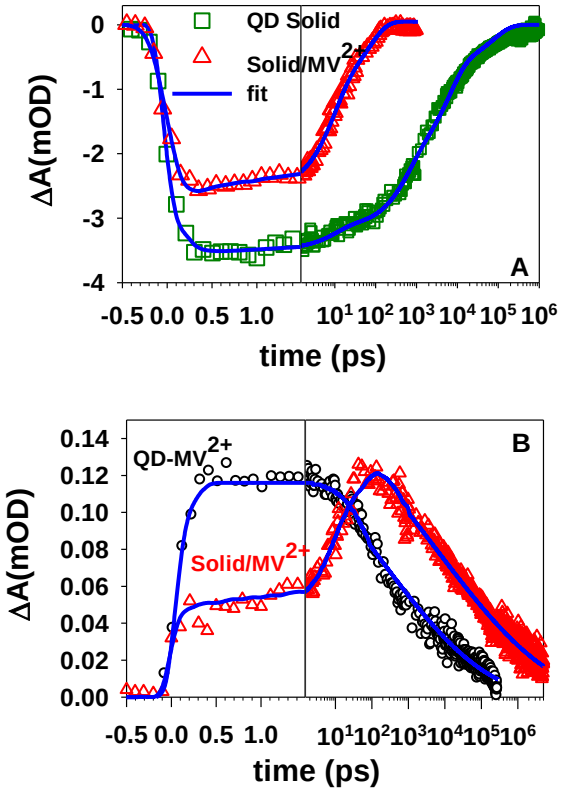

Figure 8.5. (A) 1S exciton bleach kinetics (at 548 nm) of the CdSe electrode in water containing 0 mM (green squares) and 25 mM (red triangles) of MV^{2+}. (B) Comparison of $MV^{+\cdot}$ radical formation and decay kinetics in CdSe solid/MV^{2+} (red triangles) and CdSe-MV^{2+} complexes in solution (black circle). The solid blues line in panel A and B are fits to the data (see SI for details).

The kinetic traces of the 1S exciton bleach of Solid and Solid/MV^{2+} are compared in Figure 8.5 A. In addition to a faster recovery rate, the initial amplitude of the exciton bleach for Solid/MV^{2+} is only 70% of that for Solid at early delay time, indicating an ultrafast (<<150 fs, the instrument response time) ET component.[33, 36] Such biphasic electron transfer process and the ultrafast ET component can be more clearly seen in the formation kinetics of methyl viologen radical ($MV^{+\cdot}$) monitored at 630 to 650 nm (Figure 8.5 B). This spectral range, on the longer

wavelength side of the $MV^{+\cdot}$ absorption band (centered at 605 nm), has been chosen to avoid the contributions from the much stronger QD exciton bands. In comparison, free QD solids show only a small photoinduced absorption (PA) signal of the hole in the same spectral region(Figure 8.3).[37] Fitting the $MV^{+\cdot}$ radical bi-phasic growth kinetics yield an instantaneous formation (with a rise time of 64±42 fs) and a relatively slower multiple exponential growth with a half lifetime of 12±3 ps. After subtracting the contribution from QD PA signal, the amplitude of the instantaneous $MV^{+\cdot}$ growth component is estimated to be 30% of the total amplitude, which is consistent the amplitude of the ultrafast component of the 1S exciton bleach recovery. Furthermore, the kinetics of 1S bleach recovery and $MV^{+\cdot}$ formation also shows excellent agreement. As shown in Figure 8.5 A, the 1S exciton bleach recovery kinetics can also be well fit by the same parameters for the fit of $MV^{+\cdot}$ radical formation kinetics. We attribute the nearly instantaneous and slower MV^{2+} reduction processes to the transfer of electrons from QDs on the electrode surface (with an interfacial electron transfer rate CS2), and in the bulk (with an overall transfer rates controlled by internal transport, CS1), respectively, as depicted in Figure 8.1.

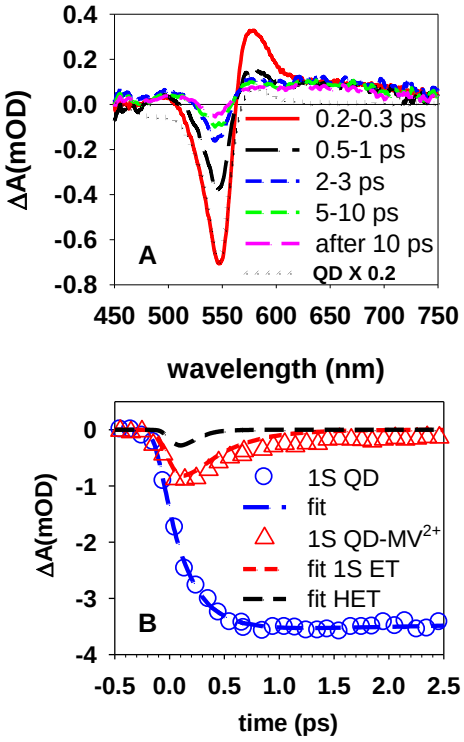

Figure 8.6. (A) Transient absorption spectra of CdSe-MV^{2+} complexes in solution at indicated delay times after 400 nm excitation. The TA spectrum of free QDs in solution (at 0.2-0.3 ps), which has been scaled by a factor of 0.2, is also plotted on for comparison. The experimental conditions and QD concentrations are the same for the QD-MV^{2+} complexes and free QDs. (B) Comparison of 1S bleach recovery kinetics of free QDs (open circles) and QD-MV^{2+} complexes (open triangles) at early delay times. The blue long-dash line is a fit of the 1S bleach formation of the free QDs. The red short-dash and black medium-dash lines are fits to the 1S bleach recovery kinetics of QD-MV^{2+} complexes according to eqs 8.1 and 8.2, respectively.

8.2.3. Electron transfer to MV^{2+}: Hot electron transfer model vs. 1S electron transfer model.

To support the above assignment, we also investigated electron transfer in CdSe-MV^{2+} complexes in chloroform. This system, in which all MV^{2+} molecules are believed to be bound to the QD due to the negligible solubility of MV^{2+} in chloroform, should serve as a model for interfacial ET from QDs on the surface of the QD Solid to adsorbed MV^{2+}. The ratio of MV^{2+} to QD was determined to be 9 from the absorbance of the QD and MV^{2+} in the complex. As shown in Figure 8.6 A, at 0.2-0.3 ps, the amplitude of QD 1S exciton bleach for CdSe-MV^{2+} complexes is only 20% of that for free the QDs at the same delay time, and the broad $MV^{+}\cdot$ radical absorption has already formed, suggesting either ultrafast ET from the 1S electron level and/or ET from 1P and higher energy level. This can be more readily seen in Figure 8.6 B, in which the 1S exciton bleach formation and decay kinetics of free QDs and QD-MV^{2+} complexes are compared. Also shown in this figure are fits according to two electron transfer model. In the first model, we assume that the hot electrons generated by 400 nm excitation relax to 1S level prior to transfer to the adsorbate. According to this model, the 1S bleach (A_{1S}) amplitude, which is proportional to the 1S electron population, can be described by the following equation

$$A_{1S}(t) = A_0 \frac{k_1}{k_2 - k_1}\left(e^{-k_1 t} - e^{-k_2 t}\right) \qquad (8.1)$$

where A_0 is the maximum 1S bleach amplitude if all excited electrons relax to the 1S level, k_1 the hot electron cooling rate to the 1S level, and k_2 the transfer rate from the 1S level to the adsorbate. A_0 and k_1 can be determined from the maximum 1S exciton bleach amplitude and its formation time, respectively, in free QDs (Figure 4B). $1/k_2$ is determined to be 107±12 fs by fitting the $MV^{+}\cdot$ radical formation kinetics (Figure 8.5 B). As shown in Figure 8.6 B, this model, which contains no adjustable parameters, fits the 1S exciton bleach recovery kinetics well. In this fit, we ignore the contribution of charge separated state signal to the 1S exciton, which accounts the small discrepancy between the fit and the data.

In the second model, we assume ET can also occur from the 1P level (with rate constant k_3), which competes with hot electron relaxation to the 1S level. In this case, the 1S bleach decay is given by

$$A_{1S}(t) = A_0 \frac{k_1}{k_2 - k_1 - k_3}\left(e^{-(k_1+k_3)t} - e^{-k_2 t}\right) \qquad (8.2)$$

This model predicts a smaller amplitude and faster formation and recovery of 1S bleach, which leads poorer agreement with the experimental data. As an illustration, the predicted kinetics of 1S bleach calculated assuming similar ET rates from the 1S and 1P level (k_3~k_2) is also shown in Figure 8.6B, which deviates significantly from the experimental data and indicates that most of the electrons are transferred from the 1S level of QDs.

8.2.3. Electron and hole transport and interfacial transfer rate in Solid/MV^{2+}.

For QD solid in the aqueous solution of MV^{2+}, the average number of adsorbed MV^{2+} on the surface QDs have been determined to be 38 by measuring the absorption spectra before and after soaking the QD solid in MV^{2+} solution. Because ET rates have been shown to be proportional to the number of adsorbed electron acceptors, we can expect that ET from the surface QDs to MV^{2+} in the QD solid is ~4 times faster than the ET in isolated QD/MV^{2+} complexes in solution, which is consistent with nearly instantaneous formation (64±42fs) of $MV^{+\bullet}$ shown in Figure 8.5 B.

Table 8.1. Half lifetimes of charge carrier transport in the solid and charge transfer at the surface**.**

	CS2(fs)*	*CS1*(ps)*	*CR2*(ns)*	*CR1*(ns)*

Solid/MV^{2+}	< 64±42	12±2	0.36±0.03**	200±10
QD-MV^{2+}	74±8	NA	0.36±0.03	NA

*These half lifetimes are calculated from the fitting parameters shown in SI.

** CR2 is assumed to be the same as charge recombination time in QD-MV^{2+} complexes in solution.

The kinetics of $MV^{+\cdot}$ radical formation and decay in Solid/MV^{2+} and QD-MV^{2+} complexes are compared in Figure 8.5 B. These kinetics are fit by multiple exponential functions, and the half lifetimes of the charge separation and recombination are summarized in Table 1. In these experiments, the concentration of QDs in QD-MV^{2+} was adjusted so that the same amount of QDs was excited as in Solid/MV^{2+}, which was verified by the amplitudes of the 1S exciton bleach in these two systems in the absence of MV^{2+}. Since MV^{2+} has no absorption at excitation wavelength (400 nm), addition of these molecules cannot affect the number of the excited QDs. The comparison shows that the same amounts of $MV^{+\cdot}$ radicals were formed in Solid/MV^{2+} and QD-MV^{2+} despite the slower transport-limited photoreduction process in the former. The transient quantum yield of $MV^{+\cdot}$ formation can be assumed to be 100% because of much faster ET rate compared to 1S exciton lifetime in both systems. Compared with QD-MV^{2+}, the decay of $MV^{+\cdot}$ absorption in Solid/MV^{2+} is ~ 500 times slower, which can be attributed to slow hole transport in the solid (CR1).

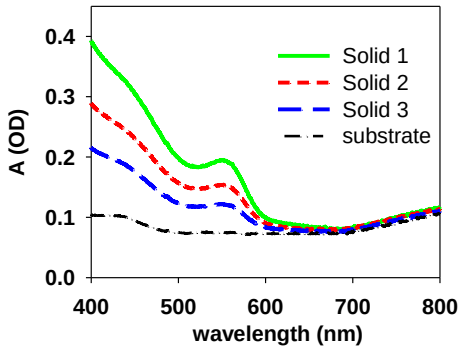

Figure 8.7. UV-Vis absorption spectra of the QD solids with various thicknesses.

8.2.3. QD solid thickness dependent electron transport rate.

To further support the proposed assignment and to understand the mechanism of electron transport, we examined its dependence on the film thickness. As shown in Figure 8.7, the absorption spectra of two solids (Solid 2 and 3) with less thickness are compared with the solid studied above (Solid 1). The total thickness of the Solid 1 was estimated to be 50±6 nm (Figure 8.2 C), and the thicknesses of the thinner solids were determined by their relative optical density to Solid 1. The TA measurement of these samples in water and MV^{2+} solution were carried out under the same excitation conditions. The initial 1S exciton bleach signals ($\Delta 1S_{max}$) are listed in Table 8.2. As discussed above, the ratio between the initial 1S bleach amplitude of the solid in these two different environments indicates the fraction of QDs in the bulk and on the surface. Indeed, in thinner films, the relative amplitude of instantaneous bleach recovery component increases, reflecting that larger percentages of QDs can be accessed by MV^{2+} in solution. The initial amplitude of the slow component reflects the percentage of QDs that are in the bulk (without direct access to MV^{2+}). Thus we estimate the effective bulk thickness (i.e. the transport distance) L, by scaling the total film thickness by the fraction of the QDs in the bulk. This scaling accounts for the nanoporous nature of the film. For example, Solid 1 (film thickness of 50±6 nm)

is estimated to have ~ 17 layers of QDs. If the films are not nanoporous, only the 6 % of the QDs (the outmost layer) have direct access to MV^{2+}, which is much smaller than the 30% surface QDs estimated from the initial amplitude of the 1S exciton bleach recovery kinetics. All these measurements and the estimated effective thicknesses are listed in Table 8.2.

Table 8.2. Transport distances in three QD solids.

	Solid 1	Solid 2	Solid 2
1S absorption (mOD)	120	79	47
Solid thickness (nm)	50±6[a]	33±4	19±1
$\Delta 1S_{max}$ solid/water (mOD)	3.7	2.8	1.8
$\Delta 1S_{max}$ solid/MV^{2+} (mOD)	2.6	1.8	0.9
Fraction of the QDs in the bulk	70%	64%	50%
Transport distance L (nm)	35±4[a]	21±2	10±1

[a]From AFM measurement.

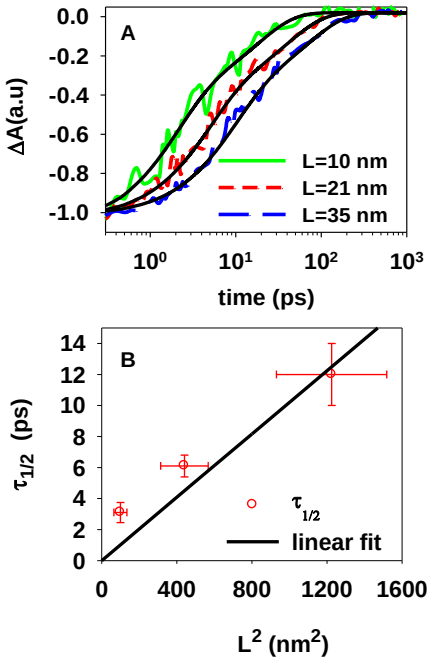

Figure 8.8. (A) Normalized comparison of 1S exciton bleach recovery kinetics of CdSe Solid/MV^{2+} sample of different film thickness. L is the electron transport distance, approximated as the thickness of the bulk of the solid. The black solid lines are bi-exponential fits. (B) Half lifetime of 1S bleach recovery (open circles) as a function of L^2, a linear fit (black line).

In Figure 8.8 A, we compare the 1S exciton bleach recoveries of QD Solids/MV^{2+} samples of different thicknesses. These kinetics have been normalized to the same amplitude at the early delay time and fit by bi-exponential functions. It shows slower ET rates in thicker films. The same trend is observed in the $MV^{+\bullet}$ radical formation kinetics (not shown), although these data have much lower signal-to-noise ratios. Due to the low dark charge carrier density in CdSe QD solids,[22] we can assume that the band bending of the solid in MV^{2+} solution is small and electron transport is controlled by diffusion. By solving the electron diffusion equation as described in Appendix 1, the theoretical prediction of the kinetics of 1S exciton bleach signal (i.e. the total electron population in the bulk) is given by

$$\Delta A(t) \approx \frac{16\alpha N_0 L}{\pi^2} e^{-D_0\left(\frac{\pi}{2L}\right)^2 t} \quad (8.3)$$

where α is absorption coefficient of QD at 1S exciton peak, N_0 the initial electron concentration in the solid , L the electron transport distance, D_0 electron diffusion coefficient. According to this model, the half lifetime of the 1S exciton bleach kinetics, $t_{1/2}$, is proportional to the square of the film thickness L^2, $t_{1/2}=(4\ln 2/\pi^2)\cdot(L^2/D_0)$. As shown in Figure 8.8 B, the half lifetime of exciton bleach recovery increases linearly with L^2, consistent with the diffusion control transport model. The diffusion coefficient of electron in the solid can also be determined from the slope of the linear fit, $D_0=(2.3\pm0.8)\times10^{-5}$ m^2s^{-1}. The electron mobility, μ, can be estimated from the Einstein–Smoluchowski relation $\mu=qD_o/K_bT$, where q is electron charge, K_b is Boltzmann constant, and T is the absolute temperature.[24, 38, 39] At T=298K, this relation gives an electron mobility of CdSe QD solid, $\mu=9.1\pm2.9$ $cm^2s^{-1}V^{-1}$, which is in the upper limit of values determined by field-effect transistor or photoconductivity ($\mu=$ 10^{-4}-10^{1} $cm^2s^{-1}V^{-1}$) measurements.[22, 24, 40-43] One possible source of error is the uncertainty in the determination of effective thickness of the nanoporous films. Further systematic studies on the dependence of the measured mobilities on film preparation conditions (such as capping ligand and annealing temperature) and direct comparison with electrical measurements would be needed to investigate whether the TA method described here is a useful way for measuring carrier mobilities in QD solid electrodes.

Our findings suggest that QD solid electrodes could be used as the active component of excitonic solar cells, in which the current is driven by gradient of electron concentration resulting from interfacial charge transfer.[18, 44] A recent study has reported that coating of multilayers of QDs in QD sensitized solar cells could improve the energy conversion efficiency, which is consistent with fast and efficient diffusion controlled charge separation process observed here.[26] The observed high mobility also suggests that these materials can also work as a component of a p-n or Schottchy junction solar cells, where current is driven by the built-in electric field.[15, 16, 45]

8.3. Conclusion.

In summary, the dynamics of charge transport and interfacial charge transfer of CdSe QD solid electrodes immersed in MV^{2+} solution has been examined by TA spectroscopy. Electron-hole pairs in the QD solid can be separated by electron transfer to MV^{2+} in solution with 100% quantum efficiency. For a 50 nm thick CdSe QD solid electrode, a bi-phasic MV^{2+} reduction process with an ultrafast interfacial transfer ($\tau_{1/2}$~64±42 fs, 30%) and a slower bulk-transport limited ($\tau_{1/2}$~12±2 ps, 70%) components were observed. Charge recombination with hole in the bulk of the solid ($\tau_{1/2}$~200±10 ns) was slowed down by hole transport in the solid. The film thickness dependent electron transfer rates can be described by a diffusion-controlled transport process. Both efficient charge separation and high carrier mobility suggests the potential applications of QD solids as photoelectrodes for solar-to-fuel conversion.

Reference

1. Han, Z.; Qiu, F.; Eisenberg, R.; Holland, P. L.; Krauss, T. D. *Science* **2012,** 338, (6112), 1321-1324.

2. Amirav, L.; Alivisatos, A. P. *J. Phys. Chem. Lett.* **2010,** 1, (7), 1051-1054.

3. Zhu, H.; Song, N.; Lv, H.; Hill, C. L.; Lian, T. *J. Am. Chem. Soc.* **2012,** 134, (28), 11701-11708.

4. Acharya, K. P.; Khnayzer, R. S.; O'Connor, T.; Diederich, G.; Kirsanova, M.; Klinkova, A.; Roth, D.; Kinder, E.; Imboden, M.; Zamkov, M. *Nano Lett.* **2011,** 11, (7), 2919-2926.

5. Huang, J.; Mulfort, K. L.; Du, P.; Chen, L. X. *J. Am. Chem. Soc*. **2012,** 134, (40), 16472-16475.

6. Tang, M. L.; Grauer, D. C.; Lassalle-Kaiser, B.; Yachandra, V. K.; Amirav, L.; Long, J. R.; Yano, J.; Alivisatos, A. P. *Angew. Chem., Int. Ed.* **2011,** 50, (43), 10203-10207.

7. Holmes, M. A.; Townsend, T. K.; Osterloh, F. E. *Chem. Commun.* **2012,** 48, (3), 371-373.

8. Brown, K. A.; Wilker, M. B.; Boehm, M.; Dukovic, G.; King, P. W. *J. Am. Chem. Soc.* **2012,** 134, (12), 5627-5636.

9. Wang, F.; Wang, W.-G.; Wang, X.-J.; Wang, H.-Y.; Tung, C.-H.; Wu, L.-Z. *Angew. Chem., Int. Ed.* **2011,** 50, (14), 3193-3197.

10. Brown, K. A.; Dayal, S.; Ai, X.; Rumbles, G.; King, P. W. *J. Am. Chem. Soc.* **2010,** 132, (28), 9672-9680.

11. Greene, B. L.; Joseph, C. A.; Maroney, M. J.; Dyer, R. B. *J. Am. Chem. Soc.* **2012,** 134, (27), 11108-11111.

12. Zhu, H.; Yang, Y.; Lian, T. *Acc. Chem. Res.* **2012**.

13. Shallcross, R. C.; D'Ambruoso, G. D.; Pyun, J.; Armstrong, N. R. *J. Am. Chem. Soc.* **2010,** 132, (8), 2622-2632.

14. Gur, I.; Fromer, N. A.; Geier, M. L.; Alivisatos, A. P. *Science* **2005,** 310, (5747), 462-465.

15. Luther, J. M.; Law, M.; Beard, M. C.; Song, Q.; Reese, M. O.; Ellingson, R. J.; Nozik, A. J. *Nano Lett.* **2008,** 8, (10), 3488-3492.

16. Pattantyus-Abraham, A. G.; Kramer, I. J.; Barkhouse, A. R.; Wang, X. H.; Konstantatos, G.; Debnath, R.; Levina, L.; Raabe, I.; Nazeeruddin, M. K.; Gratzel, M.; Sargent, E. H. *ACS Nano* **2010,** 4, (6), 3374-3380.

17. Semonin, O. E.; Luther, J. M.; Choi, S.; Chen, H.-Y.; Gao, J.; Nozik, A. J.; Beard, M. C. *Science* **2011,** 334, (6062), 1530-1533.

18. Choi, J. J.; Lim, Y.-F.; Santiago-Berrios, M. E. B.; Oh, M.; Hyun, B.-R.; Sun, L.; Bartnik, A. C.; Goedhart, A.; Malliaras, G. G.; Abruña, H. c. D.; Wise, F. W.; Hanrath, T. *Nano Lett.* **2009,** 9, (11), 3749-3755.

19. Nann, T.; Ibrahim, S. K.; Woi, P.-M.; Xu, S.; Ziegler, J.; Pickett, C. J. *Angew. Chem., Int. Ed.* **2010,** 49, (9), 1574-1577.

20. Sukhovatkin, V.; Hinds, S.; Brzozowski, L.; Sargent, E. H. *Science* **2009,** 324, (5934), 1542-1544.

21. Pal, B. N.; Robel, I.; Mohite, A.; Laocharoensuk, R.; Werder, D. J.; Klimov, V. I. *Adv. Funct. Mater*. **2012,** 22, (8), 1741-1748.

22. Choi, J.-H.; Fafarman, A. T.; Oh, S. J.; Ko, D.-K.; Kim, D. K.; Diroll, B. T.; Muramoto, S.; Gillen, J. G.; Murray, C. B.; Kagan, C. R. *Nano Lett.* **2012,** 12, (5), 2631-2638.

23. Talgorn, E.; Gao, Y.; Aerts, M.; Kunneman, L. T.; Schins, J. M.; Savenije, T. J.; van HuisMarijn, A.; van der ZantHerre, S. J.; Houtepen, A. J.; SiebbelesLaurens, D. A. *Nat Nano* **2011,** 6, (11), 733-739.

24. Lee, J.-S.; Kovalenko, M. V.; Huang, J.; Chung, D. S.; Talapin, D. V. *Nat Nano* **2011,** 6, (6), 348-352.

25. Liu, Y.; Gibbs, M.; Puthussery, J.; Gaik, S.; Ihly, R.; Hillhouse, H. W.; Law, M. *Nano Lett.* **2010,** 10, (5), 1960-1969.

26. Shalom, M.; Buhbut, S.; Tirosh, S.; Zaban, A. *J. Phys. Chem. Lett.* **2012,** 3, (17), 2436-2441.

27. Gao, Y.; Talgorn, E.; Aerts, M.; Trinh, M. T.; Schins, J. M.; Houtepen, A. J.; Siebbeles, L. D. A. *Nano Lett.* **2011**.

28. Williams, K. J.; Tisdale, W. A.; Leschkies, K. S.; Haugstad, G.; Norris, D. J.; Aydil, E. S.; Zhu, X. Y. *ACS Nano* **2009,** 3, (6), 1532-1538.

29. Yu, W. W.; Qu, L.; Guo, W.; Peng, X. *Chem. Mater*. **2003,** 15, (14), 2854-2860.

30. Jasieniak, J.; Smith, L.; Embden, J. v.; Mulvaney, P.; Califano, M. *J. Phys. Chem. C* **2009,** 113, (45), 19468-19474.

31. Klimov, V. I. *Annu. Rev. Phys. Chem.* **2007,** 58, 635-673.

32. Huang, J.; Stockwell, D.; Huang, Z.; Mohler, D. L.; Lian, T. *J. Am. Chem. Soc.* **2008,** 130, (17), 5632-5633.

33. Matylitsky, V. V.; Dworak, L.; Breus, V. V.; Basche, T.; Wachtveitl, J. *J. Am. Chem. Soc.* **2009,** 131, (7), 2424.

34. Zhu, H.; Song, N.; Rodríguez-Córdoba, W.; Lian, T. *J. Am. Chem. Soc.* **2012,** 134, (9), 4250-4257.

35. Watanabe, T.; Honda, K. *J. Phys. Chem.* **1982,** 86, (14), 2617-2619.

36. Yang, Y.; Rodríguez-Córdoba, W.; Lian, T. *J. Am. Chem. Soc.* **2011,** 133, (24), 9246-9249.

37. Huang, J.; Huang, Z.; Jin, S.; Lian, T. *J. Phys. Chem. C* **2008,** 112, (49), 19734-19738.

38. Einstein, A. *Annalen der Physik* **1905,** 322, (8), 549-560.

39. Yu, D.; Wang, C.; Guyot-Sionnest, P. *Science* **2003,** 300, (5623), 1277-1280.

40. Kang, M. S.; Sahu, A.; Norris, D. J.; Frisbie, C. D. *Nano Lett.* **2010,** 10, (9), 3727-3732.

41. Yu, D.; Wehrenberg, B. L.; Jha, P.; Ma, J.; Guyot-Sionnest, P. *J. Appl. Phys.* **2006,** 99, (10), 104315-7.

42. Talgorn, E.; Abellon, R. D.; Kooyman, P. J.; Piris, J.; Savenije, T. J.; Goossens, A.; Houtepen, A. J.; Siebbeles, L. D. A. *ACS Nano* **2010,** 4, (3), 1723-1731.

43. Talgorn, E.; Moysidou, E.; Abellon, R. D.; Savenije, T. J.; Goossens, A.; Houtepen, A. J.; Siebbeles, L. D. A. *J. Phys. Chem. C* **2010,** 114, (8), 3441-3447.

44. Gregg, B. A. *J. Phys. Chem. B* **2003,** 107, (20), 4688-4698.

45. Johnston, K. W.; Pattantyus-Abraham, A. G.; Clifford, J. P.; Myrskog, S. H.; Hoogland, S.; Shukla, H.; Klem, E. J. D.; Levina, L.; Sargent, E. H. *Appl. Phys. Lett.* **2008,** 92, (12), 122111-3.

Appendix 1

Diffusion-controlled electron transport model.

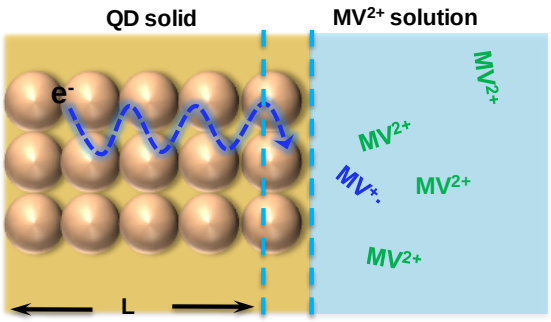

Figure A.8.1. Electron transport model for QD solid in MV^{2+} solution. *L* is the maximum electron transport distance.

In this model, we divide the QD solids into surface and bulk (with thickness *L*) regions. In the surface region, the QDs can interact directly with MV^{2+} in the solution, giving rise to ultrafast interfacial ET (with a time constant of 0.1 ps). Photogenerated electrons in the bulk can diffuse through the bulk onto surface, at which it is transferred to MV^{2+}. The electron distribution in the solid can be described by the diffusion equation

$$\frac{\partial N(x,t)}{\partial t} = D_0 \frac{\partial^2 N(x,t)}{\partial^2 x} \quad (1)$$

where D_0 is the diffusion coefficient of electrons in the solid. Because the optical density of the solid is small, we can assume that, the initial concentration of photogenerated electrons is constant over *L*, which gives the initial condition as

$$N(x, t = 0) = C_0 \quad (2)$$

Because the transient absorption measurement has shown that the electron transfer at interface was much faster than electron transport in the bulk, we can also assume that the electron concentration at surface of the solid is 0, which gives one boundary condition as

$$N(x=0,t)=0 \quad (3)$$

Since there is no electron transfer at the other end of the solid, it gives another boundary condition as

$$J(x=L,t)=0 \qquad or \qquad \frac{\partial N(x,t)}{\partial x}=0 \qquad (4)$$

Satisfied all these conditions, the diffusion equation can be solved by using Fourier series, and the solution is given by

$$N(x,t)=\sum_n C_n \sin\frac{n\pi x}{2L} e^{-D(\frac{n\pi}{2L})^2 t} \; (n=1,3,5...2l+1) \qquad (5)$$

where

$$C_n=\frac{1}{L}\int_0^L N_0 \sin\frac{n\pi x}{2L}dx=\frac{4N_0}{n\pi} \qquad (6)$$

The kinetics of the 1S exciton bleach can be described by

$$\Delta A(t)=\alpha\int_0^L N(x,t)dx \qquad (7)$$

where α is the absorption coefficient of the QD with single electron at the 1S exciton peak position. Because the terms of Fourier series with n>1 are negligibly small compared with the n=1 term, we can thus write the kinetics of 1S exciton bleach as:

$$\Delta A(t) \approx \frac{16\alpha N_0 L}{\pi^2} e^{-D_0(\frac{\pi}{2L})^2 t} \qquad (8)$$

The pre-exponential coefficient can be determined from the initial bleach amplitude (t=0). Therefore, half lifetime of the 1S exciton bleach recovery is given by

$$\tau_{1/2} = \frac{4\ln 2}{\pi^2}\frac{L^2}{D_0} \qquad (9)$$